NASA CONTRACTOR REPORT

NASA CR-7

NASA CR-747

SUPERSONIC MIXING OF HYDROGEN AND AIR

by John H. Morgenthaler

Prepared by
JOHNS HOPKINS UNIVERSITY
Silver Spring, Md.
for

NATIONAL AERONAUTICS AND SPACE ADMINISTRATION • WASHINGTON, D. C. • APRIL 1967

NASA CR-747

SUPERSONIC MIXING OF HYDROGEN AND AIR

By John H. Morgenthaler

Funded by NASA and Prepared under
Navy Contract No. NOw 62-0604-c by
JOHNS HOPKINS UNIVERSITY
Silver Spring, Md.

for

NATIONAL AERONAUTICS AND SPACE ADMINISTRATION

For sale by the Clearinghouse for Federal Scientific and Technical Information
Springfield, Virginia 22151 – CFSTI price $3.00

SUPERSONIC MIXING OF HYDROGEN AND AIR

by John H. Morgenthaler

Applied Physics Laboratory, The Johns Hopkins University
Silver Spring, Maryland

SUMMARY

The object of this work was to study quantitatively the effects of fuel injection parameters on the mixing of gaseous hydrogen with a supersonic air stream confined within a cylindrical duct to provide background information necessary for the design of combustors for supersonic combustion ramjets. Hydrogen was injected at sonic velocity into Mach 2 and Mach 3 air streams in a 1-in.-diameter duct at overall fuel-air equivalence ratios (ER) of 0.17 to 0.50, in both radial (transverse) and axial (downstream) directions from circumferential wall slots. The hydrogen and air supplies were at ambient temperature; air pressure was adjusted to give test section pressures slightly greater than 1 atm. Radial injection gave considerably better penetration and mixing than axial injection at the expense of a greater loss in stagnation pressure. For radial injection into Mach 2 air, fuel distribution improved as fuel flow (hence ER) was increased for a given slot width and as slot width was increased (5, 10, 15 mils) for a given fuel flow. For ER $>$ 0.5, a divergent duct would be required to maintain supersonic flow downstream of the injection station (with combustion, choking would occur earlier and/or at lower ER.)

For the case of radial injection from a 5-mil slot, the eddy diffusivity of mass, E_d (turbulent diffusion coefficient), and radial velocity, V_r, were determined by differentiating experimental concentration, axial velocity, and density profiles obtained at various axial distances from the injection station. As a first approximation to a representation of these results, a simple model was chosen in which E_d varied only in the radial direction and V_r varied only in the axial direction. The profiles chosen to represent $E_d(r)$ for various test conditions suggested that a) there may be a critical injection range within the region $0.17 < ER \leq 0.33$ which produces a many-fold increase in E_d (further increase in ER was less beneficial), and b) for a given ER and slot width, the air inlet Mach number may not affect E_d appreciably. This simple $E_d(r)$, $V_r(z)$ model was tested by numerical integration of the diffusion equation and simultaneous solution of the diffusion and momentum equations beginning from an initial set of experimental profiles in each case; computed downstream profiles of concentration and velocity agreed reasonably well with experimental profiles. An iterative procedure for solving the simplified energy equation together with the diffusion and momentum equations was developed for systems with variable stagnation temperature and arbitrary turbulent Lewis and Prandtl numbers.

INTRODUCTION

The problem of mixing fuels with a supersonic air stream has become important through its application to hypersonic ramjets employing supersonic diffusion flames, i.e., supersonic combustion engines (Refs. 2-6). It has been shown (Refs. 2-4) that in the speed range above Mach 8 to 10 the supersonic combustion cycle will be superior to the more conventional subsonic combustion ramjet cycle. In the latter engine, extensive molecular dissociation would occur at the excessive combustor temperatures that result at hypersonic flight speeds, so that performance would suffer due to the highly dissociated, non-equilibrium exhaust flow. For example, it has been estimated that the net thrust of a subsonic combustion engine with stoichiometric fuel flow would fall to zero near Mach 10 for kerosene (Refs. 3,7) and also would fall to unacceptable levels for hydrogen (Ref. 7). In addition, the high pressures, high heat fluxes, and loads that would exist in a subsonic combustion engine at these high Mach numbers would greatly increase materials and structural problems.

An alternative mode of supersonic combustion to the diffusion flame is shock-induced combustion, controlled by an oblique wave mechanism, in which fuel and oxidizer are premixed prior to combustion. Considerable small-scale research testing has been conducted utilizing this mode of supersonic combustion (Refs. 8,9). Shock-induced combustion also has been used extensively for investigating the kinetics of chemically reacting systems (Refs. 10,11). However, the use of shock-induced combustion of premixed fuel and air does not appear promising for practical application to ramjet engines because the combustion chamber geometry, upstream flow conditions, and heat release are complexly interconnected; these interrelations might be expected to cause problems of preignition or combustion instability that could limit the speed range (Ref. 12). Because of these problems, interest in recent years has centered on the supersonic diffusion flame, although oblique shocks induced by the fuel injection (without premixing) also may occur in these systems (Ref. 13).

The supersonic diffusion flame requires that fuel and oxidizer be mixed sufficiently well so that combustion can be initiated and propagated while maintaining supersonic flow in the combustion chamber. It is generally desirable to minimize (or deliberately control) oblique shock waves in the flow. Normal shock waves or large subsonic recirculation zones, such as would be produced by baffles, are unlikely to be used in a supersonic combustion engine. Although streamlined fuel injectors might be used to help distribute the fuel, they would complicate the geometry and structural problems in this severe environment. For these reasons, and because the static temperature attains its maximum near the wall, fuel injection from the wall into the boundary layer of the air stream appears to be a good method for initiating combustion. Disturbances created in the flow will depend on the injection angle and other

injection parameters; however, any oblique shock wave or flow-turning compression that results from the injection can be considered part of the air compression (inlet) system for the engine.

Injection from a wall slot can be in the axial direction parallel to the direction of flow of the air stream, or in the radial direction perpendicular to the air stream, or at some intermediate angle. Since the perpendicular and parallel injection cases are the simplest of the practical geometries to treat analytically and provide bounds for the intermediate cases of downstream injection at an angle to the flow, they were used exclusively in this investigation.

Coaxial injection has an important advantage over radial injection from the viewpoint of engine cycle performance, because the downstream component of momentum of the injected fuel, even though small, may contribute significantly to theoretical net engine thrust at hypersonic flight speeds. On the other hand, radial injection of fuel normal to the air stream should produce greater fuel penetration into the main stream, and consequently, better mixing* and a higher overall combustion efficiency for a given combustor length. An oblique shock wave produced by the radial injection would, of course, represent a loss in stagnation pressure in the air stream, but this effect would be compensated (at least partially) by the smaller loss in stagnation pressure due to heat addition at a lower Mach number behind the shock wave. On balance, the radial injection case appeared to be of greater interest, particularly for injection into a Mach 2 or Mach 3 air flow (simulating flight speeds of Mach 5 to Mach 9) because combustor entry temperatures would still be relatively low (less favorable for ignition, which oblique shocks would help), and the effect of axial momentum of the fuel would not be significant. Consequently, greater experimental emphasis was placed on radial injection of hydrogen through a circumferential wall slot into a supersonic air stream, but a few runs also were made with axial injection through a small annulus at the wall for comparison.

The cylindrical geometry chosen for this investigation may be considered to represent the injection and mixing section of a combustor. The broad objective was to study mixing quantitatively to aid in the design of a practical supersonic combustor. A constant-area duct represents one possible injector configuration, and, of course, cylindrical geometry is simple and convenient. (It is recognized that once combustion is initiated, a divergent section might be required to maintain supersonic flow for the case of low combustor inlet Mach number.) For experimental

---

* Theoretical calculations made by Vranos and Nolan (Ref. 14) suggest that coaxial injection might result in relatively good mixing at low ratios of fuel jet momentum to air jet momentum; however, no experimental data were presented for coaxial mixing.

flexibility, and because of the relatively long run times (30 min) required to obtain a detailed set of concentration, velocity, and density profiles, and the correspondingly high hydrogen requirement, a one-inch-diameter test section was chosen for this work.

Since turbulent flow will occur in almost all practical supersonic combustion engines, and turbulent mixing is much more rapid than laminar mixing, only the turbulent case is considered herein. The statistical theory of turbulence is not sufficiently developed to allow its application to this supersonic mixing problem (Refs. 15, 16). The phenomenological approach, which has been used successfully for a considerable period of time for investigating jet mixing problems (see App. A), employs empirically determined turbulent transport coefficients; **e.g.**, eddy diffusivities of mass (E_d), momentum (E_m), and heat (E_h) (or the eddy thermal conductivity, K). They are defined as functions of the fluctuating component of the product of the density and radial velocity with the fluctuating component of the mass fraction, axial velocity, and static enthalpy, respectively, and must be empirically established for a given system; they depend on (at least) position and the radial gradients of the time-averaged values of Y, V_z, and T, respectively. Using them, the turbulent equations of change are obtained (e.g., Ref. 1). It is important to recognize that chemical reactions (such as combustion reactions) occur on a molecular scale, which does not necessarily correspond to the time-averaged measurements.

By making several assumptions, the general equations may be considerably simplified and the turbulent transport coefficients may be obtained by differentiating experimental data. This course was chosen in this investigation rather than the more usual one of assuming simple relationships to predict the coefficients and then testing their validity by integrating the basic equations in an attempt to reproduce experimental profiles. It was selected because large radial variations in E_d and E_m were anticipated. They should be near zero in the laminar sublayer near the wall where molecular transport rather than turbulent eddy transport is important, and should increase through the turbulent boundary layer. Recent experimental investigations of supersonic mixing (Refs. 17, 18) have shown that even in the case of coaxial free jets, neither E_d, E_m, nor the eddy viscosity, $\epsilon = \bar{\rho}E_m$, is constant in the radial direction as often has been assumed. To permit evaluation of the E_d's, E_m's, and $\bar{V}_r$'s obtained, a numerical integration which used experimentally determined profiles as the initial conditions was developed to solve the turbulent diffusion and momentum equations both separately and simultaneously. Inconsistencies in the eddy diffusivities caused by differentiation of the experimental data could be determined in this manner, and by using an iterative procedure, values could be continually improved.

SYMBOLS

A, B	A (r,z), B(r,z), defined in Eq. (28), ft^{-1}
b	Base used in transformation of radial coordinate in Eq. (C-26)
c_p	Specific heat at constant pressure, ft-lbf/lbm-^oR
C, E, F	C(r,z), E(r,z), F(r,z) defined in Eq. (30), ft^{-1}, ft^{-1}, and $(ft\text{-}sec)^{-1}$, respectively
c_v	Specific heat at constant volume, ft-lbf/lbm-^oR
D	Molecular diffusivity, or diffusion coefficient, ft^2/sec
E_d	Eddy diffusivity of mass, ft^2/sec
E_h	Eddy diffusivity of heat, ft^2/sec
E_m	Eddy diffusivity of momentum, ft^2/sec
ER	Overall fuel-air equivalence ratio
g_c	Dimensional constant, 32.174 lbm-ft/lbf-sec^2
h	Enthalpy, ft-lbf/lbm
k	Molecular thermal conductivity, ft-lbf/sec-ft-^oR
k_n	Constant in Eq. (14)
L, M	L(r,z), M(r,z), defined in Eq. (B-2), ft^{-1}
Le	Lewis number, $\rho D c_p/k$
M	Mach number
M_i	Total mass of component i, lbm
$\mathfrak{M}$	Molecular weight, lbm/lb-mole-^oR
$\dot{m}$	Mass flow rate (dm/dt), lbm/sec
N, P	N(r,z), P(r,z), defined in Eq. (B-2), ft-lbf/lbm-ft^2
P	Pressure, lbf/ft^2
Pr	Prandtl number, $c_p\mu/k$
R	Universal gas constant, 1545.1 ft-lbf/lb-mole-^oR
r	Radial coordinate, ft
r^*	Coordinate of wall or centerline, defined by Eq. (15), ft
r_s	Radial coordinate of streamline, ft
Sc	Schmidt number, $\mu/\rho D$; Sc = Pr/Le; $Sc_T = E_m/E_d$
T	Absolute temperature, ^oR
t	Time, sec
V	Mass-average or bulk velocity, ft/sec

w	Transformed radial coordinate defined in Eq. (C-26)
x	Distance from wall, ft
x_H	Distance from wall at which $Y = \frac{1}{2} Y_{max}$
Y	Mass fraction (denotes hydrogen when without subscript)
z	Axial coordinate, ft
γ	Specific heat ratio, c_p/c_v
ϵ_s	Eddy viscosity, lbm/ft-sec
κ	Eddy thermal conductivity, ft-lbf/sec-ft-^oR
μ	Molecular shear viscosity, lbm/ft-sec
ρ	Density, lbm/ft^3
Φ	Dissipation function, ft-lbf/ft^3-sec

Subscripts

a	Air
av	Average
c	Cone
h	Hydrogen
i	Particular molecular (or atomic) species
j	Radial grid designation
m	Mixture
max	Maximum
n	Axial grid designation
R	Ram or pitot (pressure behind normal shock)
r	Radial component
T	Turbulent
t	Total or stagnation
w	Wall
z	Axial component

Superscripts

$( )'$	Fluctuating component
$(\overline{\ })$	Time-averaged quantity; used in Eqs. (1-20) but dropped thereafter for simplicity

METHOD OF DETERMINATION OF TURBULENT TRANSPORT COEFFICIENTS

The general equations of change* for steady, axially-symmetric, turbulent flow in which no significant variation in stagnation temperature occurs are summarized below. (Detailed development is given in Ref. 1). Following standard notation, a bar is placed over symbols that represent time-averaged quantities.

Turbulent Continuity Equation

$$\frac{1}{r}\frac{\partial}{\partial r}\left(\overline{\rho V}_r r\right) + \frac{\partial}{\partial z}\left(\overline{\rho V}_z\right) = 0 \tag{1}$$

Turbulent Diffusion Equation

$$\overline{\rho V}_r \frac{\partial \overline{Y}}{\partial r} + \overline{\rho V}_z \frac{\partial \overline{Y}}{\partial z} = \frac{1}{r}\frac{\partial}{\partial r}\left[\overline{\rho}\,(D + E_{d_1})r\frac{\partial \overline{Y}}{\partial r}\right] + \frac{\partial}{\partial z}\left[\overline{\rho}\,(D + E_{d_2})\frac{\partial \overline{Y}}{\partial z}\right] \tag{2}$$

Turbulent Navier-Stokes Momentum Equations

a. Radial Equation

$$\overline{\rho V}_r \frac{\partial \overline{V}_r}{\partial r} + \overline{\rho V}_z \frac{\partial \overline{V}_r}{\partial z} = -g_c \frac{\partial \overline{P}}{\partial r} + \frac{2\mu}{r}\left(\frac{\partial \overline{V}_r}{\partial r} - \frac{\overline{V}_r}{r}\right) + \frac{2\epsilon_1}{3r}\left(2\frac{\partial \overline{V}_r}{\partial r} - \frac{\overline{V}_r}{r} - \frac{\partial \overline{V}_z}{\partial z}\right)$$

$$+ \frac{\partial}{\partial r}\left[\frac{2(\mu + \epsilon_1)}{2}\left(2\frac{\partial \overline{V}_r}{\partial r} - \frac{\overline{V}_r}{r} - \frac{\partial \overline{V}_z}{\partial z}\right)\right] + \frac{\partial}{\partial z}\left[(\mu + \epsilon_2)\left(\frac{\partial \overline{V}_z}{\partial r} + \frac{\partial \overline{V}_r}{\partial z}\right)\right] \tag{3}$$

b. Axial Equation

$$\overline{\rho V}_r \frac{\partial \overline{V}_z}{\partial r} + \overline{\rho V}_z \frac{\partial \overline{V}_z}{\partial z} = -g_c \frac{\partial \overline{P}}{\partial z} + \frac{1}{r}\frac{\partial}{\partial r}\left[(\mu + \epsilon_3)\, r\left(\frac{\partial \overline{V}_z}{\partial r} + \frac{\partial \overline{V}_r}{\partial z}\right)\right]$$

$$+ \frac{\partial}{\partial z}\left[\frac{2(\mu + \epsilon_4)}{2}\left(2\frac{\partial \overline{V}_z}{\partial z} - \frac{\partial \overline{V}_r}{\partial r} - \frac{\overline{V}_r}{r}\right)\right] \tag{4}$$

---

* For initially isoenergetic flow in which the turbulent Prandtl and Lewis (and hence Schmidt) numbers are unity, a constant stagnation temperature is a solution of the simplified energy equation (Ref. 19).

where the turbulent transport coefficients are defined by the relations*

$$\overline{(\rho V_r)'Y'} \equiv - \bar{\rho} E_{d_1} \frac{\partial \bar{Y}}{\partial r} \tag{5}$$

$$\overline{(\rho V_z)'Y'} \equiv - \bar{\rho} E_{d_2} \frac{\partial \bar{Y}}{\partial z} \tag{6}$$

$$\overline{(\rho V_r)'V_r'} \equiv - \frac{2\epsilon_1}{3} \left(2 \frac{\partial \bar{V}_r}{\partial r} - \frac{\bar{V}_r}{r} - \frac{\partial \bar{V}_z}{\partial z} \right) \tag{7}$$

$$\overline{(\rho V_z)'V_r'} \equiv - \epsilon_2 \left(\frac{\partial \bar{V}_z}{\partial r} + \frac{\partial \bar{V}_r}{\partial z} \right) \tag{8}$$

$$\overline{(\rho V_r)'V_z'} \equiv - \epsilon_3 \left(\frac{\partial \bar{V}_z}{\partial r} + \frac{\partial \bar{V}_r}{\partial z} \right) \tag{9}$$

$$\overline{(\rho V_z)'V_z'} \equiv - \frac{2\epsilon_4}{3} \left(2 \frac{\partial \bar{V}_z}{\partial z} - \frac{\bar{V}_r}{r} - \frac{\partial \bar{V}_r}{\partial r} \right) \tag{10}$$

Equations (2) to (4) cannot be solved directly for the six unknown transport coefficients unless some assumptions are made concerning their relationships, e.g., that some are either equal or negligible. However, even when such assumptions are made, accurate determination of the remaining terms in these equations using experimental data would be difficult. An alternative approach, which leads to considerable simplification, is to make several general assumptions concerning the flow. The simplifying assumptions that appear reasonable when the bulk flow is supersonic are:

1) Diffusion in the axial direction is negligible compared to that in the radial direction.

2) Viscous normal stresses are negligible compared to the pressure.

---

* The axial dispersion coefficient is frequently defined in a similar manner to E_{d_2} in Eq. (6) (Ref. 20).

(An order of magnitude analysis shows this assumption is reasonable even in the boundary layer where viscous forces attain their maxima.)

3) Viscous shear stresses depend primarily on the radial gradient of axial velocity ($\partial\overline{V}_z/\partial r \gg \partial\overline{V}_r/\partial z$).

4) Fluctuating components of the axial velocity are negligible compared to corresponding time-average quantities [$\overline{\rho V_z}\,\overline{V_z} \gg \overline{(\rho V_z)'V_z'}$].

Using these assumptions, Eqs. (2) and (4) become, respectively,

$$\overline{\rho V_r}\,\frac{\partial\overline{Y}}{\partial r} + \overline{\rho V_z}\,\frac{\partial\overline{Y}}{\partial z} = \frac{1}{r}\,\frac{\partial}{\partial r}\left[\overline{\rho}E_d r\,\frac{\partial\overline{Y}}{\partial r}\right] \tag{11}$$

$$\overline{\rho V_r}\,\frac{\partial\overline{V}_z}{\partial r} + \overline{\rho V_z}\,\frac{\partial\overline{V}_z}{\partial z} = \frac{1}{r}\,\frac{\partial}{\partial r}\left[\overline{\rho}E_m r\,\frac{\partial\overline{V}_z}{\partial r}\right] - g_c\,\frac{\partial\overline{P}}{\partial z} \tag{12}$$

where $E_d \equiv E_{d_1}$, and E_m is defined by the relation,

$$\overline{(\rho V_r)'V_z'} = -\,\overline{\rho}E_m\,\partial\overline{V}_z/\partial r \approx -\,\epsilon_3\,\partial\overline{V}_z/\partial r \tag{13}$$

In Eqs. (11) and (12) molecular transport has been neglected compared to turbulent transport, an assumption normally valid except within the laminar sublayer; however, they may still be applied within this region if E_d and E_m are considered the sums of the molecular plus turbulent coefficients.

Probably none of the terms in Eq. (3), the radial momentum equation, are large; therefore, it is difficult to conclude which, if any, of them may be neglected. However, if $\epsilon_2 \approx \epsilon_3$, i.e., $\overline{V}_r\overline{\rho'V_z'}$ and $\overline{V}_z\overline{\rho'V_r'}$ are small compared to $\overline{\rho}\;\overline{V_r'V_z'}$ (or are approximately equal), or if axial derivatives are much less than radial derivatives in this equation, ϵ_1 could be obtained. Alternatively, if $\overline{\rho V_r}\,\overline{V_r} \gg \overline{(\rho V_r)'V_r'}$, ϵ_2 may be determined. If all viscous terms in this equation are negligible, so that it reduces to an Euler equation, it still would be useful for checking the consistency of the inertial and pressure terms, and hence, the experimental measurements. If inertial terms also are negligible, Eq. (3) becomes the radial boundary layer momentum equation ($\partial\overline{P}/\partial r = 0$). Since the transfer of axial momentum is generally of greater interest than the transfer of radial momentum, frequently this equation need not be considered at all, i.e., values of ϵ_1 and ϵ_2 are not of interest.

One method for determining E_d, E_m, and $\overline{V}_r$ is differentiation of the experimental $\overline{Y}$, $\overline{V}_z$ and $\overline{\rho}$ profiles, and substitution of these derivatives in Eqs. (11) and (12). Using an assumed value of the turbulent Schmidt number,* Sc_T (near unity), Eqs. (11) and (12) can be solved simultaneously for E_d, E_m and $\overline{V}_r$. Equation (1) would be used to check the consistency of values of $\overline{V}_r$. If Eq. (1) were not satisfied, a new Sc_T would be assumed and the procedure repeated. An obvious disadvantage of this method is the need to obtain second derivatives from experimental data, which requires extremely closely spaced and accurate data points.

One integration of Eqs. (1), (11), and (12) eliminates the need for obtaining second derivatives and allows determination of the unknown terms directly. This integration can be accomplished by an extension of Shipman's method (Ref. 21) in which these equations are integrated once in the radial direction, between either the wall or the centerline and a "streamline", i.e., a line bounding a fixed mass flow, designated $r_s(n)$.

The value of $r_s(n)$ is found for various test section lengths and values of the constant k_n by a numerical evaluation of the integral

$$\int_{r^*}^{r_s(n)} \overline{\rho V}_z \, r\,dr = k_n \tag{14}$$

where r^* designates either the wall or the centerline. The boundary conditions at r^* are

$$r^* = \begin{cases} r_w: & \overline{V}_z = 0,\ \overline{V}_r = 0,\ \partial\overline{Y}/\partial r = 0 \\ 0: & \partial\overline{V}_z/\partial r = 0,\ \overline{V}_r = 0,\ \partial\overline{Y}/\partial r = 0 \end{cases} \tag{15}$$

since no mass diffuses through the wall, the velocity at the wall is zero, and the centerline is an axis of symmetry. Equation (14) shows that there will be no net flux of mass across the streamline by convection, although both hydrogen and air cross the streamline by diffusion (equal masses in opposite directions). Multiplying each term in Eq. (1) by rdr, integrating from either the wall or the centerline to r_s, and applying the generalized Liebnitz formula (Ref. 22) for interchanging the order of differentiation and integration, yields

$$\left[\overline{\rho V}_r r_s\right]_{r_s} + \frac{\partial}{\partial z}\int_{r^*}^{r_s} \overline{\rho V}_z r\,dr = \left[\overline{\rho V}_z r_s \frac{\partial r_s}{\partial z}\right]_{r_s} \tag{16}$$

*The assumed Sc_T gives a relation between E_m and E_d.

But Eq. (14) requires that the second term on the left be zero, so that at r_s

$$\overline{\rho V}_r = \overline{\rho V}_z \, \partial r_s/\partial z \tag{17}$$

Equations (11) and (12) may be integrated in a similar manner using Eqs. (15) and (17), to give

$$\frac{\partial}{\partial z} \int_{r^*}^{r_s} \overline{\rho V_z} \, \overline{Y} r dr = \left[\overline{\rho} E_d r_s \frac{\partial \overline{Y}}{\partial r} \right]_{r_s} \tag{18}$$

and

$$\frac{\partial}{\partial z} \int_{r^*}^{r_s} \overline{\rho V_z} \, \overline{V}_z r dr = \left[\overline{\rho} E_m r \frac{\partial \overline{V}_z}{\partial r} \right]_{r^*}^{r_s} - g_c \int_{r^*}^{r_s} \frac{\partial \overline{P}}{\partial z} r dr \tag{19}$$

These integral equations also can be obtained directly by noting that since neither hydrogen nor momentum leaves or enters a streamtube by convection, any variation of these parameters within the streamtube must be caused by diffusion normal to the flow. Equations (18) and (19) were solved for E_d and E_m, respectively. Note that since $\partial V_z/\partial r = 0$ at the centerline, no momentum flux crosses the centerline, but that there is a momentum flux to the wall since $\partial \overline{V}_z/\partial r \neq 0$ at the wall; of course, $\partial \overline{Y}/\partial r$ is zero at the wall. As previously noted, near the wall in the laminar sublayer the molecular diffusivity and viscosity, D and μ, rather than E_d and E_m, become important.

If radial pressure variations can be experimentally determined, the last term in Eq. (19) may be evaluated numerically using the measured local free-stream static pressure, e.g., obtained with a conical probe. This numerical evaluation could be most readily accomplished using the Liebnitz formula

$$\int_{r^*}^{r_s} \frac{\partial \overline{P}}{\partial z} r dr = \frac{\partial}{\partial z} \int_{r^*}^{r_s} \overline{P} r dr - \left[\overline{P} r_s \frac{\partial r_s}{\partial z} \right]_{r_s} \tag{20}$$

Since r^* may equal either 0 or r_w, the various integrations may be carried out either from the wall or the centerline, so that two values of E_d and E_m may be obtained. These values will agree only if mass and momentum balances are consistent.

The integrals in Eqs. (18) and (19) were evaluated numerically at each test section length using interpolated* Y, V_z and ρ data, and the trapezoidal

---

* Henceforth we will refer only to the time-averaged quantities and will drop the bar notation for convenience.

rule at intervals of 0.002 in.; their axial variations were determined by fitting a truncated Laurent polynomial in $1/(z + a)$ and differentiating the polynomial. The terms $\partial Y/\partial r$ and $\partial V_z/\partial r$ were determined by numerical differentiation of the interpolated concentration and velocity data, using a five-point, second-order, running-smoothing routine, and ρ was determined by interpolation of the density profiles. Mass and momentum balances were computed using the interpolated data. In the data reduction, the assumption was made that radial pressure variations were negligible and that the stagnation temperature remained constant; these points are discussed in the following section.

No effort was made to determine the eddy diffusivity of heat, or eddy thermal conductivity, in this work since the stagnation temperature remained approximately constant throughout the flow; however, the simplified energy equation also can be integrated (see App. B) and used to determine these parameters when T_t measurements are available. In this way Pr_T and Le_T can be obtained as well as Sc_T.

APPARATUS AND PROCEDURE

The general apparatus used for these mixing studies is shown schematically in Fig. 1. The radial injection geometry used in the majority of the tests is shown in Fig. 2a; Fig. 2b shows the axial injection geometry used in a few runs for comparison. Air was supplied to the test section through a Clippinger-type, axially-symmetric nozzle (Mach 2 or Mach 3)* of 1.00-in. exit diameter. Pitot pressure (P_R) traverses across the exit planes of the nozzles indicated relatively flat Mach number and velocity profiles. The boundary layer thickness for the Mach 2 nozzle, computed from the von Karman momentum relation, was approximately 0.02 in. The nozzles were calibrated, so that they could be used to meter the air flow.

Test section static pressures were maintained above atmospheric so that no ambient air would enter the test section through the subsonic portion of the boundary layer. Stagnation temperatures were less than ambient (50° to 60°R less for the air) in these cold-flow tests because the gases experienced Joule-Thomson cooling when expanding from the high-pressure storage to the relatively low pressures upstream of the nozzles and venturi. A small, sonic venturi (throat diameter 0.079 in.) was used to meter the hydrogen; upstream pressure and temperature and throat pressure (to confirm choked flow) were measured. This venturi was calibrated by discharge into a known volume.

The metered hydrogen was injected from a ring manifold through a small circumferential slot (Fig. 2). The manifold pressure was normally considerably

---

* Nominal values; actual design Mach numbers were 1.98 and 3.04, Ref. 23.

greater than twice the test section pressure. The discharge coefficient of the hydrogen injector was determined for each run from the measured pressure and temperature of the injection manifold. Since the minimum cross-sectional area for the hydrogen flow existed at the inner wall of the test section (the exit of the injection slot), the hydrogen attained sonic velocity just prior to its initial contact with the air. For a given hydrogen flow rate, the injection pressure was established by the area of the injection slot. No effort was made to balance the injection pressure and the test section static pressure by varying the width of the slot; slot width was considered an independent variable.

Sampling System and Instrumentation. A combination milling and rotary table (3-axis) was used to move the gas sampling probe, cone-static probe, or thermocouple across the test section. A dial micrometer was used to indicate probe position. The tubing used for gas sampling probes (which also were used for pitot pressure) ranged from 0.010 to 0.013 in. I.D. with an O.D. ranging from 0.020 to 0.025 in. Most of the data were taken with the 0.010-in. I.D. tip, which proved to be the minimum practical size with respect to sample flow rate. Since the probe had a relatively blunt tip, a normal shock wave was present in front of the mouth of the probe. Confirmation of the fact that true samples were obtained was achieved for Mach 2 tests by mixing hydrogen with the air in the subsonic air line about 15 ft upstream of the nozzle, so that the gases were completely mixed at the sampling position (confirmed by radial traverses). Hydrogen concentrations calculated from the air nozzle and hydrogen venturi calibrations were within a few percent of those obtained with the calibrated thermal conductivity cell. Therefore, separation of the hydrogen and air entering the probe (due to the large difference in molecular weights, as observed, e.g., in Ref. 24) did not appear to be a problem. However, it will be noted later that the hydrogen mass balances were generally 12% to 30% low, and it is possible that preferential separation contributed in some degree to these discrepancies.

Small (0.1 in. deep) slots just slightly wider than the capillary sampling probe were used to position the probe at the end of the test section and to permit sample withdrawals and ram pressure measurements very close to the wall. The slots also allowed the probe tip to be positioned 0.1 in. upstream of the exit of the test section at the same location as the last wall static pressure tap.

All data were recorded on magnetic tape for subsequent reduction on the IBM 7094 computer. Pressures were measured with commerical strain-gauge transducers. An "electrical calibration" was made before each run by introducing fixed standard resistances into the transducer circuit, and periodic calibrations were made with known pressures. Iron-constantan thermocouples were used with reference junctions at approximately 100°F.

A VECO (Victory Engineering) M 182 thermal conductivity gas analysis cell was used for determining hydrogen concentration. This cell is an open diffusion type, which has a moderate rate of response and is slightly flow-

sensitive. It contained two matched, glass-coated, 2000-ohm thermistor beads in a stainless steel block and was connected to a Wheatstone bridge circuit. Cell pressure (normally 2 to 3 in. Hg) was adjusted with a needle valve to maintain a constant volumetric sampling rate; the water-proofed cell was immersed in an ice bath. Since cell output was not a linear function of gas composition, a calibration was made either before or after each run, metering the hydrogen and air with jewelled orifices that had been calibrated by discharge into a known volume (Fig. 3 and Table 1), and keeping the cell pressure at the level to be used during the run. In some cases when the probe was near the wall, the normal cell pressure could not be attained, and a second calibration at a lower pressure was required. Pressures were displayed both on recorders in the control room and on gauges in the test cell. The probe position (set with the dial micrometer) was recorded by setting the resistance of a decade box equal to the distance from the wall in ohms. The reference for the dial micrometer (one outside-radius of the probe) was set by touching the probe to the test section wall, completing an electric circuit and lighting a bulb. The pressure in the thermal conductivity cell was then adjusted manually to a predetermined value. When the recorder showed a stable cell output, the data acquisition system was activated. After measuring concentration at a given position, the quick-opening valve in the vacuum line to the thermal conductivity cell was closed, and the pitot pressure was recorded as soon as it became steady. The valve was then opened again, the probe was moved to a new location, and the procedure was repeated.

Normally, 25 to 35 data points were obtained across the 500-mil test section radius; points were spaced more closely near the wall than in the central region. Each complete concentration profile required approximately 30 min. A computer program converted the raw data (including calibrations) into total mass flow rates of hydrogen and air, discharge coefficient of the hydrogen injector, and local values of mass fraction of hydrogen, Mach number, static temperature, velocity, density, and mass flow rate per unit area for hydrogen and air. Local Mach numbers ($M > 1$) were computed from P_W/P_R by linear interpolation of a table generated using the Rayleigh pitot formula with $\Delta M = 0.01$ and $\gamma = 1.4$.

In some of the Mach 2 runs, an attempt was made to determine static pressure profiles via cone-static measurements.* The probe had a 10-degree semivertex angle and four 0.015-in. I.D. pressure taps located 0.16 in. from the tip and manifolded together. Unfortunately, even with this small probe

---

* In this case, P_c/P_R was used in the Mach number interpolation; P/P_R, computed from the Rayleigh formula, was multiplied by P_c/P obtained from a least-squares fit of data from cone-flow tables (Ref. 25).

the irregular profiles obtained were difficult to interpret and appeared to be inconsistent from station to station. Therefore, when attempts to use such pressure data in E_d calculations seemed to produce no more useful a picture than that obtained using wall static pressures and the assumption that $\partial P/\partial r \approx 0$, it was decided to adopt the latter simpler procedure for the results reported herein. Even though it was recognized that radial pressure gradients resulted from the hydrogen injection, especially near the injection station, the additional effort that would have been required to obtain satisfactory and consistent sets of profiles (preferably supported by some technique for viewing the flow field, e.g., schlieren pictures, which could not be done with opaque test sections) was beyond the scope of the present work.

In a few runs, stagnation temperature profiles were obtained using a small, shielded, butt-welded, iron-constantan thermocouple made from a 0.010-in. wire. The I.D. of the thermocouple shield was 0.062 in. with an O.D. of 0.083 in.; there were four 0.032-in. holes in its base 90° apart. Typical profiles (Fig. 4) indicated a 3% variation in stagnation temperatures in the Mach 2 test section. The assumption of constant T_t used in the subsequent data reduction therefore is considered to be justified.*

Using a constant stagnation temperature equal to the mass-average stagnation temperature of the hydrogen and air, the static temperature, T, was computed from M using the adiabatic relationship for a perfect gas. The density of the mixture was computed from P_w, T and Y (the H_2 mass fraction) using the perfect gas law

$$\rho = P_w \mathcal{M}_m / RT \tag{21}$$

where $\mathcal{M}_m \equiv \mathcal{M}_h \mathcal{M}_a / [Y\mathcal{M}_a + (1 - Y)\mathcal{M}_h]$. The densities of hydrogen and air present in the mixture were computed as

$$\rho_h = \rho Y \quad ; \quad \rho_a = \rho(1 - Y) \tag{22}$$

The axial velocity was computed from the relation

$$V_z = M \left(\gamma g_c RT/\mathcal{M}_m\right)^{\frac{1}{2}} \tag{23}$$

The average mass flow rate per unit area of either hydrogen or air present in an annular ring between two adjacent sampling points was computed by averaging the products of mixture density, mass fraction, and axial velocity for the two adjacent sampling points (j and j + 1)

---

* The analysis in Ref. 19 shows that if $\partial T_t/\partial r = 0$ at an initial axial station, and $Pr_T = Le_T = Sc_T = 1$, then (in an adiabatic system) T_t will remain constant throughout the flow. The effect of a 3% variation in T_t on these transport coefficients has not been determined.

$$(\dot{m}/A)_{h_j} = [\rho Y V_z]_{j_{ave}} \quad ; \quad (\dot{m}/A)_{a_j} = [\rho(1 - Y)V_z]_{j_{ave}} \tag{24}$$

The total mass flow rate of hydrogen was then computed by multiplying the local mass fluxes by the appropriate areas and summing across the duct

$$\dot{m}_h = \sum_{j=0}^{N-1} (\rho Y V_z)_{j_{ave}} \pi(r_{j+1}^2 - r_j^2) \tag{25}$$

where N is the total number of sampling points (using the convention $r_0 \equiv 0$).* The same procedure was used for air. Total momentum was obtained in a similar manner as

$$\text{Momentum} = \sum_{j=0}^{N-1} \left[\left(\frac{\rho V_z^2}{g_c} \right)_{j_{ave}} + P_j \right] \pi(r_{j+1}^2 - r_j^2) \tag{26}$$

where P_j was the local static pressure.

RESULTS AND DISCUSSION

Runs were made with radial injection of 0, 0.005, 0.010, and 0.015 lb/sec of hydrogen from a 5-mil slot into a Mach 2 air flow (1.06 lb/sec) for up to five test section lengths (length/duct-diameter ratios up to 5.9), other conditions being maintained as nearly identical as possible. Runs also were made with radial injection of 0 and 0.010 lb/sec of H_2 into 1.99 lb/sec Mach 3 air with four lengths. The eddy diffusivity of mass, E_d, and the radial velocity, V_r, were determined for these runs. The test conditions are summarized in Tables 2 and 3. A few tests were made to determine the effects of axial injection [Table 2(B)] and injection slot width with Mach 2 air; these effects can be discussed only qualitatively because of limited data.

During data reduction, the data profiles were smoothed in two steps. First a standard Aitkens polynomial interpolation routine was used to produce equally spaced points between data points. After some experimentation, a third-order polynomial and three interpolated points between data points were found suitable. Second, the resulting profiles were machine-plotted at large scale and smoothed by hand when necessary. The card decks were corrected accordingly for subsequent calculations.

---

* More accurate mass balances were obtained during computation of the turbulent transport coefficients by using smoothed interpolated data at 2-mil intervals, as previously discussed.

As previously noted, the static pressures used in the calculations were those measured at the wall, because attempts to determine static pressure profiles via cone-static measurements (within the scope of this work) were unsatisfactory. Efforts should be made in future work to obtain accurate local free stream static pressures and stagnation temperatures.

Air mass balances normally agreed within a few percent; hydrogen mass balances generally were low by 12% to 30%. Lack of agreement of the hydrogen balances is believed to have been caused by the difficulty in accurately determining the velocity and density, particularly in the region very near the wall where hydrogen concentration was large. Deficiencies in axial momentum balances increased with axial length in a reasonable manner because of wall friction, and with radial hydrogen injection rate, presumably because of stronger interactions and hence greater losses in stagnation pressure. These balances were computed using interpolated values of the concentration, velocity, and density at 2-mil intervals.

Mach 2 Inlet Air

Air Flow Without Hydrogen Injection. Axial velocity, density, Mach number, and static temperature profiles for the series of runs with no hydrogen injection (Table 2) are presented in Fig. 5. The expected trend of decreasing velocity with downstream distance from the injection station occurs in the boundary layer. [Because of the finite size of the sampling probe (0.010-in. I.D.), the deduced velocity at the wall was never zero (intercepts, not shown, were in the range 900-1100 fps.)]. The V_z and ρ profiles suggest that the 0.4-in. data are not consistent with those for the other lengths, but the M and T profiles are reasonably smooth. The fact that some irregularities do exist suggests that even more accurately machined parts should be used in future work. Test section diameters larger than 1 in. also would be advantageous in reducing the relative importance of wall irregularities.

Radial Injection--Low Flow Rate. Profiles for radial injection at $\dot{m}_h$ = 0.005 lb/sec (overall equivalence ratio of 0.17) using a 5-mil circumferential injection slot are presented in Fig. 6. Because of the large variation of concentration with axial length, the Y profiles are plotted on a logarithmic scale in Fig. 6(a) (mass fractions of 0.10 and 0.40 are equivalent to about 62 and 91 mole percent H_2, respectively). Hydrogen concentration at the wall decreases with length in a regular manner. (Since no hydrogen penetrates the wall, the slope of each Y profile should be zero at the wall.) In Fig. 6(b), the abnormally high V_z near the wall for the 0.05- and 0.4-in. test sections is not fully understood, but it is noted that the H_2 injection velocity (sonic) from the slot in the radial direction was approximately 3900 ft/sec in all tests, and the emerging hydrogen probably experienced an initial supersonic expansion in the lower static pressure environment of the test section. The irregularity of the same two profiles at greater distances from the wall probably results from shock waves which decreased in

strength with distance from the injection slot. The remainder of the V_z profiles are fairly smooth and nearly parallel. Of course, these V_z profiles were subject to much greater error than the Y profiles, since concentration was measured directly, but four different measurements (local-pitot and wall-static pressures, stagnation temperature, and hydrogen concentration) were used in the computation of V_z.

Figure 6(c) shows that the density near the wall increased with test section length, corresponding to the decrease in hydrogen concentration as mixing proceeds. Density was minimum at the wall because the hydrogen concentration was highest there. It might be noted that the deduced ρ depends on the same measurements as V_z, and in addition, on the static pressure directly. Comparing Figs. 5(a) and (c) with Figs. 6(b) and (d), respectively, shows that hydrogen injection thickens the boundary layer and decreases both V_z and M in the central region. The fact that the profiles are particularly irregular for the 0.05-in. length suggests that the assumption that $\partial P/\partial r = 0$ is unacceptable at this station because of a relatively strong oblique shock generated by the injection; however, its application for the longer test section lengths ($L \geq 0.4$) appeared adequate for the present purpose.

Radial Injection--Middle Flow Rate. Profiles for radial injection at $\dot{m}_h = 0.010$ lb/sec (overall equivalence ratio of 0.33) using a 5-mil circumferential injection slot are presented in Fig. 7. One important difference between Figs. 6(a) and 7(a)* is that in the latter the maximum hydrogen concentration does not occur at the wall for the 0.05-in. length. Apparently the hydrogen jet caused separation of the flow immediately downstream of the injection slot and an abnormally low wall-static pressure (11.3 psia) due to aspiration by the jet, which entrained some ambient air through the boundary layer into the test section, thereby reducing the hydrogen concentration in the boundary layer. Additional tests with the same hydrogen injection rate, but 20% more air, resulted in wall-static pressures slightly greater than ambient with a maximum hydrogen concentration at the wall, as indicated by the added note on Fig. 7(a). An important feature noted in comparison of Figs. 6(a) and 7(a) (note the change in the scale of the abscissa) is that, except for the 0.05 and 0.4-in. lengths, the higher $\dot{m}_h$ results in lower hydrogen concentrations at the wall, and penetration and spreading are greatly enhanced at this increased flow rate.

The velocity profiles in Fig. 7(b) are generally similar in shape to those for the lower hydrogen injection rate [Fig. 6(b)], but the average

---

* The small circles on Fig. 7(a) represent interpolated points, which were used to improve the accuracy of the numerical differentiation. Interpolated points were obtained for the Y, V_z and ρ profiles, but for clarity of presentation, they are shown only for the concentration profiles in Figs. 7(a) and 8(a). All data points are shown on figures in Ref. 1.

velocities are lower because of the increased injection rate. (For the 0.05-in. length, the velocity computed using the abnormally low measured wall-static pressure reached a maximum of 3900 ft/sec approximately 16 mils from the wall.) Density profiles are similar to those for the lower $\dot{m}_h$ except for their greater spread. The M and T profiles are more irregular. The M profiles are lower (average about 1.4) than those in Fig. 6(d) (average of about 1.8); the average value for the case of no hydrogen injection [Fig. 5(c)] was about 1.9. The M and T profiles for the 0.05-in. length do not appear valid for the reasons previously discussed.

Radial Injection--High Flow Rate. Three runs were made at $\dot{m}_h$ = 0.015 lb/sec (overall equivalence ratio of 0.50) using a 5-mil circumferential wall slot. The trends in the concentration profiles [Fig. 8(a)] are consistent with those for lower $\dot{m}_h$, but the maximum hydrogen concentrations (particularly for the 0.4-in. length) are lower and penetration is correspondingly greater. The bulges in the concentration profiles in the $50 < r < 100$ mil region which were barely suggested in Fig. 7(a) are more apparent in Fig. 8(a). The V_z, P, M, and T profiles of this series are similar to those in Fig. 7; the trends previously discussed are confirmed. Both V_z and M again are reduced in this case; M is close to unity. Thus, for equivalence ratios greater than 0.5, an expanding combustor geometry, e.g., conical, must be employed in order to prevent choking the flow, even without combustion.

Comparison of the concentration profiles obtained at various flow rates shows that initial fuel penetration is more important in obtaining a favorable fuel distribution than downstream turbulent mixing. This result is in agreement with that of Longwell, et al. (Ref. 26) for high-speed subsonic mixing.

Effect of Slot Width on Radial Injection. A number of runs were made in which the width of the radial injection slot was varied from 5 to 10 and 15 mils, other conditions being maintained as nearly equal as possible. Data for Mach 2 air and the three hydrogen injection rates previously reported are shown for two lengths: 0.4 in. in Figs. 9(a)-(c), and 5.9 in. in Figs 9(d)-(f). In most cases, a decrease in the maximum (wall) concentration and an improvement in penetration were obtained by increasing the slot width. In Fig. 9(f) the increase in centerline concentration with slot width is apparent. [The variations in V_z profiles (not shown) due to changes in slot width were relatively small (up to about 70 ft/sec); no consistent trends were obtained.]

Since the present work was restricted to opaque test sections, no photographs of the interactions within the duct could be obtained. However, it is interesting to consider implications of the pressure data. Shown on the figures are the measured static pressure at the wall just downstream of the injector (P_w), and the approximate static pressure of the hydrogen (P_h), computed by assuming that the hydrogen flow was choked in the slot and multiplying the measured hydrogen injection manifold pressure (P_{t_h}) by

$P/P_t = 0.528$ (for $M = 1$). When the P_h so computed is less than P_w, the injection must have been slightly subsonic ($M_h < 1$); when $P_h \gg P_w$, the hydrogen jet undoubtedly became supersonic immediately after leaving the slot. Therefore, it appears likely that at each flow rate, the 15-mil (nominal) slot gave slightly subsonic injection, the 10-mil slot gave approximately sonic injection, and the 5-mil slot (typical for most of the data in this report) produced a sonic jet that rapidly expanded to Mach 1.4-1.6. It is postulated that the 5-mil slot is poorest for penetration because a normal shock wave probably occurs in the jet relatively near the wall and thereafter the hydrogen's dynamic pressure, and hence penetration capability, is smaller. Further investigation of the injection process is required.

Axial Injection. Early in the test program a series of runs was made with brass test sections in a preliminary investigation of the relative merits of axial as opposed to radial injection. Test section geometries are illustrated in Fig. 2, and the run conditions for axial injection are included in Table 2. Results for axial injection through a 5-mil slot into Mach 2 air for a 3.4-in. test section length at three hydrogen flow rates are presented in Fig. 10. Comparing Fig. 10(a) with Figs. 6(a), 7(a), and 8(a) shows that mixing, as characterized both by maximum concentration at the wall and extent of penetration, was poorer with axial injection. In Fig. 10(a) maximum hydrogen concentrations at the wall are almost proportional to $\dot{m}_h$, whereas in many cases a decrease was obtained with radial injection; however, V_z and M profiles [Figs. 10(b) and 10(d)] do not decrease as much with increased $\dot{m}_h$ as they did with radial injection because of the initial axial momentum of the fuel and the fact that weaker shock waves occurred near the injector in the axial case. The density profiles [Fig. 10(c)] also reflect these effects.

Normalization of Concentration Profiles for Axial and Radial Injection. One of the curves Forstall and Shapiro (Ref. 27) used to correlate concentration and velocity profiles for axial injection of helium-air mixtures at the center of a subsonic air stream was the probability curve; for wall injection this equation becomes

$$Y/Y_{max} = 0.5^{(x/x_H)^2}$$

where x is the radial distance from the wall, Y is the local concentration at x, Y_{max} is the maximum (wall) concentration, and x_H is the distance from the wall at which the concentration is half the maximum. Figure 11 is a normalized plot of the axial injection data from Fig. 10 together with data obtained with a 0.775-in.-long brass test section. Most of the data points fall quite close to the probability curve, except those for $\dot{m}_h = 0.016$ lb/sec and the 3.4-in. length (the more divergent set of x's). However, the probability curve does not correlate the results for radial injection shown in Fig. 12. Comparison of Figs. 11 and 12 again shows that superior mixing is achieved with radial injection; normalized concentrations are greater for

radial injection at a corresponding radial position for $x/x_H > 1$.

Regardless of agreement with the probability curve, the normalization technique is useful for two reasons: it establishes the general shape of a concentration profile as soon as at least two experimental points are known, and it serves as a check on the general consistency of experimental data.

Mach 3 Inlet Air

Air Flow Without Hydrogen Injection. Profiles for a Mach 3 air flow rate of 1.97 lb/sec are presented in Fig. 13 for test conditions given in Table 3. These profiles are not as smooth as the corresponding Mach 2 profiles (Fig. 5), in part because of the increased difficulty (caused by partial freezing of the air pressure regulator) in maintaining the higher air flow rate required to keep test section static pressures greater than atmospheric, and in part because of the increased forces on the sampling probe. However, the profiles are generally similar to those obtained at Mach 2.

Radial Injection at 0.010 lb H_2/sec. Profiles for a series of runs with 1.99 lb/sec of Mach 3 air and $\dot{m}_h = 0.010$ lb/sec (overall equivalence ratio 0.15) with radial hydrogen injection through a 5-mil slot are presented in Fig. 14. Only two of these sets of profiles (at z = 2.9 and 5.9 in.) were obtained with the stainless steel sections. In order to at least estimate E_d and V_r for this Mach 3 case, earlier data obtained with somewhat oversized brass test sections, and in some cases slightly different $\dot{m}_h$ and $\dot{m}_a$, were used for other lengths (Table 3). Because of various test problems, the Mach 3 profiles were irregular. Therefore, before differentiating them for E_d and V_r determinations, they were smoothed by hand.

Determination of E_d and V_r

Computations of E_d and V_r were made for the Mach 2 case with radial injection using the data of Figs. 6, 7, and 8 and the procedure previously described. Results obtained for $\dot{m}_h = 0.005$ and 0.010 lb/sec are shown in Tables 4 and 5. In each table, Case 1 (from Ref. 1) was obtained by evaluating the axial variation of the integral in Eq. (18) using a fourth-order truncated Laurent polynomial in $1/(z + a)$; the second set was obtained using a second-order polynomial . The order of the polynomial fit can be up to one less than the number of axial stations available; however, the greater the order of the polynomial , the more frequent and extreme can be its oscillations and the more erratic the derivatives. Thus, use of a lower order least-squares fit smooths the experimental data at some risk of losing details of the distribution.

Case 1 in Tables 4 and 5 shows considerable variation in E_d and V_r in both the radial and axial directions, and in some regions even physically unreal negative values of E_d, so that they can be used only to estimate trends, which must be confirmed by the numerical integration techniques described below

before being accepted. The negative E_d values undoubtedly result from the difficulty in obtaining axial variations from only a few widely spaced test-section lengths, and especially the difficulty in obtaining the proper slope at the end points. The irregularities that occur at large distances from the wall can be ascribed to sensitivity to small measurement errors when the concentration profiles approach zero. The initial station, 0.05 in., also is suspect, because it represents only 10 slot widths downstream and may be strongly affected by an injection shock wave. The remaining values of E_d suggest that variation in the radial direction is more significant than variation in the axial direction. Similarly, V_r varies more strongly with z than with r.* Accordingly, various combinations of $E_d(r)$ and $V_r(z)$ profiles were tried, and the simple models shown in Fig. 15 were found to do a reasonable job of reproducing downstream experimental concentration profiles when used as input to the numerical integration routines. The results, to be presented later (Tables 8-11), show that small changes in E_d or V_r can result in large changes in Y; therefore, the simple models were considered adequate first approximations.

In Case 2 in Tables 4 and 5, the 0.05-in. length was omitted in addition to using a second-order (rather than a fourth-order) polynomial . Fewer negative values occurred and results are more regular and substantiate the general trends shown in Fig. 15, which had been chosen earlier based on Case 1. In Table 6, for $\dot{m}_h$ = 0.015 lb/sec, only a second-order polynomial could be used because data were available for only 3 lengths.

Comparison of curves A and B in Fig. 15(a) shows that for Mach 2 air at 1.06 lb/sec, the peak E_d increased by almost an order of magnitude when the hydrogen injection rate was doubled (from 0.005 to 0.010 lb/sec), but a further 50% increase in hydrogen flow rate (to 0.015 lb/sec, curve C) increased the peak E_d only an additional 30%. Such an effect suggests that for these test conditions, a critical turbulence level is reached at an injection rate between 0.005 and 0.010 lb/sec. Determination of this critical level would be very important in the design of practical combustors.

The E_d and V_r profiles for Mach 3 air at 1.99 lb/sec and a hydrogen injection rate of 0.010 lb/sec (curves D in Fig. 15) are very similar to those for Mach 2 air at 1.06 lb/sec and a hydrogen injection rate of 0.005 lb/sec (curves A). This result suggests that at the same small overall hydrogen/air equivalence ratio (ER $\sim$ 0.16), the inlet Mach number may not greatly affect E_d. For simplicity, E_d is considered to be the sum of the actual eddy diffusivity of mass (E_d) and the molecular diffusivity (D), because $E_d \gg D$ except in the laminar sublayer near the wall. At the experimental conditions, D = 0.0006 ft^2/sec (Ref. 28). Diffusivities of this general magnitude were obtained from the experimental profiles within 2 mils of the wall, and this

* Actually, V_r must be zero at the wall and also at the centerline; however, ignoring these constraints appeared to be reasonable for first approximations,

value was used throughout as E_d at the wall. Since both E_d and ρ reached minimum values at the wall, the model used by previous investigators (Refs. 12, 17, 29 and 30) in which either ρE_d or $\rho^2 E_d$ was assumed constant clearly does not apply for the case of radial injection of hydrogen from a duct wall into a supersonic air stream.

Solution of Diffusion and Momentum Equations

The best way to judge whether or not turbulent transport coefficients are valid is to integrate the basic equations of change (generally numerically) to permit comparison of profiles computed using them with those determined experimentally. Therefore, numerical solutions of the diffusion and momentum equations were obtained.

Numerical integration of Eq. (11) was accomplished by assuming $\overline{\rho\vec{V}} \approx \bar{\rho}\,\bar{\vec{V}}$ (i.e., neglecting $\rho'\vec{V}'$) and by writing it in the form (again dropping the bars for simplicity)

$$V_r \frac{\partial Y}{\partial r} + V_z \frac{\partial Y}{\partial z} = E_d \left[\frac{\partial^2 Y}{\partial r^2} + \left(\frac{1}{r} + \frac{1}{\rho} \frac{\partial \rho}{\partial r} + \frac{1}{E_d} \frac{\partial E_d}{\partial r} \right) \frac{\partial Y}{\partial r} \right] \tag{27}$$

which may be rewritten as

$$A(r,z) \frac{\partial Y}{\partial z} = \frac{\partial^2 Y}{\partial r^2} + B(r,z) \frac{\partial Y}{\partial r} \tag{28}$$

where

$$A(r,z) \equiv \frac{V_z}{E_d} \qquad B(r,z) \equiv \frac{1}{r} + \frac{1}{\rho} \frac{\partial \rho}{\partial r} + \frac{1}{E_d} \frac{\partial E_d}{\partial r} - \frac{V_r}{E_d}$$

Equation (28) is a parabolic partial differential equation, which can be solved numerically using the Crank-Nicolson technique (Refs. 31 and 1) in which partial derivatives with respect to r and z are approximated at intermediate points not part of the grid or mesh from values at six surrounding mesh points (App. C). The values of V_z, ρ, and $\partial\rho/\partial r$ at any axial position were obtained by fitting a polynomial in $1/(z + a)$ through experimental points at various lengths but at the same radial position. Various values of $E_d(r)$ and $V_r(z)$ were used in the evaluation of the coefficients A and B. Those yielding the best results were presented in Fig. 15. Equation (28) can be solved for new values of Y, once the coefficients have been evaluated.

Typical values of the coefficients in Eq. (28) and the various terms of which they are composed are presented in Table 7. Small values of A (always positive), which will result from either large E_d or small V_z, favor mixing. The coefficient B can be either positive or negative; it is composed of four separate terms (columns 6-9) which result from 1) curvature, 2) compressibility, 3) E_d variation, and 4) the V_r/E_d ratio. Since the last two are much more important than the first two, the ability of the numerical integration to predict reasonably accurate concentration profiles is a true test of the

correlating ability of the $E_d(r)$ and $V_r(z)$ models. Since variations of $\ln\rho$ and $\ln E_d$ are important, rather than their actual values, multiplication of ρ or E_d by a constant factor has no effect on B. The primed coefficients in the last two columns of Table 7 result from the change of variable from r to w (App. C); their greater uniformity, as compared to the unprimed coefficients, is the reason that valid solutions can be attained with far fewer radial grid points in the transformed variable w than in the original variable r.

Hydrogen concentration profiles obtained from numerical integrations of the diffusion equation at various axial locations are compared with corresponding experimentally measured profiles in Tables 8-11. Values of Y computed using various combinations of E_d and V_r profiles are tabulated so that the significant variations in the computed profiles, caused by only slight changes in the transport coefficients, can be seen. Additional perturbations of E_d and V_r probably would lead to improved agreement; of course, exact agreement cannot be expected using the simple model. Generally, both radial and axial variations in E_d and V_r must be considered in order to obtain exact agreement. Such detailed variations must await future refined experiments.

The numerical solution of the momentum equation is very similar to the diffusion equation. However, some modification is required because of three differences: 1) the momentum equation is non-linear, so that an iterative procedure is required, 2) the boundary condition at the wall requires that there be no slip at the wall, and 3) the momentum equation has an additional term, when axial pressure gradients exist in the flow. Equation (12) also can be written in the same form as was the diffusion equation, Eq. (27), as

$$V_r \frac{\partial V_z}{\partial r} + V_z \frac{\partial V_z}{\partial z} = E_m \left[\frac{\partial^2 V_z}{\partial r^2} + \left(\frac{1}{r} + \frac{1}{\rho} \frac{\partial \rho}{\partial r} + \frac{1}{E_m} \frac{\partial E_m}{\partial r} \right) \frac{\partial V_z}{\partial r} \right] - \frac{g_c}{\rho} \frac{\partial P}{\partial z} \qquad (29)$$

This equation may be written in a form similar to Eq. (28) as

$$C(r,z,V_z) \frac{\partial V_z}{\partial z} = \frac{\partial^2 V_z}{\partial r^2} + E(r,z) \frac{\partial V_z}{\partial r} + F(r,z) \qquad (30)$$

where

$$C(r,z,V_z) \equiv \frac{V_z}{E_m} \qquad E(r,z) \equiv \frac{1}{r} + \frac{1}{\rho} \frac{\partial \rho}{\partial r} + \frac{1}{E_m} \frac{\partial E_m}{\partial r} - \frac{V_r}{E_m}$$

$$F(r,z) \equiv - (g_c/\rho E_m) \, \partial P/\partial z$$

Although valid values of the eddy diffusivity of momentum (E_m) were not

determined by direct differentiation of the approximate velocity profiles, reasonable results were obtained in some cases by assuming $E_d = E_m$, i.e., $Sc_T = 1$. Only a few integrations of the momentum equation were made because of the increased computing time required by the iterations; the differences between E_d and E_m (i.e., variation of Sc_T) should be investigated in future work using more accurate velocity data.

Simultaneous Solutions of Diffusion and Momentum Equations

The least satisfying aspect of the separate solutions of the diffusion and momentum equations is the need to specify density profiles in advance, which requires prior knowledge of both the composition and static temperature. Of course, these integrations are the ultimate test of the validity of the E_d and E_m models. However, if T_t is constant throughout the flow, the need for specifying density profiles can be overcome by simultaneous solution of the diffusion and momentum equations using the Crank-Nicolson technique and a numerical iterative procedure. If oblique shock waves occur, the integration is still possible as long as the detailed pressure variation is known. Since initial Y and V_z profiles are given, the initial static temperature can be computed from the relationship

$$T = T_t - V_z^2/2g_c c_{p_m} \tag{31}$$

where $c_{p_m} = c_{p_h} Y + c_{p_a} (1 - Y)$. The initial density then can be computed using the known initial value of Y and Eq. (21); the initial value of $\partial\rho/\partial r$ can be obtained by numerical differentiation of this computed density profile. Equations (28) and (30) now can be solved using these initial values of the density, its radial derivative, and the initial value of V_z for a first iteration to give new values of Y and V_z at the next axial station. Averaging the new and initial values gives an improved estimate of the desired value of these terms midway between the new and initial values (at the mid-point in the computing grid). The process is repeated until no further change occurs in the values of the coefficients at the mid-point. For the cases investigated, two iterations generally proved sufficient. For the next integration step, the entire procedure is repeated using the newly computed values of Y and V_z as initial conditions. This procedure was successfully programmed, using a different value of the base, b, (App. C) for each of the equations, which greatly reduced computing time. The reasonable agreement between computed and experimental concentration and velocity profiles obtained using this technique is shown in Table 12.

Solution of Turbulent Mixing Problems

The energy equation must be included in any general analysis of turbulent mixing, since T_t will remain constant only in very special cases. No attempt was made to solve the energy equation in this investigation; however, the method for solving it together with the diffusion and momentum equations, again

using an iterative procedure, was worked out (see App. B). The method of solution for the general case is rather complex; fortunately, a great simplification results when Pr_T and Le_T (and hence Sc_T) are unity, since in this case it becomes identical in form to the diffusion equation. For the case of an adiabatic wall, the boundary conditions are completely analogous in these equations, so that the procedure used for solving the diffusion equation also may be used for this simple case of the energy equation. Thus, turbulent mixing problems can be solved using the general iterative procedure discussed above as long as the turbulent transport coefficients and the static pressure are known as functions of position, and the initial conditions are given. Of course, as previously discussed, if T_t is initially constant for each component prior to mixing, it will remain constant throughout the mixing region (when $Pr_T = Le_T = 1$) and the energy equation need not be considered at all (Ref. 19).

Future investigations should be made with an objective of predicting the transport coefficients and the initial profiles theoretically, or at least semi-empirically (for values of the various parameters within the range of greatest interest). However, the ultimate application of this numerical technique will be its extension to include chemical kinetics; of course, in this case the additional complications caused by the combustion process will have to be considered.

CONCLUDING REMARKS

The important conclusions of this work, applicable for sonic hydrogen injection from the wall into a ducted, Mach 2 or Mach 3 air stream for the range of hydrogen flow rates and test geometries investigated are:

1. Radial hydrogen injection results in considerably greater penetration and mixing than does axial injection for the cases compared.

2. Penetration of the supersonic air stream at the point of injection is more important in producing good mixing than turbulent diffusion downstream of the injection region.

3. Normalization of hydrogen concentrations yields a reasonable correlation of data obtained at various hydrogen injection rates and axial lengths for a given Mach number and injection configuration; i.e., given at least 2 (but preferably several) points, a correlation curve of characteristic shape can be drawn. For the axial injection case, the probability curve (Ref. 27), locatable by 2 points, correlated most of the data, but for radial injection, the curves were skewed, showing lower concentration at the wall and greater penetration than the probability curves.

4. For radial hydrogen injection, from a 5-mil circumferential wall slot, the following conclusions were drawn:

a) A simple model in which the eddy diffusivity of mass varies only in the radial direction and the radial velocity varies only in the axial

direction gave reasonable approximations of experimentally determined downstream concentration and velocity profiles when used for computing similar profiles.

b) A critical injection rate may exist above which turbulent mixing increases markedly. For Mach 2 air, there was a much larger percentage improvement in apparent E_d when the overall equivalence ratio was increased from 0.17 to 0.33 than from a further increase to 0.5.

c) For a given overall equivalence ratio, the effect of air inlet Mach number on mixing may be small. This point should be investigated further, because it relates to an important combustor design consideration.

d) For Mach 2 inlet air, a divergent section is required to maintain supersonic flow (even with no combustion) at an overall equivalence ratio greater than 0.5.

5. Some tests with increased slot width (10 and 15 mils) showed that penetration improved, presumably because the degree of underexpansion of the jet decreased.

6. The simplified diffusion and axial momentum equations apply throughout the flow field as long as axial diffusion is negligible compared to radial diffusion, viscous normal stresses are negligible compared to pressure, and the axial variation of the radial velocity is negligible compared to the radial variation of the axial velocity.

7. Simultaneous numerical solution of the simplified equations of change is feasible using the Crank-Nicolson technique.

APPENDIX A

BACKGROUND LITERATURE

When this work was begun in 1962, no references were found in the open literature which treated the mixing of gaseous fuel with a ducted supersonic stream in which axial pressure gradients existed. However, extensive literature existed concerning the related problem of free turbulent flows, in particular turbulent jets discharging either into a quiescent medium or into a coaxial flow which is considered to be infinite. These free turbulent flows represent the simplest case of turbulence relatively free from the effect of viscosity. However, even in this case understanding of the turbulence is not complete (16,32,33).* This appendix summarizes some of the pertinent background literature available up to 1965.

Incompressible Flow. In 1926 Tollmien (34) obtained the first solution for mixing in the region beyond the potential core of a turbulent jet discharging into a medium at rest (based on Prandtl's semi-empirical mixing length theory). Schlichting analyzed the corresponding laminar problem in 1933 (35). Both solutions depend on similarity of velocity profiles in the region of interest. Pai (16), Abramovich (32), and Forstall and Shapiro (27) have surveyed the extensive literature on jets discharging into a concurrent flow, which includes several hundred references, in addition to discussing results of their own investigations. Kuethe (36) extended Tollmien's results to the case of a two-dimensional jet discharging into a moving medium and obtained an approximate method for computing the velocity profile in the initial region of a round jet discharging into a medium at rest, but subsequent experimental data did not agree with his semi-empirical theory (32). Squire and Trouncer (37) extended Kuethe's results to the case of a round jet issuing into a uniform stream by assuming cosine velocity profiles across the jet (eliminating the need to solve the equation of motion) and integrating the boundary layer momentum equation. Reichardt (38) proposed an inductive theory which corresponds to a constant exchange coefficient, ϵ_o, in the normal direction across the mixing region. Görtler (39) applied Reichardt's assumptions and obtained velocity profiles in better agreement with experimental results than those initially obtained by Tollmien.

*In this section, numbers in parentheses are reference numbers.

Forstall and Shapiro (27) studied constant pressure mixing of a circular jet with an annular coaxial stream; they confirmed the existence of the cosine velocity profiles and showed that concentration profiles were of similar shape for the conditions of their experiments. Turbulent Prandtl and Schmidt numbers were found to be approximately 0.7, independent of their laminar counterparts, and the nature of the experiment. They presented an extensive literature survey and outlined the three principal historical methods for analytically attacking problems of jet spreading as follows:

"1) Point-source diffusion of momentum, material or temperature, using equations and solutions well known from the study of heat flow. This method is valid only at distances downstream from the point of initial mixing which are large compared to the initial jet width.

"2) Boundary-layer form of the Navier-Stokes equations, into which are inserted various transport theories.

a) Momentum transport, using the mixing-length concept.

b) Vorticity transport, using the mixing-length concept.

c) Constant exchange coefficient, using the concept of 'turbulent' coefficients of viscosity, thermal conductivity, and diffusion.

d) Kármán similarity theory.

e) Statistical theory.

"Most of the extensive literature on jets and wakes is concerned with this [second] approach...

"3) Integral equations of motion (Kármán momentum equations)."

Hinze (15) showed that when the velocity of the jet and the velocity of the ambient fluid are of the same magnitude, cosine profiles are not a solution of the equation of motion. Abramovich (32) considered the two-dimensional mixing in the presence of a longitudinal pressure gradient and found that with a positive gradient, the mixing region widens more rapidly, and vice versa, than in the case of constant pressure.

Compressible Flow. For a compressible fluid, the effect of density variations must be included, greatly complicating the analysis, because velocity and temperature effects must be considered simultaneously.

Szablewski (40, 41) theoretically investigated the turbulent diffusion of a subsonic hot jet in a subsonic air stream for both the core and the transition zones and used Prandtl's mixing length theories to

predict velocity and temperature along the jet axis and the width of the mixing region. Page, et al. (42) observed experimentally that for air flowing between parallel plates at low subsonic velocities, the eddy diffusivities of heat and momentum reached maxima of the order of 100 times their values near the wall about half-way to the centerline. Values at the centerline were slightly below ($\sim$ 25%) these maxima. The turbulent Prandtl number was less than unity throughout.

For low speed flow across a flat plate, Morkovin (43) found excessive scatter when attempting to determine the eddy diffusivities of mass, momentum, and heat by differentiating experimental profiles. He was successful in a trial-and-error approach in which he estimated an eddy diffusivity, integrated the basic equations of change, and compared resulting profiles with experimental profiles, repeating the process until agreement was attained.

Ruden (44) obtained the first systematic measurements of velocity and temperature distribution in an axially-symmetric, subsonic heated turbulent jet. The temperature distribution was appreciably broader than the velocity distribution in the fully developed turbulent region. Near the nozzle exit, the temperature distribution at the edge of the free jet was in much closer agreement with the modified vorticity transfer theory than with the momentum transfer theory. Corrsin and Uberoi (45) made a detailed investigation of heated round jets at subsonic speeds which included mean velocity and temperature distribution, and also turbulence level, temperature fluctuation level, and temperature velocity correlation. Keagy and Weller (46) studied jets of helium, nitrogen, and carbon dioxide discharging from sharp-edged orifices into still air and found that the difference in the densities of the jet and the medium into which it is discharging is important. Squire's data (47) for temperature distribution in subsonic, heated jets showed that similarity in temperature profiles was reached approximately 10 diameters downstream from the exit of the nozzle.

Abramovich (32) mentioned studies of turbulent compressible free jets by various Russian workers but concluded that there had been no systematic experimental verification of the assumptions made in their various theories and that only the velocity and temperature profiles at the cross section of a compressible free jet had been experimentally obtained. He stated that none of the (then) current theoretical approaches can be recommended. He presented a semi-empirical theory which predicts the jet spreading and velocity, temperature, and concentration profiles. He used Prandtl's hypothesis concerning the mechanism of the turbulent expansion of an incompressible jet, (i.e., geometric and kinematic similarity, and the proportionality of the fluctuations of velocity to the mean velocity gradient) to demonstrate that the velocity profile in a compressible jet can be normalized in the same manner as in the incompressible case.

Pai (48,49) assumed a constant exchange coefficient across the mixing region and discussed two-dimensional as well as axially-symmetric jet mixing. He later discussed (50) the general problem of two-dimensional, laminar mixing of chemically-reacting streams and numerically solved the case of subsonic mixing of streams of equal initial velocity. For two-dimensional laminar and turbulent mixing of two gases (16), he obtained solutions assuming that: 1) the mixture is a continuous medium, 2) no chemical reaction occurs, 3) both fluids are perfect gases, 4) the boundary layer assumptions apply, and 5) pressure is constant in the mixing zone. He also solved other specific mixing problems, e.g., turbulent free jet mixing at constant temperature.

Alexander, et al. (51) generalized Reichardt's inductive theory to include transport of heat and mass as well as momentum in free jets. This approach linearized the equation of motion for axially-directed momentum and thereby facilitated analytical solution of cases of free turbulence involving complicated boundary conditions.

Schlichting (52) outlined the procedure for solving the turbulent boundary layer equation assuming constant pressure and E_m constant in the radial direction, using an experimentally determined scale factor, σ, whose value depends on the divergence or spreading of the mixing region. Pai (16) gave experimental results of supersonic turbulent free jet mixing in terms of σ. Vasiliu (53) presented a plot of σ vs M for data of several investigators; for subsonic flows, $\sigma = 12$. Considerable spread is shown in the experimental data in the supersonic range with maximum values of σ of approximately 40 between Mach 2 and 3. The "divergence of mixing" concept appears to be most useful where σ is constant, since otherwise it merely becomes an arbitrary factor which "adjusts" profiles obtained at supersonic speeds to conform to subsonic data.

Longwell and Weiss (26) studied the distribution and mixing of liquids injected into subsonic air streams. They simplified the turbulent diffusion equation [Eq. (2)] by assuming E_d to be constant and V_r to be negligible; since the flow was subsonic, the assumption that the flow was incompressible also was made. Analytical solutions were obtained for a point source and for a ring source; they showed that in many practical cases much more mixing resulted from initial spreading from the injector than from eddy diffusion in the stream.

Recent Mixing Studies. In recent years application of supersonic diffusion flames to ramjet engines has renewed interest in mixing of a fuel jet with a supersonic stream. Vasiliu (53) considered turbulent mixing and reaction of a two-dimensional supersonic jet with a supersonic stream. He used Reichardt's constant exchange coefficient to evaluate E_d, which he assumed to be constant in the direction normal to the flow, and used the Crank-Nicolson method (31) to obtain numerical solutions to an idealized combustion problem.

Much of the recent work has been conducted at General Applied Science Laboratories (30,54) and the Polytechnic Institute of Brooklyn (12,17,29,55) through their close association. Both laminar and turbulent mixing problems have been considered; however, the following factors are common in most of this work: 1) a coaxial fuel jet (except Ref. 30, which considered a two-dimensional jet) discharges into a free air stream; 2) no pressure gradients exist; 3) the von Mises transformations, used by Pai (49) to solve similar mixing problems numerically, are employed to transform the boundary layer equations; 4) these transformed equations are linearized; 5) except in Ref. 54, either $\bar{\rho}E_m$ or $\bar{\rho}^2E_m$ is assumed to be constant in the radial direction; 6) no initial radial variation of velocity or concentration occurs in either stream; and 7) turbulent Prandtl and Lewis numbers are assumed to be near unity, so that the energy equation reduces to the same form as the diffusion and momentum equations. Since no body of experimental data is available for fuel injected into a supersonic air stream, much of the data for testing the theories are for the case of subsonic and supersonic injection into a quiescent medium, or in some cases into a subsonic secondary stream.

An important problem common to all of this work is that the turbulent boundary layer momentum equation does not apply across the initial region of the jet where a potential core still exists and large pressure gradients (and shock waves) occur; the equation applies only after the central jet has become fully developed (all boundary layer). Zakkay (17) recognized this limitation in his experimental investigations of coaxial mixing and did not consider the initial region of the jet, or the region downstream where shock waves exist. Libby (54) used a compressible transformation of Prandtl's empirically determined E_m for incompressible flow to determine the E_m and E_d (assumed equal) for compressible, coaxial-jet mixing and obtained good agreement with subsonic mixing data.

Kleinstein's analysis of coaxial laminar jets (55) was compared with the finite difference solution obtained by Pai (49) and agreed reasonably well for the particular example considered. His coaxial-turbulent-jet analysis (29) differed from Libby's in that he considered the eddy kinematic viscosity in terms of compressible flow variables and an arbitrary constant, determined experimentally. This approach did not rely on an extrapolation of empirical data from incompressible flow as did Libby's. He obtained reasonably good agreement for the case of subsonic discharge into a medium at rest. Only two cases of supersonic jets were included in the comparison of his theory with experimental data, both discharging into a medium at rest. Mach 1.5 data deviated only slightly from his analysis, but Mach 2.6 data showed considerable deviation.

Zakkay, et al. (17) experimentally determined E_d, E_m, Le_T, and Sc_T for the coaxial turbulent mixing of dissimilar gases; the central jet was subsonic or supersonic and discharged into an outer Mach 1.6 air stream. Various gases were used in the central jet. In general, the method was inconsistent because T_t was assumed to be constant throughout the flow in the computation of V_z and ρ (implying that Sc_T and $Le_T = 1.0$) and these values were then used for computing Sc_T and Le_T in some cases greatly different from unity (19). The method used required evaluation of the second derivatives of V, $\bar{h}$, and Y; it was applied only at the centerline since $\partial\rho/\partial r$, which could not be evaluated elsewhere, was zero there because of symmetry. Extensive profiles could not be obtained due to limitations on instrumentation and run time (1 min). An estimate of $E_m(r)$ was obtained by using Forstall and Shapiro's cosine profiles (27) and assuming the density to be constant (even though the flow was compressible). These cosine profiles were shown to give asymptotically incorrect descriptions of the velocity decay; however, this approach did demonstrate a radial dependence of E_m. A relation for representing average values of the E_d and E_m for a given cross section of the mixing region was presented; $E_m \approx E_d \approx K\, r_{\frac{1}{2}}\, V_C$, where $r_{\frac{1}{2}}$ is the half boundary of the mixing region of the jet, V_C is the ratio of V at any point on the centerline of the inner jet divided by the initial velocity of the external jet, and K is a constant.

Schetz (30) obtained numerical solutions for a two-dimensional (x-y) free jet (hydrogen in air) and for the related case of a two-dimensional constant pressure jet at the centerline of a duct. Equilibrium chemistry was considered and the channel contours necessary to maintain constant pressure with heat release were obtained. A linearization technique was used and $\rho^2 E_m$ was assumed proportional to the maximum mass flux difference at each axial station.

For coaxial injection along the centerline, Zakkay (18) found that E_m varied significantly in the radial direction when the injected gas was either much lighter or heavier than that of the outer stream. Radial variations were much smaller when both gases had approximately the same molecular weight, and $\epsilon = \bar{\rho} E_m$ was found to be a weaker function of radial position than E_m itself, although considerable variation in ϵ occurred in the hydrogen-air system.

Forde (56) studied mixing in coaxial supersonic compressible streams of CO_2 and air for the region from the nozzle exit to the end of the potential core. He used the mixing similarity parameter, σ (determined from measured velocity ratios), to correlate his data. Average values of σ varied from 15 to 18 as M for the inner CO_2 jet varied from 1.47 to 1.62 in a Mach 1.62 air stream. Experimental values of Sc_T were near 0.92. He concluded that subsonic turbulent mixing theories were applicable for his supersonic conditions when σ was determined empirically.

APPENDIX B

THE ENERGY EQUATION

The energy equation must be included in any general analysis of turbulent mixing because in general T_t will not be the same for the various streams prior to mixing. For steady, axisymmetric flow, the energy equation may be written in the following form for instantaneous quantities (Ref. 1)

$$\rho V_r \frac{\partial h}{\partial r} + \rho V_z \frac{\partial h}{\partial z} = \frac{1}{r}\frac{\partial}{\partial r}\left[kr\frac{\partial T}{\partial r} + \sum_i \rho D_i r h_i \frac{\partial Y_i}{\partial r}\right] +$$

$$\frac{\partial}{\partial z}\left[k\frac{\partial T}{\partial z} + \sum_i \rho D_i h_i \frac{\partial Y_i}{\partial z}\right] + V_r\frac{\partial P}{\partial r} + V_z\frac{\partial P}{\partial z} + \Phi \qquad \text{(B-1)}$$

This equation is considerably simplified if the following assumptions, which are analogous to those discussed with regard to the simplified diffusion and momentum equations are made: 1) energy transferred in the axial direction by conduction and diffusion is negligible compared to that transferred in the radial direction; 2) viscous normal stress and $\partial V_r/\partial z$ are negligible; and 3) $V_z(\partial P/\partial z) \gg V_r(\partial P/\partial r)$. Assumption (2) allows simplification of the dissipation function, Φ, which becomes

$$\Phi \approx \frac{\mu}{g_c}\left(\frac{\partial V_z}{\partial r}\right)^2 \qquad \text{(B-2)}$$

Using these assumptions and time-averaging the resulting equation in the usual way yields (Refs. 1, 19)

$$\overline{\rho V}_r \frac{\partial \bar{h}_t}{\partial r} + \overline{\rho V}_z \frac{\partial \bar{h}_t}{\partial z} = \frac{1}{r}\frac{\partial}{\partial r}\left(\bar{\rho}E_h\, r\frac{\partial \bar{h}_t}{\partial r}\right) +$$

$$\frac{1}{r}\frac{\partial}{\partial r}\left[\sum_i\left(1 - \frac{1}{Le_{T_i}}\right)\bar{\rho}E_{d_i}\, r\bar{h}_i\frac{\partial \bar{Y}_i}{\partial r} + \left(1 - \frac{1}{Pr_T}\right)\bar{\rho}E_m\frac{r}{2g_c}\frac{\partial V_z^2}{\partial r}\right] \qquad \text{(B-3)}$$

1. Determination of E_h, Pr_T, and Le_{T_i}

Equation (B-3) can be integrated in an identical manner to Eqs (18) and (19) to give

$$\frac{\partial}{\partial z}\int_{r^*}^{r_s} \overline{\rho V}_z\, \bar{h}_t r\, dr = \left[\bar{\rho}E_h\, r\frac{\rho \bar{h}_t}{\rho r}\right]_{r^*}^{r_s} +$$

$$\left[\sum_i\left(1 - \frac{1}{Le_{T_i}}\right)\bar{\rho}E_d r_s\,\bar{h}_i\frac{\partial \bar{Y}_i}{\partial r} + \left(1 - \frac{1}{Pr_T}\right)\bar{\rho}E_m\frac{r_s V_z}{g_c}\frac{\partial \bar{V}_z}{\partial r}\right]_{r_s} \qquad \text{(B-4)}$$

if the flow is adiabatic, the first flux term on the right-hand-side of this equation also is zero when evaluated to r^*. This equation can be used to determine Pr_T and Le_{T_i} if experimental stagnation temperature profiles are available. Of course, for cases in which $\bar{T}_t$ was not constant throughout the flow, these profiles would be required for computation of $\bar{T}$, $\bar{\rho}$, and $\bar{V}_z$. The stagnation enthalpy, $\bar{h}_t$, could be computed from $\bar{T}_t$ using the relations

$$\bar{h}_{t_i} = \int_{T_{ref}}^{\bar{T}_t} c_{p_i} \, d\bar{T}_t \tag{B-5}$$

$$\bar{h}_t = \sum_i \bar{Y}_i \bar{h}_{t_i} \tag{B-6}$$

where the c_{p_i} are, of course, functions of temperature, and the static enthalpy could be computed from the relation

$$\bar{h}_i = \bar{h}_{t_i} - \frac{\bar{V}_z^2}{2g_c} \tag{B-7}$$

Since E_{d_i} and E_m can be determined from Eqs. (18) and (19), Sc_{T_i} can be determined from the relation $Sc_{T_i} = E_m/E_{d_i}$; Le_{T_i} can be eliminated from Eq. (B-4) using the identity $Le_{T_i} = Pr_T/Sc_{T_i}$ and Eq. (B-4) solved for Pr_T ($= E_m/E_h$).* Once Pr_T has been determined, E_h and Le_{T_i} can be computed completing the determination of turbulent transport coefficients.

2. Method for Solving the Energy Equation

For a binary mixture, the energy equation can be written in a form analogous to the diffusion and momentum equations (again dropping the bars) as

$$L(r,z) \frac{\partial h_t}{\partial z} = \frac{\partial^2 h_t}{\partial r^2} + M(r,z) \frac{\partial h_t}{\partial r} + N(r,z) + P(r,z) \tag{B-8}$$

---

* $E_h \equiv \kappa/\bar{\rho}\, c_p$; $c_p = \sum_i c_{p_i} \bar{Y}_i$; $\kappa = \sum_i \kappa_i \bar{Y}_i$; $\overline{(\rho V_r)' h_i'} \equiv -\kappa_i \, \partial\bar{T}/\partial r$

where

$$L(r,z) \equiv Pr_T \, V_z/E_m$$

$$M(r,z) \equiv \frac{1}{r} + \frac{1}{\rho}\frac{\partial \rho}{\partial r} + \frac{1}{E_m}\frac{\partial E_m}{\partial r} - \frac{1}{Pr_T}\frac{\partial Pr_T}{\partial r} - Pr_T \frac{V_r}{E_m}$$

$$= E(r,z) - \frac{1}{Pr_T}\frac{\partial Pr_T}{\partial r} + (1-Pr_T)\frac{V_r}{E_m}$$

$$N(r,z) \equiv (Le_T-1)\sum_i h_i \left\{ \frac{\partial^2 Y_i}{\partial r^2} + \left[B(r,z) + \frac{V_r}{E_d} + \frac{1}{h_i}\frac{\partial h_i}{\partial r} + \frac{1}{Le_T}\left(\frac{1}{Le_T-1}\right)\frac{\partial Le_T}{\partial r}\right]\frac{\partial Y_i}{\partial r}\right\}$$

$$P(r,z) \equiv (Pr_T-1)\frac{V_z}{g_c}\left\{ \frac{\partial^2 V_z}{\partial r^2} + \frac{1}{V_z}\left(\frac{\partial V_z}{\partial r}\right)^2 + \left[E(r,z) + \frac{V_r}{E_m} + \frac{1}{Pr_T}\left(\frac{1}{Pr_T-1}\right)\frac{\partial Pr_T}{\partial r}\right]\frac{\partial V_z}{\partial r}\right\}$$

where i designates either hydrogen or air, and B and E are the coefficients defined in Eqs. (28) and (30).

For the case of an adiabatic wall, the boundary conditions for Eq. (B-2) are analogous to those for the diffusion equations. At the wall, $\partial h(r_w,z)/\partial r = 0$, and $\partial h_t(r_w,z)/\partial r = 0$, since $V_z = 0$. Symmetry at the centerline requires that $\partial h(0,z)/\partial r = 0$ and $\partial h_t(0,z)/\partial r = 0$. Therefore, Eq. (B-2) can be solved by the same general procedure used for Eq. (28), provided that the coefficients are evaluated using experimental profiles. Unfortunately, second derivatives of both Y and V_z are needed to evaluate coefficients N and P. Although these terms can be evaluated from experimental profiles, the alternative procedure of solving the diffusion, momentum, and energy equations simultaneously, which avoids the need for differentiation of experimental profiles, is clearly more desirable. In this case Pr_T and Le_T must be known functions of position as well as E_d, E_m, V_r, and P. In addition, either the stagnation enthalpy h_t or temperature T_t must be given (or estimated) at the initial axial location as well as the Y and V_z profiles.

APPENDIX C

NUMERICAL INTEGRATION OF PARABOLIC PARTIAL DIFFERENTIAL EQUATIONS

Diffusion Equation

The application (Ref. 1) of the Crank-Nicolson technique (Ref. 31) to the solution of the diffusion equation, Eq. (28), may be summarized as follows. Partial derivatives with respect to both r and z are approximated at intermediate points (e.g., point P) not part of the grid or mesh from values at six surrounding mesh points [e.g., point (j,n)]. Lines of constant z are designated with n's and lines of constant r with j's.

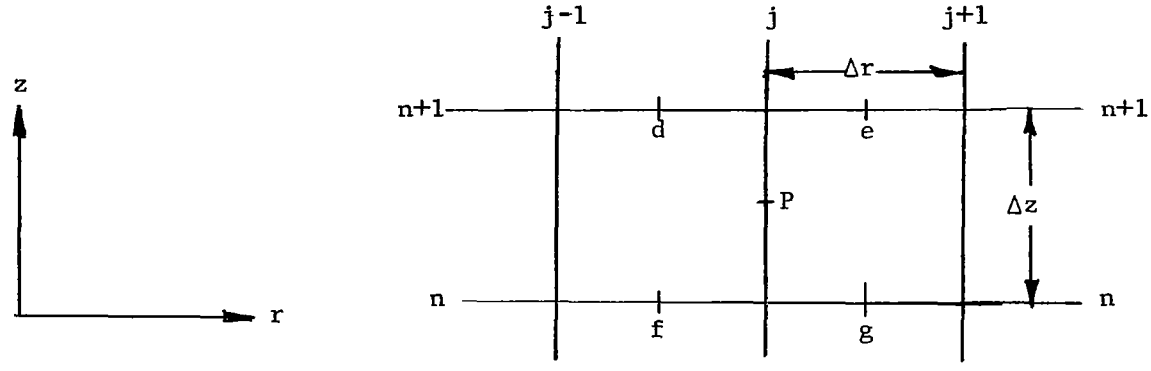

Fig. C-1 Illustration of the Mesh.

The first derivative of Y with respect to z at point P is approximated by

$$(\partial Y/\partial z)_P \simeq \left(Y_{j,n+1} - Y_{j,n}\right)/\Delta z \qquad (C\text{-}1)$$

Similarly,

$$(\partial Y/\partial r)_{j,n+1} \simeq \left(Y_{j+1,n+1} - Y_{j-1,n+1}\right)/2\Delta r \qquad (C\text{-}2)$$

and another equation is obtained at point (j,n). Then $\partial Y/\partial r$ at P is approximated as the average of the derivatives at point (j,n+1) and (j,n) as

$$(\partial Y/\partial r)_P = \frac{1}{2}\left[\left(\partial Y/\partial r\right)_{j,n+1} + \left(\partial Y/\partial r\right)_{j,n}\right]$$
$$= \left[Y_{j+1,n+1} - Y_{j-1,n+1} + Y_{j+1,n} - Y_{j-1,n}\right]/4\Delta r \qquad \text{(C-3)}$$

In a similar manner, $\partial^2 Y/\partial r^2$ at P is obtained from first differences evaluated at points d, e, f, and g; for example,

$$(\partial Y/\partial r)_d = \left(Y_{j,n+1} - Y_{j-1,n+1}\right)/\Delta r \qquad \text{(C-4)}$$

and similar relations apply at e, f, and g. Then at (j,n+1),

$$(\partial^2 Y/\partial r^2)_{j,n+1} = \left[\left(\partial Y/\partial r\right)_e - \left(\partial Y/\partial r\right)_d\right]/\Delta r =$$
$$\left(Y_{j+1,n+1} - 2Y_{j,n+1} + Y_{j-1,n+1}\right)/(\Delta r)^2 \qquad \text{(C-5)}$$

A similar equation is obtained at (j,n), and $\partial^2 Y/\partial r^2$ at P is approximated as the average of these derivatives. Using this result with Eqs. (C-1) and (C-3), Eq. (28) can now be written as a finite difference equation with the coefficients of the various Y's grouped together:

$$\left(\frac{B}{4\Delta r} - \frac{1}{2(\Delta r)^2}\right) Y_{j-1,n+1} + \left(\frac{A}{\Delta z} + \frac{1}{(\Delta r)^2}\right) Y_{j,n+1} - \left(\frac{B}{4\Delta r} + \frac{1}{2(\Delta r)^2}\right) Y_{j+1,n+1}$$
$$= -\left(\frac{B}{4\Delta r} - \frac{1}{2(\Delta r)^2}\right) Y_{j-1,n} + \left(\frac{A}{\Delta z} - \frac{1}{(\Delta r)^2}\right) Y_{j,n} + \left(\frac{B}{4\Delta r} + \frac{1}{2(\Delta r)^2}\right) Y_{j+1,n} \qquad \text{(C-6)}$$

If both sides of Eq. (C-6) are multiplied by $2(\Delta r)^2$, it may be written

$$a_j Y_{j-1,n+1} + b_j Y_{j,n+1} + c_j Y_{j+1,n+1} = \eta_j \qquad \text{(C-7)}$$

where

$$\eta_j = -a_j Y_{j-1,n} + \left(b_j - 4 \right) Y_{j,n} - c_j Y_{j+1,n} \qquad \text{(C-8)}$$

and

$$a_j \equiv \tfrac{1}{2} B\Delta r - 1 \qquad b_j \equiv 2A (\Delta r)^2/\Delta z + 2$$

$$c_j \equiv - (\tfrac{1}{2} B\Delta r + 1)$$

The coefficients A and B are evaluated at P; Eq. (C-8) contains only known Y's, since initial boundary conditions at z = 0 must be given to start the integration; that is, η_j is always known. Eq. (C-7) can be solved for the various Y's most simply by setting up the system of equations as a tridiagonal system (Ref. 31) and solving by a normalized form of Gaussian elimination (Ref. 57) once the boundary conditions Y(0,z) and $Y(r_w,z)$ (which occur at j = 1 and j = M) are specified. The conditions $\partial Y(0,z)/\partial r = 0$ and $\partial Y(r_w,z)/\partial r = 0$ are introduced into the difference equation through Taylor's series expansions about the boundaries. At the centerline, the result,* neglecting terms of second order and higher in Δr, is

$$(\partial Y/\partial r)_0 = - \left(Y_2 - 4Y_1 + 3Y_0 \right)/2\Delta r = 0 \qquad \text{(C-9)}$$

At the wall, since the expansion is about point M where the value of r is greatest, the values of term Δr in the Taylor series expansion are negative, hence the sign changes

$$(\partial Y/\partial r)_M = \left(Y_{M-2} - 4Y_{M-1} + 3Y_M \right)/2\Delta r = 0 \qquad \text{(C-10)}$$

Substituting j = 1 in Eq. (C-7) and j = M - 1 in (C-8) and using Eqs. (C-9) and (C-10) to eliminate Y_0 and Y_M gives

*The second subscript n+1 is omitted from the Y's since it is common to each of them.

$$(4\,a_1/3 + b_1)\,Y_{1,n+1} + (c_1 - a_1/3)\,Y_{2,n+1} = \eta_1 \qquad \text{(C-11)}$$

$$\left(a_{M-1} - c_{M-1}/3\right) Y_{M-2,\,n+1} + \left(b_{M-1} + 4\,c_{M-1}/3\right) Y_{M-1,\,n+1} = \eta_{M-1} \qquad \text{(C-12)}$$

Defining these special coefficients by the relations

$$b_1' \equiv 4\,a_1/3 + b_1\,; \qquad c_1' \equiv c_1 - a_1/3$$

$$a_{M-1}' \equiv a_{M-1} - c_{M-1}/3\,; \qquad b_{M-1}' \equiv b_{M-1} + 4\,c_{M-1}/3$$

allows Eq. (C-7) to be written in matrix form as

$$QY = \eta \qquad \text{(C-13)}$$

The technique for solving Eq. (C-13) for the various Y's is demonstrated by considering only four values of j, which illustrate each of the two different types of regions: boundary and interior. It may be readily generalized to any number of j's. The tridiagonal matrix Q in this simple case becomes

$$Q = \begin{pmatrix} b_1' & c_1' & 0 & 0 \\ a_2 & b_2 & c_2 & 0 \\ 0 & a_3 & b_3 & c_3 \\ 0 & 0 & a_4' & b_4' \end{pmatrix} = LU = \begin{pmatrix} \beta_1 & 0 & 0 & 0 \\ \ell_2 & \beta_2 & 0 & 0 \\ 0 & \ell_3 & \beta_3 & 0 \\ 0 & 0 & \ell_4 & \beta_4 \end{pmatrix} \begin{pmatrix} 1 & U_1 & 0 & 0 \\ 0 & 1 & U_2 & 0 \\ 0 & 0 & 1 & U_3 \\ 0 & 0 & 0 & 1 \end{pmatrix} \qquad \text{(C-14)}$$

Carrying out the matrix multiplication L x U indicated in Eq. (C-14), and associating the elements with corresponding elements in Q yields relations from which the β's can be determined as

$$\beta_1 = b_1'\,;\ \beta_2 = b_2 - a_2 c_1'/\beta_1\,;\ \beta_3 = b_3 - a_3 c_2/\beta_2\,;\ \beta_4 = b_4' - a_4' c_3/\beta_3 \qquad \text{(C-15)}$$

Now let

$$Y = \begin{pmatrix} Y_1 \\ Y_2 \\ Y_3 \\ Y_4 \end{pmatrix} = UY = \begin{pmatrix} 1 & U_1 & 0 & 0 \\ 0 & 1 & U_2 & 0 \\ 0 & 0 & 1 & U_3 \\ 0 & 0 & 0 & 1 \end{pmatrix} \begin{pmatrix} Y_1 \\ Y_2 \\ Y_3 \\ Y_4 \end{pmatrix} \qquad \text{(C-16)}$$

and write

$$L\,\gamma = \eta \tag{C-17}$$

Expanding these matrices, substituting the terms obtained from Eq. (C-14) and equating corresponding terms yields

$$\gamma_1 = \frac{\eta_1}{\beta_1}\ ;\ \gamma_2 = \frac{\eta_2 - a_2\gamma_1}{\beta_2}\ ;\ \gamma_3 = \frac{\eta_3 - a_3\gamma_2}{\beta_3}\ ;\ \gamma_4 = \frac{\eta_4 - a_4'\gamma_3}{\beta_4} \tag{C-18}$$

Expanding Eq. (C-16) and using terms obtained from (C-14) gives

$$Y_1 = \gamma_1 - c_1'Y_2/\beta_1\ ;\ Y_2 = \gamma_2 - c_2Y_3/\beta_2\ ;\ Y_3 = \gamma_3 - c_3Y_4/\beta_3\ ;\ Y_4 = \gamma_4 \tag{C-19}$$

Equations (C-15), (C-18), and (C-19) may be generalized to include more than four radial positions by writing

$$\beta_1 = b_1 \qquad \beta_j = b_j - a_jc_{j-1}/\beta_{j-1} \qquad j = 2,\ldots,\ M-1 \tag{C-20}$$

$$\gamma_1 = \eta_1/\beta_1 \qquad \gamma_j = \eta_j - a_j\gamma_{j-1}/\beta_j \qquad j = 2,\ldots,\ M-1 \tag{C-21}$$

$$Y_{M-1} = \gamma_{M-1} \qquad Y_j = \gamma_j - c_jY_{j+1}/\beta_j \qquad j = M-2,\ldots,\ 1 \tag{C-22}$$

where b_1, c_1, a_{M-1}, and b_{M-1} are understood to be primed quantities. The various β's and γ's are first determined using Eq. (C-20) and (C-21), then the term Y_{M-1} is computed and each preceding value of Y by using Eq. (C-22). By this procedure M-1 simultaneous equations are solved for the M-1 values of Y.

Momentum Equation

The numerical solution of the momentum equation, Eq. (30), is similar to the foregoing, but some modification is required because 1) the momentum equation is non-linear, so that an iterative procedure is required, 2) the boundary condition at the wall requires that there be no slip at the wall, and 3) the momentum equation has an additional term if axial pressure gradients exist in the flow. Since Eq. (30) is identical in form to Eq. (28), except for the added term F(r,z), Eq. (C-6) may be applied by simply changing

the "Y's" to "V_z's", adding the term F(r,z) to the right-hand side, and changing A to C and B to E. When the equivalent of Eq. (C-6) is multiplied by $2(\Delta r)^2$, there results

$$e_j V_{z_{j-1,\,n+1}} + f_j V_{z_{j,\,n+1}} + g_j V_{z_{j+1,\,n+1}} = \zeta_j \qquad \text{(C-23)}$$

$$\zeta_j = - e_j V_{z_{j-1,\,n}} + (f_j - 4) V_{z_{j,\,n}} - g_j V_{z_{j+1,\,n}} + h_j \qquad \text{(C-24)}$$

$$e_j \equiv \tfrac{1}{2}E\Delta r - 1 \qquad f_j \equiv 2C\,(\Delta r)^2/\Delta z + 2$$

$$g_j \equiv - (\tfrac{1}{2}E\Delta r + 1) \qquad h_j \equiv 2(\Delta r)^2 F$$

The boundary condition along the axis, $\partial V_z\,(0,z)/\partial r = 0$, produces, when j = 1, an equation analogous to (C-11).

Unlike the diffusion case (no mass flux to the wall), a momentum flux to the wall exists because of friction. The boundary condition becomes $V_z(r_w,z) = 0$. Therefore, when j = M-1, $V_{z_M} = 0$, and Eq. (C-23) simply becomes

$$e_{M-1} V_{z_{M-2,\,n+1}} + f_{M-1} V_{z_{M-1,\,n+1}} = \zeta_{M-1} \qquad \text{(C-25)}$$

Therefore, the special primed coefficients for the momentum equation become

$$f_1' \equiv \frac{4}{3} e_1 + f_1\,; \quad g_1' \equiv g_1 - \frac{1}{3} e_1\,; \quad e'_{M-1} = e_{M-1}\,; \text{ and } f'_{M-1} \equiv f_{M-1}$$

Equation (C-23) can now be written in matrix form analogous to Equation (C-13) and solved by the same technique of normalized Gaussian elimination [see Eqs. (C-20-22)]. The only difference in procedure is the need for an iteration, which is required by the non-linearity of the momentum equation. Initially the value of the coefficient C, which depends on V_z, is not known at point P in Fig. C-1. For the first iteration, the known value of V_z at j,n is used in computing C, and a V_z is obtained at j, n+1 using equations analogous to (C-20-22). For the second iteration, the average of these two V_z's is used in computing an improved value of C, and so on. Test cases showed that three iterations were sufficient, so three were used in subsequent calculations.

Variable Grid Spacing

Initial solutions of the diffusion equation showed the need for very fine mesh near the wall because the required boundary condition $\partial Y/\partial r = 0$ was approached by the experimental data only in the region extremely close to the wall [see Figs. 6(a) and 7(a)]. The finer the mesh spacing, the smaller was the region influenced by the boundary conditions and the better the agreement between computed and experimental profiles. Since a fine mesh increased computing time significantly, a logarithmic variation in spacing was obtained by changing the variable in the partial differential equation from r to a new variable w:

$$w = b^{(r_w - r)/r_w} \tag{C-26}$$

so that

$$r = r_w + (\ell n\ w)/\alpha \quad ; \quad \alpha \equiv -(\ell n\ b)/r_w \tag{C-27}$$

The base, b, was an arbitrary constant; its value depended on the application.

The transformation will be illustrated for the momentum equation (the diffusion equation is identical in form but with the term $F \equiv 0$). The change of variables was made in Eq. (30) by writing it as

$$C\,\frac{\partial V_z}{\partial z} = \frac{\partial}{\partial r}\left(\frac{\partial V_z}{\partial w}\,\frac{dw}{dr}\right) + E\,\frac{\partial V_z}{\partial w}\,\frac{dw}{dr} + F \tag{C-28}$$

which can be expanded and rewritten to give

$$C'\,\partial V_z/\partial z = \partial^2 V_z/\partial w^2 + E'\,\partial V_z/\partial w + F' \tag{C-29}$$

where

$$C' \equiv \frac{C}{(dw/dr)^3} \quad ; \quad E' \equiv \frac{E\,dw/dr + d^2w/dr^2}{(dw/dr)^2} \quad ; \quad F' \equiv \frac{F}{(dw/dr)^3}$$

Equation (C-29) is identical in form to Eq. (30) except that the variable r has been changed to the variable w; therefore, the terms e, f, g, and h in Eqs. (C-23) and (C-24) can be transformed directly by substituting Δw

for Δr, with no other change in the method of solution, as long as the prime coefficients defined in Eq. (C-29) are used. These coefficients were evaluated using the relations

$$\frac{dw}{dr} = \alpha b^{(r_w - r)/r_w} = \alpha w; \quad \frac{d^2w}{dr^2} = \alpha \frac{dw}{dr} = \alpha^2 w \tag{C-30}$$

from which

$$C' \equiv C/\alpha^2 w^2 \quad ; \quad E' \equiv (E/\alpha + 1)/w \; ; \quad F' \equiv F/\alpha^2 w^2 \tag{C-31}$$

The effect of various values of b on the radial grid spacing is shown in Fig. C-2; the value of w is always between b and 1.0, while $0 < r < r_w$. The nearer b is to unity, the smaller is the region in which w exists, and the more nearly linear is the transformation from r to w.

Convergence effects are illustrated in Fig. C-3 for the diffusion equation. After an integration of 5.5 in., 101 logarithmically distributed radial grid points with b = 0.001 yield a valid solution, but 101 approximately equally spaced grid points with b = 0.90 do not. The extremely non-linear mesh resulting when b = 0.001 was not satisfactory for solving the momentum equation, however; b = 0.90 did yield valid solutions.

REFERENCES

1. Morgenthaler, J. H.: Supersonic Mixing of Hydrogen and Air. Ph.D. Thesis, University of Maryland (June 1965). Microfilm copies available from University Microfilms, Inc., (Order No. 66-1358).

2. Weber, R. J., and MacKay, J. S.: An Analysis of Ramjet Engines Using Supersonic Combustion. NACA TN 4386 (1958).

3. Dugger, G. L.: Comparison of Hypersonic Ramjet Engines with Subsonic and Supersonic Combustion. Combustion and Propulsion Fourth AGARD Colloquium, pp. 84-119, Pergamon Press, New York (1961).

4. McLafferty, G. H.: Relative Thermodynamic Efficiency of Supersonic Combustion and Subsonic Combustion Hypersonic Ramjets. ARS J., 30, 1019-1021 (1960).

5. Mordell, D. L., and Swithenbank, J.: Hypersonic Ramjets. Second International Congress for the Aeronautical Sciences, Advances in Aeronautical Sciences, vol. 4, pp. 831-848, Pergamon Press, New York (1962).

6. Ferri, A.: Review of Problems in Application of Supersonic Combustion. J. Roy. Aeronaut. Soc., 68, 575-597 (Sept. 1964).

7. Olson, W. T.: Recombination and Condensation Processes in High Area Ratio Nozzles. ARS J., 32, 672-680 (1962).

8. Gross, R. A., and Chinitz, W.: A Study of Supersonic Combustion. J. Aerospace Sci., 27, 517-524, 534 (1960).

9. Rubins, P. M., and Cunningham, T. H. M.: Shock-Induced Supersonic Combustion in a Constant-Area Duct. J. Spacecraft and Rockets, 2, 199-205 (1965).

10. Nicholls, J. A.: Standing Detonation Waves. Ninth Symposium (International) on Combustion, pp. 488-496, Academic Press, New York (1963).

11. Rubins, P. M.: Experimental Standing-Wave Shock-Induced Combustion for Determining Reaction Kinetic Histories (Abstract), AIAA Bulletin, 2, 227 (1965).

12. Ferri, A., Libby, P. A., and Zakkay, V.: Theoretical and Experimental Investigations of Supersonic Combustion. Aeronautical Research Laboratories, USAF, ARL-62-467, PIBAL Rept. No. 713, AD 291712 (1962).

13. Dugger, G. L.: Comments on High Performance Combustion Systems. International Astronautical Congress, 12th, Proceedings, pp. 715-727, Academic Press, New York (1963).

14. Vranos, A., and Nolan , J. J.: Supersonic Mixing of a Light Gas and Air (Abstract). AIAA Bulletin, 2, 209 (1965).

15. Hinze, J. O.; Turbulence; An Introduction to its Mechanism and Theory. Chapters 1, 5, 6, McGraw-Hill, New York (1959).

16. Pai, S. I.: Fluid Dynamics of Jets. Chapters V, VI, VII, Van Nostrand, New York (1954).

17. Zakkay, V., Krause, E., and Woo, S. D. L.: Turbulent Transport Properties for Axisymmetric Heterogeneous Mixing. AIAA J., 2, 1939-1947 (1964).

18. Zakkay, V., and Krause, E.: The Radial Variation of the Eddy Viscosity in Compressible Turbulent Jet Flows. Int. J. Heat Mass Transfer, 8, 1047-1050 (1965).

19. Morgenthaler, J. H.: Mixing in Supersonic Flow. General Applied Science Laboratories, Inc., Westbury, L.I., New York, GASL Tech. Rept. 592 (Sept. 1966).

20. Levenspiel, O.: Chemical Reaction Engineering, p. 262, Wiley, New York (1962).

21. Howe, N. M., Jr., Shipman, C. W., and Vranos, A.: Turbulent Mass Transfer and Rates of Combustion in Confined Turbulent Flames. Ninth Symposium (International) on Combustion, pp. 36-47, Academic Press, New York (1963).

22. Wylie, C. R., Jr.: Advanced Engineering Mathematics, p. 591, McGraw-Hill, New York (1951).

23. Clippinger, R. F.: Supersonic Axially Symmetric Nozzles. Ballistic Research Laboratories, Aberdeen Proving Ground, Md., BRL Rept. 794 (1951).

24. Alpinieri, L. J.: Turbulent Mixing of Coaxial Jets. AIAA J., 2, 1560-1567 (1964).

25. Kopal, Z.: Tables of Supersonic Flow about Cones. M.I.T. Tech. Rept. No. 1 (1947).

26. Longwell, J. P., and Weiss, M. A.: Mixing and Distribution of Liquids in High Velocity Air Streams. Ind. Eng. Chem., 45, 667-677 (1953).

27. Forstall, W., Jr., and Shapiro, A. H.: Momentum and Mass Transfer in Coaxial Gas Jets. J. Appl. Mech., 17, 399-408 (1950).

28. Rohsenow, W. M., and Choi, H. Y.: Heat, Mass, and Momentum Transfer. Chapter 3, Prentice-Hall, Englewood Cliffs, New Jersey (1961).

29. Kleinstein, G.: Mixing in Turbulent Axially Symmetric Free Jets. J. Spacecraft and Rockets, 1, 403-408 (1964).

30. Schetz, J. A.: Supersonic Diffusion Flames. Supersonic Flow, Chemical Processes and Radiative Transfer, pp. 79-91, Pergamon Press, New York (1964).

31. Douglas, J., Jr.: A Survey of Numerical Methods for Parabolic Differential Equations. Advances in Computers, vol. 2, pp. 1-54, Academic Press, New York (1961).

32. Abramovich, G. N.: Theory of Turbulent Jets. Translation by Scripta Technica. Chapters II, VII, M.I.T. Press, Cambridge, Massachusetts (1963).

33. Pai, S. I.: Viscous Flow Theory. Vol. II - Turbulent Flow. Chapter VIII, Van Nostrand, Princeton, New Jersey (1957).

34. Tollmien, W.: Calculation of Turbulent Expansion Processes. Zamm., 6, 468-478 (1926). Translated in NACA TM 1085 (1945).

35. Schlichting, H.: Laminar Jet Propagation. Zamm., 13, 260 (1933).

36. Kuethe, A. M.: Investigation of the Turbulent Region Formed by Jets. Trans. ASME, 57, A87 (1935).

37. Squire, H. B., and Trouncer, J.: Round Jets in a General Stream. Aeronautical Research Committee R. & M. No. 1974 (1944).

38. Reichardt, H.: A New Theory of Free Turbulence. Zamm., 21, 257-264 (1941). Translated in J. Roy. Aeronaut. Soc., 47, 167-176 (1943).

39. Görtler, H.: A New Approximate Method for the Numerical Evaluation of Free Turbulence Problem. Zamm., 22, 244-254 (1942). Translated in ARC 7947, FM 718, RTP Translation No. 2234.

40. Szablewski, W.: Contributions to the Theory of the Spreading of a Free Jet Issuing from a Nozzle. NACA TM 1311 (1951); report originally published in German (1944).

41. Szablewski, W.: The Diffusion of a Hot Air Jet in Air in Motion. NACA TM 1288 (1950); report originally published in German (1946).

42. Page, F., Jr., Schlinger, W. G., Breaux, D. K., and Sage, B. H.: Point Values of Eddy Conductivity and Viscosity in Uniform Flow Between Parallel Plates. Ind. Eng. Chem., 44, 424-430 (1952).

43. Morkovin, M. V.: On Eddy Diffusivity, Quasi-Similarity, and Diffusion Experiments in Turbulent Boundary Layers. AIAA Paper No. 64-432 (1964).

44. Ruden, P.: Propagation of Turbulence in a Free Jet. Die Naturwissenschaften, 21, 375-378 (1933).

45. Corrsin, S., and Uberoi, M. S.: Further Experiments on the Flow and Heat Transfer in a Heated Turbulent Air Jet. NACA TN 1865 (1949).

46. Keagy, W. R., and Weller, A. E.: Proceedings of the Heat Transfer and Fluid Mechanics Institute. pp. 89-98, ASME, New York (1949).

47. Squire, H. B.: Jet Flow and Its Effects on Aircraft. Aircraft Engineering, 22, 62-67 (1950).

48. Pai, S. I.: Two-Dimensional Jet Mixing of a Compressible Fluid. J. Aerospace Sci., 16, 463-469 (1949).

49. Pai, S. I.: Axially Symmetrical Jet Mixing of a Compressible Fluid. Quart. Appl. Math., 10, 141-148 (1952).

50. Pai, S. I.: Laminar Jet Mixing of Two Compressible Fluids with Heat Release. J. Aeronaut. Sci., 23, 1012-1018 (1956).

51. Alexander, L. G., Baron, T., and Comings, E. W.: Transport of Momentum, Mass, and Heat in Turbulent Jets. Univ. of Illinois Bulletin No. 413 (1953).

52. Schlichting, H.: Boundary Layer Theory. 4 ed., Chapters VII, XVIII, XXIII, McGraw-Hill, New York (1962).

53. Vasiliu, J.: Turbulent Mixing of a Rocket Exhaust Jet with a Supersonic Stream Including Chemical Reactions. J. Aerospace Sci., 29, 19-28 (1962).

54. Libby, P. A.: Theoretical Analysis of Turbulent Mixing of Reactive Gases with Application to Supersonic Combustion of Hydrogen. ARS J., 32, 388-396 (1962).

55. Kleinstein, G.: An Approximate Solution for the Axisymmetric Jet of a Laminar Compressible Fluid. Quar. Appl. Math., 20, 49-54 (1962).

56. Forde, J. M.: An Experimental Investigation of the Mixing of Supersonic Turbulent Streams on Non-Similar Fluids. Hypersonic and Propulsion Laboratory, McGill Univ., Montreal, Canada, Rept. 63-3 (1963).

57. Faddeeva, V. N.: Computational Methods of Linear Algebra. Chapter 2, Dover, New York (1959).

Table 1

Thermal Conductivity Cell Calibration

Orifice diameter, mm		K (gm/sec-atm)
Air	0.523	0.0465
Hydrogen	0.201	0.00178

Upstream orifice pressure, in. Hg		Hydrogen concentration, mole percent
Air	Hydrogen	
400	0	0.0
400	100	12.1
400	200	21.6
400	300	29.3
400	350	32.6
300	300	35.7
200	300	45.6
100	300	62.4
100	350	65.9
80	300	67.6
80	350	70.9
0	350	100.0

Table 2

Summary of Run Conditions, Mach 2 Air
Constant Parameters: C_D Hydrogen Venturi = 0.932; C_D Nozzle = 1.00

Axial length, in.	Hydrogen flow, $\dot{m}_h$ lb/sec	Air flow, $\dot{m}_a$ lb/sec	Injector C_D	Pressure, psia					Temperature, °R			Computed from streamtube sums		
				P_{t_a}	P_{t_h}	$P_{t_{hv}}$	P_w	P_{we}	T_{t_a}	T_{t_h}	$T_{t_{hv}}$	$\dot{m}_a+\dot{m}_h$ lb/sec	$\dot{m}_h$ lb/sec	Momentum,++ lbf
A. Radial injection through 0.0052-in. slot; 1.00-in. I.D. test section														
0.05	0.	1.08	--	95	--	--	--	13.6	488	--	--	1.11	--	53.0
	0.0052	1.08	0.868	95	59	184	**	15.4	488	509	511	1.10	0.0046	51.8
	0.0107	1.07	0.904	95	116	375	**	11.3	488	506	507	1.01	0.0127	53.9
0.4	0.	1.05	--	95	--	--	17.8	14.0	510	--	--	1.07	--	52.4
	0.0051	1.06	0.815	95	64	188	16.4	15.4+	506	547	533	1.06	0.0044	51.1
	0.0100	1.07	0.848	96	121	369	17.4	21.1+	507	549	552	1.09	0.0084	47.9
	0.0152	1.04	0.866	94	179	555	27.9	27.9+	507	545	546	1.12	0.0090	42.3
1.4	0.*	1.08	--	97	--	--	14.6	14.8	508	--	--	1.11	--	53.5
	0.0052	1.05	0.820	93	63	184	16.0	15.2	489	506	507	1.01	0.0050	48.0
	0.0109	1.11	0.834	96	128	384	26.6	23.1	474	507	507	1.15	0.0085	46.5
2.9	0.	1.04	--	94	--	--	14.3	14.6	510	--	--	1.06	--	50.9
	0.0050	1.06	0.788	95	65	184	16.5	17.2	510	547	551	1.06	0.0039	49.2
	0.0100	1.05	0.814	96	126	368	26.8	23.6	515	549	550	1.10	0.0071	45.5
	0.0155	1.05	0.843	95	186	565	30.6	30.5	515	547	547	1.16	0.0116	39.6
5.9	0.	1.05	--	95	--	--	14.6	14.9	511	--	--	1.06	--	50.4
	0.0050	1.05	0.777	95	65	184	16.6	19.4	515	545	547	1.07	0.0034	47.1
	0.0100	1.05	0.809	95	127	367	26.1	26.0	515	547	547	1.08	0.0080	41.9
	0.0153	1.05	0.816	95	189	557	33.8	32.2	516	547	548	1.08	0.0148	38.4
B. Axial injection through 0.0055-in. slot; 1.04-in. I.D. test section														
0.775	0.*	1.07	--	96	--	--	**	12.9†	502	--	--			
	0.004*	1.09	--	97	85	146	**	13.4†	500	513	517			
	0.008*	1.10	--	97	164	289	**	14.3†	490	512	515			
	0.016*	1.11	--	98	264	559	**	15.2†	490	507	508			
3.4	0.004*	1.12	--	98	51	148	15.3	14.7	483	513	515			
	0.008*	1.11	--	97	96	284	14.1	16.1	484	514	516			
	0.016*	1.12	--	98	185	566	13.6	20.4	486	516	517			

* Probe I.D. was 0.013 in. for these cases; 0.010 for all others.
** Data not available.
++ Computed axial momentum at exit plane of nozzle, assuming one-dimensional isentropic expansion = 54 lbf (excluding PA term)
† Obtained from subsequent tests.

Table 3

Summary of Run Conditions, Mach 3 Air
Constant Parameters: C_D Hydrogen Venturi = 0.932; C_D Nozzle = 0.960

Radial Injection					Pressure, psia					Temperature, °R			Computed from streamtube sums		
Axial length, in.	Diam. Test Sect., in.	Hydrogen flow, $\dot{m}_h$, lb/sec	Air flow, $\dot{m}_a$ lb/sec	Injector C_D	P_{t_a}	P_{t_h}	$P_{t_{hv}}$	P_w	P_{we}	T_{t_a}	T_{t_h}	$T_{t_{hv}}$	$\dot{m}_a+\dot{m}_h$, lb/sec	$\dot{m}_h$ lb/sec	Momentum, +++ lbf
1.65+	1.009	0.0084	1.99	0.654	490	138	293	15.8	17.9	488	493	493	2.11	0.0088	124
2.9++	1.001	0.	1.96	--	496	--	--	14.5	15.6	513	--	--	2.08	--	123
		0.0103	1.98	0.953	497	109	372	19.2	18.1	509	533	535	1.97	0.0076	115
3.4+	1.009	0.	1.96	--	472	--	--	13.2	13.6	477	--	--	1.93	--	111
4.9+	1.008	0.	1.98	--	483	--	--	13.7	12.8	472	--	--	1.88	--	109
		0.0083	2.04	0.854	490	104	286	15.2	16.1	464	492	492	1.96	0.0050	109
5.9++	1.001	0.	1.97	--	500	--	--	14.7	15.1	519	--	--	2.03	--	122
		0.0102	1.98	0.785	497	132	372	19.4	19.6	510	541	543	1.98	0.0072	112

+ Injection slot width = 0.0047 in.; Probe I.D. = 0.013 in.; brass test section

++ Injection slot width = 0.0052 in.; Probe I.D. = 0.010 in.; stainless steel test section

+++ Computed axial momentum at exit plane of nozzle, assuming one-dimensional isentropic expansion = 122-128 lbf (excluding PA term)

Table 4

Computed E_d and V_r for Mach 2
Air with Radial Hydrogen Injection at 0.005 lb/sec
(from Data of Fig. 6)

Distance from wall, mils	Case 1: Five Lengths, Fourth-Order Polynomial					Case 2: Four Lengths, Second-Order Polynomial			
	Axial length, in.:					Axial length, in:			
	0.05	0.4	1.4	2.9	5.9	0.4	1.4	2.9	5.9
	a) E_d, Eddy Diffusivity of Mass, (ft^2/sec) x 10^3								
0	0	0	0	0	0	0	0	0	0
5	25	23	2	13	-24	9	17	7	1
10	29	27	8	20	-29	11	23	12	7
15	35	34	14	23	-35	16	30	13	18
20	41	42	19	29	-44	24	34	17	31
25	49	45	23	39	-57	26	34	22	40
30	102	26	24	50	-72	18	31	27	46
35	235	22	24	67	-84	20	28	32	49
40	4720	19	22	93	-95	26	25	42	51
45	11200	13	21	128	-110				
50	9300	-5	21	165	-130	33	24	70	64
70						-46	46	139	137
100	0	0	93	899	-581	0	146	316	245
	b) V_r, Radial Velocity, ft/sec								
0	0	0	0	0	0	0	0	0	0
5	13	5.5	0.2	2.0	-2.1	2.6	1.0	0.5	0.04
10	26	6.1	0.8	3.6	-3.5	3.6	1.7	1.1	0.5
15	23	4.6	1.4	6.4	-7.0	3.7	2.1	1.8	1.2
20	18	0.9	1.7	9.3	-8.5	3.2	2.4	2.4	1.9
25	15	-4.2	1.8	10	-9.6	2.6	2.6	2.9	2.5
30	6.6	-7.7	2.2	12	-11	1.6	2.7	3.3	2.9
35	0.1	-11	2.6	13	-12	0.3	2.7	3.6	3.3
40	-3.2	-15	2.7	14	-13	-1.3	2.5	3.8	3.6
45	-3.9	-19	2.7	15	-15				
50	-4.0	-23	2.4	16	-16	-5.4	1.8	3.7	4.0
70						-11	-0.1	3.2	3.9
100	-40	-39	-1.4	17	-19	-14	-2.5	2.2	3.5

Table 5

Computed E_d and V_r for Mach 2
Air with Radial Hydrogen Injection at 0.010 lb/sec
(from data of Fig. 7)

Distance from wall, mils	Case 1: Five Lengths, Fourth-Order Polynomial					Case 2: Four Lengths, Second-Order Polynomial			
	Axial length, in.:					Axial length, in.:			
	0.5	0.4	1.4	2.9	5.9	0.4	1.4	2.9	5.9
	a) E_d, Eddy Diffusivity of Mass, (ft^2/sec) x 10^3								
0	0	0	0	0	0	0	0	0	0
5	3	37	13	20	-81	13	47	18	-46
10	-12	46	24	35	-152	23	88	30	-97
15	-443	132	95	18	-66	57	215	37	-107
20	395	127	171	4	15	52	290	51	-115
25	287	142	206	1	48	58	307	73	-106
30	162	173	224	15	36	78	321	82	-86
35	115	247	208	38	8	126	300	86	-81
40	127	231	164	67	-37	126	234	90	-78
45	249	200	131	105	-97	112	189	101	-74
50	1360	195	119	153	-161	117	184	116	-68
100	0	0	29	404	-763	0	229	118	21
	b) V_r, Radial Velocity, ft/sec								
0	0	0	0	0	0	0	0	0	0
5	18	20	2	-0.2	-0.2	5.9	4.5	.53	-1.0
10	76	26	6	-2.5	2.8	11	8.1	.95	-1.9
15	129	31	11	-4.9	6.3	16	11	1.2	-2.6
20	159	34	14	-6.8	9.9	19	13	1.4	-3.1
25	169	34	17	-8.1	11	22	14	1.6	-3.4
30	152	33	18	-8.7	13	24	14	1.7	-3.6
35	106	33	19	-8.8	13	27	15	1.8	-3.7
40	60	32	18	-8.5	13	30	15	1.9	-3.6
45	30	31	18	-8.0	12	32	15	1.9	-3.6
50	9	30	18	-7.5	12	34	14	1.9	-3.4
100	-5	25	10	-3.1	4.9	30	8.9	1.2	-2.1

Table 6

Computed E_d and V_r for Mach 2
Air with Radial Hydrogen Injection at 0.015 lb/sec
(from data of Fig. 8)

Distance from wall, mils	Three Lengths, Second-Order Polynomial		
	Axial length, in.:		
	0.4	2.9	5.9
a) E_d, Eddy Diffusivity of Mass, $(ft^2/sec) \times 10^3$			
0	0	0	0
5	10	7	-2
10	16	11	-4
15	30	23	-8
20	59	42	-14
25	118	69	-17
30	98	123	-18
35	73	231	-15
40	78	372	-13
50	107	153	-2
60	151	80	15
80	250	100	39
100	412	86	53
120	368	61	55
140	0	25	20
b) Radial Velocity, ft/sec			
0	0	0	0
5	2.0	0.4	0.02
10	3.3	0.7	-0.06
15	4.9	0.9	-0.2
20	6.6	1.1	-0.3
25	8.3	1.4	-0.4
30	9.9	1.6	-0.5
35	11	1.8	-0.5
40	12	2.0	-0.4
50	14	2.3	-0.2
60	14	2.6	0.04
80	14	3.0	0.6
100	12	3.0	1.2
120	8.9	3.0	1.7
140	0	2.6	2.0

Table 7

Typical Values of Coefficients Used in Solving Diffusion Equation*

Calculations for Data Presented in Fig. 7 at L = 2.9 in.
Integration started from L = 0.4 in.; E_{d_I} (see Table 9) and V_{r_I} = 15 ft/sec; Radial grid points = 101;
b = 0.001; Initial Δz = 0.0031; Maximum Δz = 0.09 in.;
Criteria for increasing Δz by $\sqrt{2}$: $Y_{wall,n+1} - Y_{wall,n} < 0.01$

Distance from wall mils	$E_{d'}$ ft²/sec	V_z ft/sec	ρ lb/ft³	$\frac{1}{r}$ ft⁻¹	$\frac{\partial}{\partial r} \ell n\, \rho$ ft⁻¹	$\frac{\partial}{\partial r} \ell n\, E_d$ ft⁻¹	$-V_r/E_{d'}$ ft⁻¹	A, ft⁻¹	B, ft⁻¹	A' ft	B'
0**	0.0006	1018	0.097	24.0	-200.8	-26,400	-25,300	1,700,000	-51,800	61.7	-312
7.6	0.018	1146	0.105	24.4	-93.7	-3,950	-849	64,200	-4,870	2.88	-31.6
16.1	0.123	1193	0.111	24.8	-68.5	-1,660	-124	9,730	-1,820	0.55	-12.5
25.8	0.253	1222	0.116	25.3	-52.0	-280	-59.9	4,830	-366	0.36	-1.73
36.9	0.231	1244	0.121	25.9	-39.3	364	-65.7	5,390	285	0.54	4.53
50.1	0.150	1249	0.126	26.7	-32.0	443	-101	8,330	337	1.21	6.06
66.2	0.134	1271	0.131	27.7	-32.6	359	-113	9,500	241	2.15	6.13
87.0	0.113	1286	0.140	29.1	-38.2	216	-134	11,400	73.0	4.58	4.79
116.2	0.100	1313	0.151	31.3	-26 5	88.2	-152	13,100	-58.6	11.9	3.22
166.0	0.100	1367	0.167	35.9	-15.6	64.3	-152	13,700	-66.9	48.9	5.91
500.0**	0.100	1297	0.169	--	0.3	0	-152	13,000	--	472,100.	--

* $A = \frac{V_z}{E_d}$; $B = \frac{1}{r} + \frac{\partial}{\partial r} \ell n\, \rho + \frac{\partial}{\partial r} \ell n\, E_d - \frac{V_r}{E_d}$ [see Eq. (28)]

$A' = A\left(\frac{dw}{dr}\right)^{-2}$; $B' = B\left(\frac{dw}{dr}\right)^{-1} + \frac{d^2w}{dr^2}\left(\frac{dw}{dr}\right)^{-2}$ [see Appendix C]

** Coefficients computed for end points were not used; concentrations were obtained from boundary conditions.

Table 8

Comparison of Experimental and Computed Concentration Profiles at Three Downstream Stations
Radial Hydrogen Injection, Mach 2 Air (Fig. 6); Injection Slot = 0.0052 in., $\dot{m}_h$ = 0.005 lb/sec, $\dot{m}_a$ = 1.06 lb/sec

Distance from wall, mils	z = 0.4 in.	z = 1.4 in.				z = 2.9 in.				z = 5.9 in.			
	Initial Profile		Computed				Computed				Computed		
	Y_{exp}	Y_{exp}	Y_I	Y_{II}	Y_{III}	Y_{exp}	Y_I	Y_{II}	Y_{III}	Y_{exp}	Y_I	Y_{II}	Y_{III}
0	.225	.102	.072	.088	.117	.060	.044	.049	.064	.028	.028	.030	.033
7.6	.151	.092	.067	.074	.086	.051	.043	.046	.054	.026	.028	.029	.031
16.1	.078	.074	.058	.053	.062	.037	.040	.042	.045	.020	.027	.028	.030
25.8	.044	.060	.047	.038	.042	.024	.037	.038	.037	.017	.026	.027	.026
36.9	.012	.040	.030	.020	.024	.015	.030	.030	.027	.014	.023	.022	.023
50.1	.003	.019	.011	.005	.009	.009	.017	.018	.015	.009	.018	.014	.017
66.2	.001	.007	.002	.001	.002	.005	.006	.006	.006	.006	.010	.007	.010
87.0	0	.002	0	0	0	.003	.001	.001	.001	.004	.004	.002	.004
116.2	0	0	0	0	0	.002	0	0	0	.003	0	0	.001
166.0	0	0	0	0	0	0	0	0	0	.001	0	0	0
500.0	0	0	0	0	0	0	0	0	0	0	0	0	0
$\sum_i (\rho Y V_z A)_i$	.0044	.0050	.0034	.0036	.0036	.0039	.0045	.0047	.0047	.0034	.0043	.0045	.0045
$\sum_i (\rho V_z A)_i$	1.056	1.014	.994	.994	.994	1.063	1.034	1.034	1.034	1.069	1.044	1.044	1.043

Distance from wall, mils	Eddy diffusivity of mass, ft^2/sec			Axial length, z in.	Radial velocity, ft/sec
	E_{d_I}	$E_{d_{II}}$	$E_{d_{III}}$*		V_{r_I}, V_{r_H} and $V_{r_{III}}$*
0	.0006	.0006	.0006	.4	5
5	.022	.010	.005	.8	3
10	.027	.025	.015	1.4	2
15	.033	.030	.018	2.9	2
20	.042	.035	.020	5.9	2
25	.045	.040	.030		
30	.025	.030	.025		
35	.022	.025	.020		
40	.020	.020	.018		
45-500	.015	.015	.018		

*This set corresponds to curves "A", Fig. 15.

Table 9

Comparison of Experimental and Computed Concentration Profiles at Three Downstream Stations
Radial Hydrogen Injection, Mach 2 Air (Fig. 7); Injection Slot = 0.0052 in., $\dot{m}_h$ = 0.010 lb/sec, $\dot{m}_a$ = 1.06 lb/sec

Distance from wall, mils	z = 0.4 in.	z = 1.4 in.				z = 2.9 in.				z = 5.9 in.			
	Initial Profile		Computed				Computed				Computed		
	Y_{exp}	Y_{exp}	Y_I	Y_{II}	Y_{III}	Y_{exp}	Y_I	Y_{II}	Y_{III}	Y_{exp}	Y_I	Y_{II}	Y_{III}
0	.413	.049	.051	.055	.052	.032	.032	.026	.030	.024	.023	.014	.021
7.6	.275	.041	.046	.047	.044	.029	.031	.025	.029	.022	.022	.013	.021
16.1	.186	.036	.044	.044	.042	.025	.031	.024	.029	.021	.022	.013	.021
25.8	.110	.032	.042	.041	.041	.022	.030	.024	.028	.020	.022	.013	.021
36.9	.063	.029	.041	.038	.039	.020	.030	.023	.028	.018	.022	.013	.020
50.1	.028	.024	.037	.030	.036	.017	.029	.020	.027	.017	.021	.012	.020
66.2	.006	.018	.030	.020	.029	.015	.026	.017	.024	.014	.020	.011	.019
87.0	0	.012	.018	.011	.017	.011	.020	.012	.019	.012	.018	.009	.017
116.2	0	.007	.005	.003	.005	.007	.011	.007	.011	.009	.013	.007	.013
166.0	0	.003	0	0	0	.003	.003	.002	.003	.005	.007	.004	.006
215.5	0	.001	0	0	0	.002	0	0	0	.004	.002	.002	.002
500.0	0	0	0	0	0	0	0	0	0	.001	0	0	0
$\Sigma(\rho Y V_z A)_i$	.0084	.0085	.0104	.0086	.0099	.0071	.0100	.0069	.0094	.0080	.0094	.0053	.0088
$\Sigma(\rho V_z A)_i$	1.094	1.147	1.121	1.121	1.121	1.100	1.075	1.076	1.074	1.080	1.050	1.050	1.050

Distance from wall, mils	Eddy diffusivity of mass, ft^2/sec			Axial length, z in.	Radial velocity, ft/sec	
	E_{d_I}	$E_{d_{II}}$	$E_{d_{III}}^*$		V_{r_I} and $V_{r_{III}}^*$	$V_{r_{II}}$
0	.0006	.0006	.0006	.4	40	35
5	.010	.010	.005	.8	25	22
10	.025	.025	.015	1.4	20	15
15	.10	.10	.10	2.9	15	12
20	.20	.20	.20	5.9	12	10
25	.25	.25	.25			
30	.27	.20	.27			
35	.25	.15	.25			
40	.20	.12	.20			
45	.18	.12	.18			
50	.15	.12	.15			
100	.10	.12	.10			
300	.10	.12	.10			
500	.10	.12	.10			

*Note that $E_{d_{III}}$ and $V_{r_{III}}$ correspond to the curves labelled "B" in Fig. 15

Table 10

Comparison of Experimental and Computed Concentration Profiles at Two Downstream Stations

Radial Hydrogen Injection, Mach 2 Air (Fig. 8);
Injection Slot = 0.0052 in., $\dot{m}_h$ = 0.015 lb/sec, $\dot{m}_a$ = 1.05 lb/sec

Distance from wall, mils	Y_{exp} @ z = 0.4 in.	Y @ z = 2.9 in.		Y @ z = 5.9 in.	
	Initial Profile	Exp.	Computed*	Exp.	Computed*
0	.129	.036	.032	.026	.026
7.6	.103	.031	.031	.024	.026
16.1	.072	.026	.030	.023	.025
25.8	.058	.024	.029	.022	.025
36.9	.043	.023	.029	.021	.025
50.1	.024	.022	.028	.019	.025
66.2	.012	.019	.027	.018	.024
87.0	.005	.016	.024	.017	.022
116.2	.002	.013	.017	.015	.019
166.0	0	.008	.009	.013	.013
215.5	0	.005	.004	.011	.009
500.0	0	0	0	.005	.002
$\sum_i (\rho Y V_z A)_i$	.0090	.0116	.0133	.0148	.0151
$\sum_i (\rho V_z A)_i$	1.123	1.095	1.066	1.077	1.047

*Computed using Curves "C" of Fig. 15.

Table 11

Comparison of Experimental and Computed Concentration Profiles at Three Downstream Stations
Radial Hydrogen Injection, Mach 3 Air (Fig. 9); Injection Slot = 0.0052 in., $\dot{m}_h$ = 0.010 lb/sec, $\dot{m}_a$ = 1.99 lb/sec

Distance from wall, mils	z = 1.65 in.	z = 2.9 in.				z = 4.9 in.				z = 5.9 in.			
	Initial Profile	Computed				Computed				Computed			
	Y_{exp}	Y_{exp}	Y_I	Y_{II}	Y_{III}	Y_{exp}	Y_I	Y_{II}	Y_{III}	Y_{exp}	Y_I	Y_{II}	Y_{III}
0	.084	.053	.048	.057	.052	.034	.032	.046	.037	.032	.027	.043	.033
7.6	.075	.051	.046	.055	.050	.030	.031	.046	.036	.031	.027	.043	.032
16.1	.063	.046	.043	.053	.047	.026	.030	.045	.035	.029	.026	.042	.031
25.8	.054	.039	.040	.049	.043	.022	.028	.043	.033	.028	.025	.041	.030
36.9	.040	.032	.034	.042	.038	.017	.026	.040	.031	.024	.023	.039	.028
50.1	.026	.023	.023	.030	.027	.011	.020	.032	.025	.019	.018	.032	.023
66.2	.012	.015	.011	.015	.015	.007	.012	.019	.016	.014	.012	.020	.016
87.0	.003	.007	.004	.004	.005	.004	.006	.006	.008	.008	.006	.007	.009
116.2	0	.001	.001	0	.001	.002	.001	.001	.002	.003	.002	.001	.003
166-500	0	0	0	0	0	0	0	0	0	0	0	0	0
$\sum_i(\rho Y V_z A)_i$	.0088	.0076	.0066	.0080	.0076	.0050	.0067	.0096	.0085	.0072	.0062	.0093	.0079
$\sum_i(\rho V_z A)_i$	2.110	1.972	1.915	1.915	1.915	1.958	1.902	1.902	1.902	1.980	1.913	1.913	1.913

Distance from wall, mils	Eddy Diffusivity of mass, ft^2/sec		Axial length, z, in.	Radial velocity, ft/sec	
	E_{d_I} and $E_{d_{III}}$*	$E_{d_{II}}$		V_{r_I}	$V_{r_{II}}$ and $V_{r_{III}}$*
0	.0006	.0006			
5	.020	.020			
10	.030	.027	1.4	--	3
15	.040	.033	1.65	10	--
20	.050	.042	2.9	8	2
25	.060	.045	4.9	3	2
30	.070	.025	5.9	2	2
35	.050	.022			
40	.030	.020			
45	.030	.013			
50-500	.030	.010			

*Note that $E_{d_{III}}$ and $V_{r_{III}}$ correspond to curves labelled "D" in Fig. 15.

Table 12

Comparison of Experimental and Computed Velocity and Concentration Profiles at Two Downstream Stations
Radial Hydrogen Injection, Mach 3 Air (Fig. 9); Injection Slot = 0.0052 in., $\dot{m}_h$ = 0.010 lb/sec, $\dot{m}_a$ = 1.99 lb/sec

Distance from wall, x, mils	z = 1.65 in. (V_r = 3fps) Initial Profile		z = 2.9 in. (V_r = 2fps) Experimental		z = 2.9 in. (V_r = 2fps) Computed		z = 5.9 in. (V_r = 2fps) Experimental		z = 5.9 in. (V_r = 2fps) Computed		Transport Coefficients	
	Y_{exp}	$V_{z_{exp}}$ ft/sec	Y_{exp}	$V_{z_{exp}}$ ft/sec	Y	V_z ft/sec	Y_{exp}	$V_{z_{exp}}$ ft/sec	Y	V_z ft/sec	x, mils	$E_d = E_m$ ft²/sec
0	.084	0*	.053	1117*	.054	0*	.032	1043*	.032	0*	0	.0006
7.6	.075	1450	.051	1313	.053	1122	.031	1237	.032	937	5	.008
16.1	.063	1511	.046	1394	.048	1372	.029	1315	.030	1171	10	.017
25.8	.054	1581	.040	1461	.043	1491	.028	1405	.029	1306	15	.023
36.9	.040	1638	.032	1509	.036	1574	.024	1470	.026	1417	20	.030
50.1	.026	1668	.023	1591	.025	1660	.019	1533	.021	1553	25	.035
66.2	.012	1735	.014	1652	.014	1747	.014	1650	.014	1680	30	.040
87.0	.003	1869	.008	1768	.005	1834	.008	1738	.008	1777	35	.035
116.2	0	1908	.002	1864	.001	1890	.003	1798	.002	1843	40	.030
166.0	0	1910	0	1921	0	1901	0	1882	0	1877	45-500	.025
215.5	0	1925	0	1927	0	1914	0	1900	0	1890	z, in.	V_r, ft/sec
500.0	0	1904	0	1840	0	1890	0	1881	0	1869		
$\sum_i(\rho Y V_z A)_i$	.0088		.0076		.0074		.0072		.0071		1.4	3
$\sum_i(\rho V_z A)_i$	2.110		1.972		1.968		1.980		2.076		2.9	2
$\sum_i(\rho V_z^2 A)_i/g_c$	123.6		114.7		117.6		112.4		121.6		5.9	2

*The velocity at the wall was set to zero for the initial profile because of the boundary condition; experimental values were never zero because of the finite probe size.

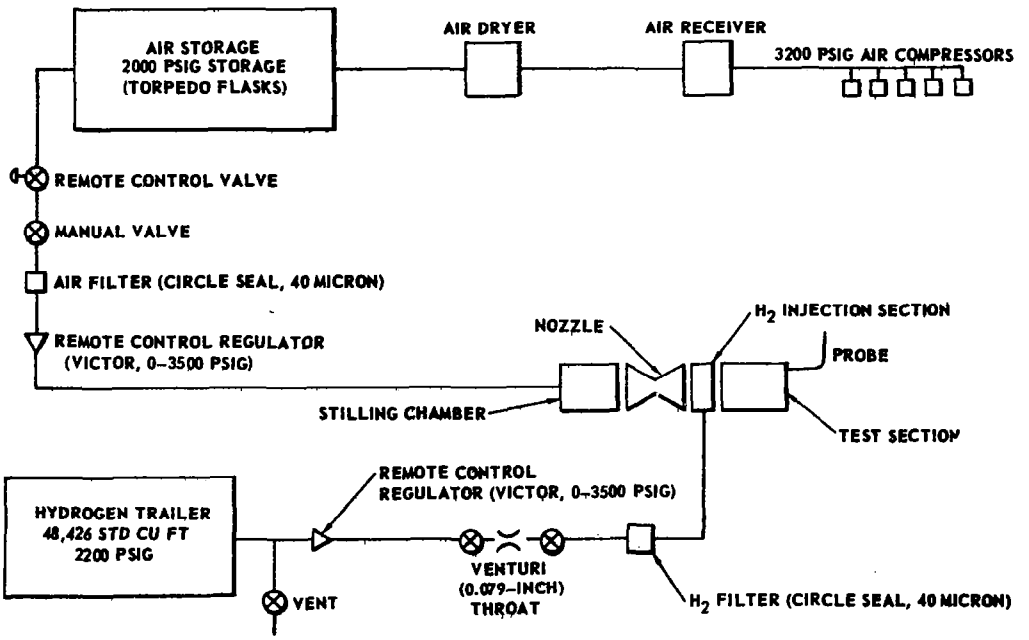

Fig. 1 SCHEMATIC DIAGRAM OF APPARATUS

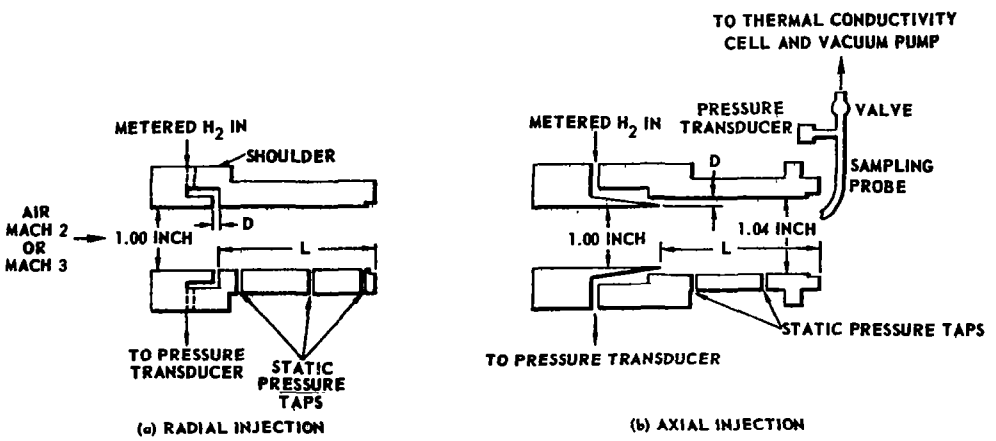

Fig. 2 DETAILS OF TEST SECTIONS.

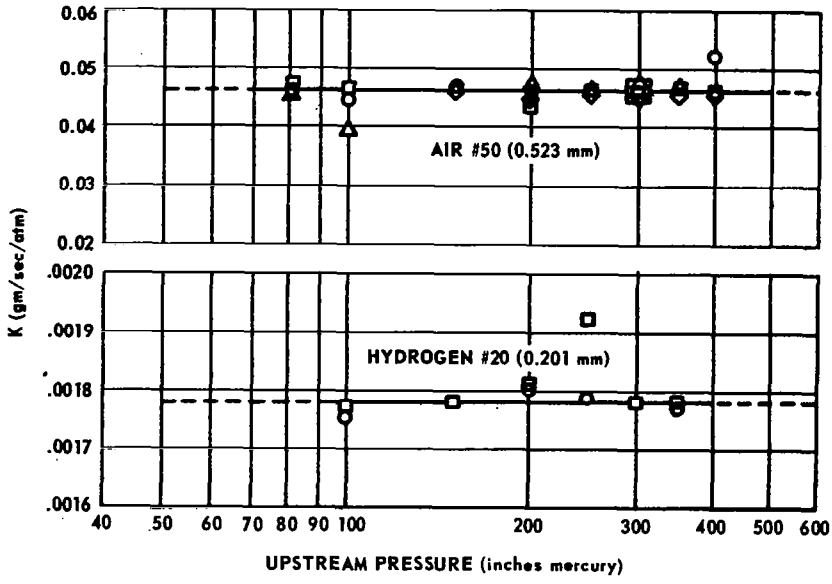

Fig. 3 JEWELLED ORIFICE CALIBRATIONS.

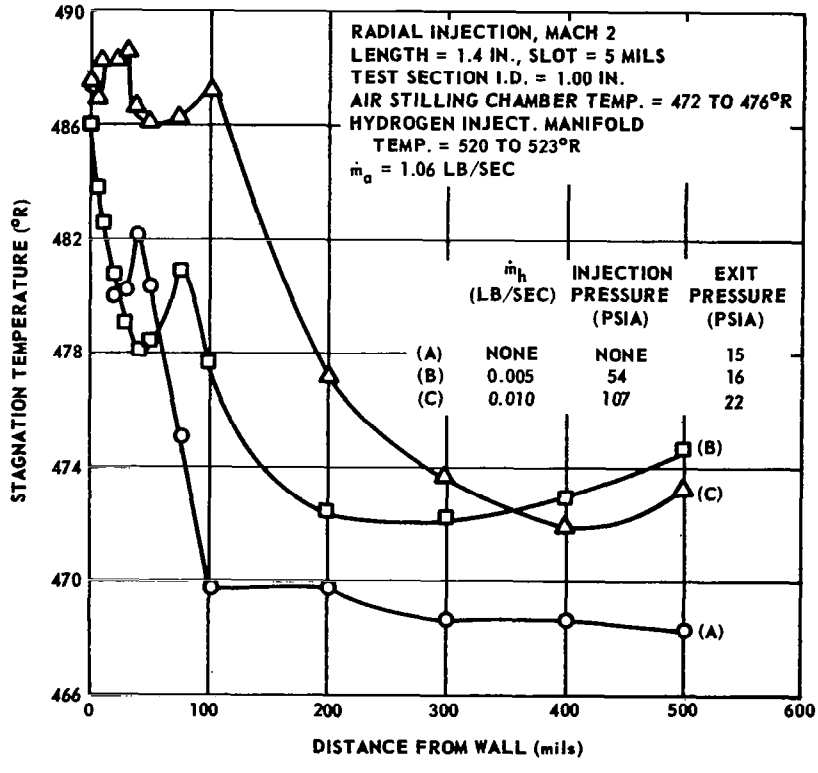

Fig. 4 STAGNATION TEMPERATURE PROFILES, MACH 2 AIR.

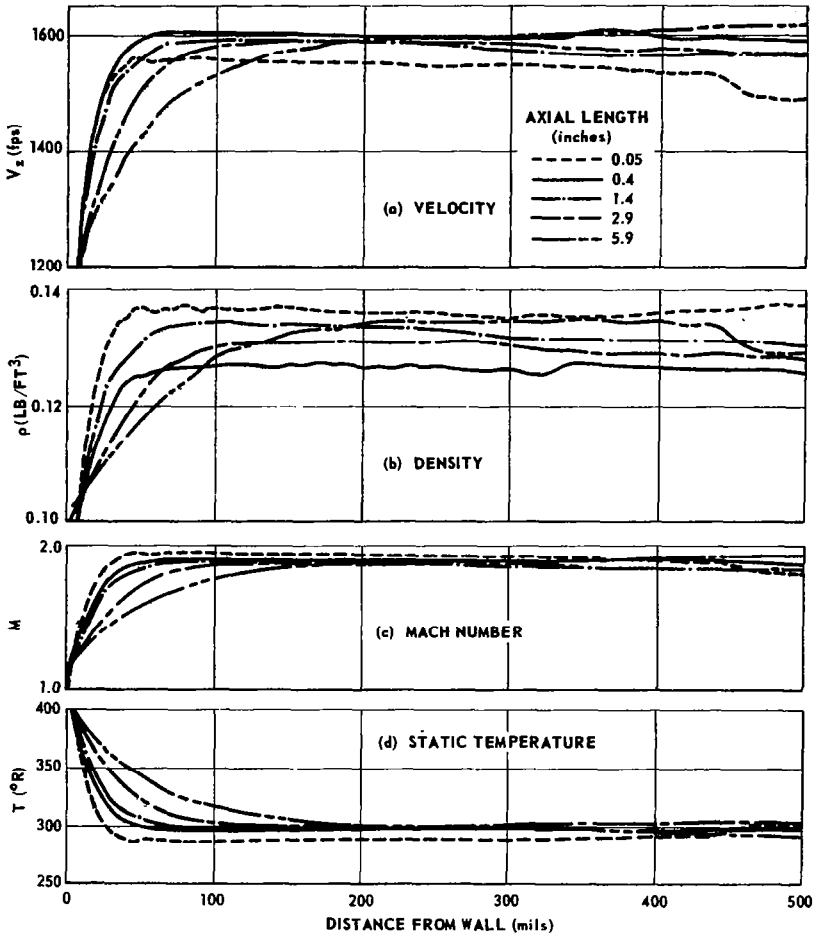

Fig. 5 AIR PROFILES FOR V_z, ρ, M, AND T, MACH 2 AIR (NO HYDROGEN), 1.06 LB/SEC, EXIT PRESSURE = 13.6 TO 14.9 PSIA.

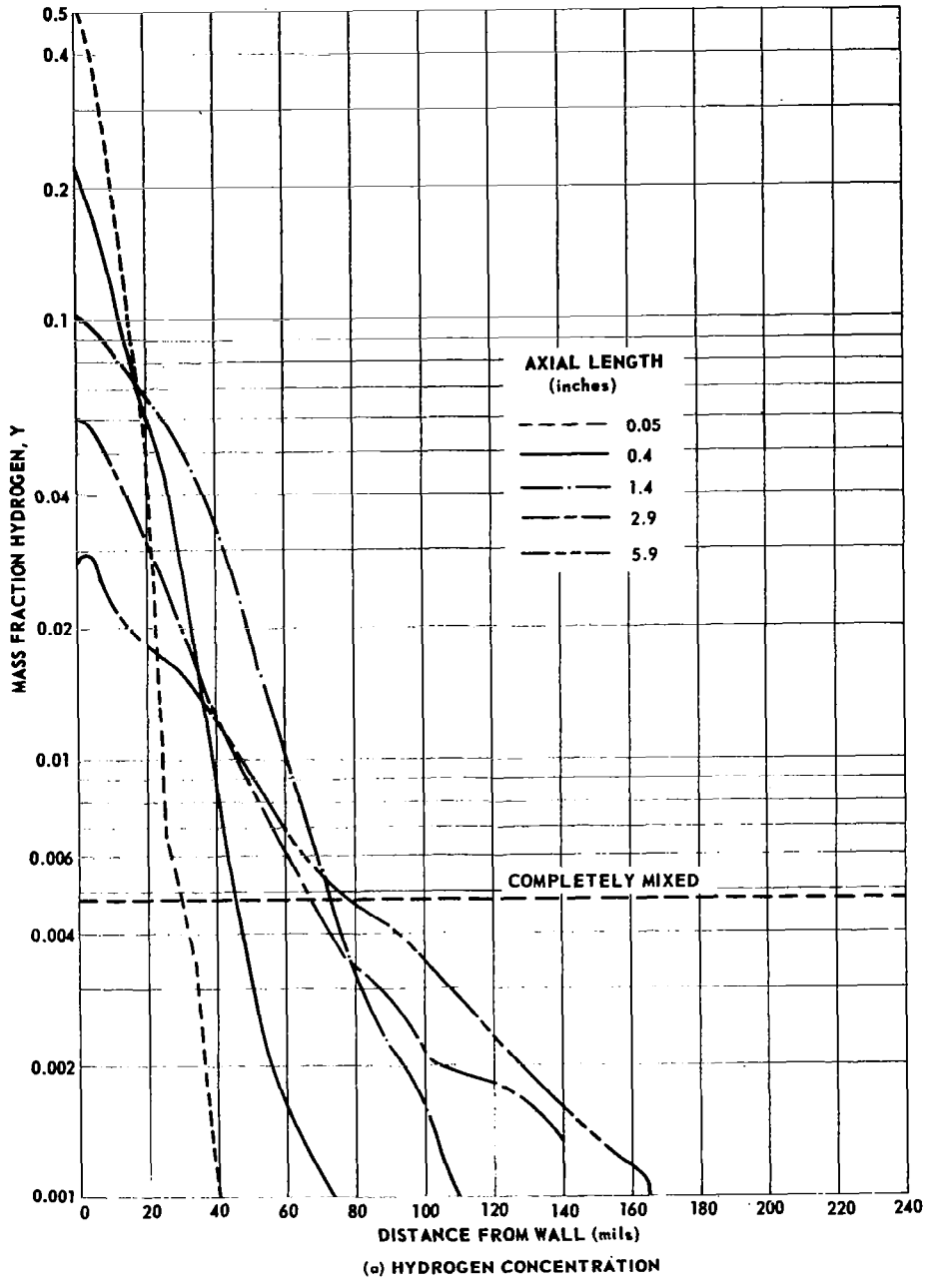

Fig. 6 MIXTURE PROFILES FOR RADIAL HYDROGEN INJECTION AT 0.005 LB/SEC, AND INTO MACH 2 AIR AT 1.06 LB/SEC; 5-MIL SLOT; INJECTION PRESSURE 63 TO 65 PSIA; EXIT PRESSURE 15.2 TO 19.3 PSIA.

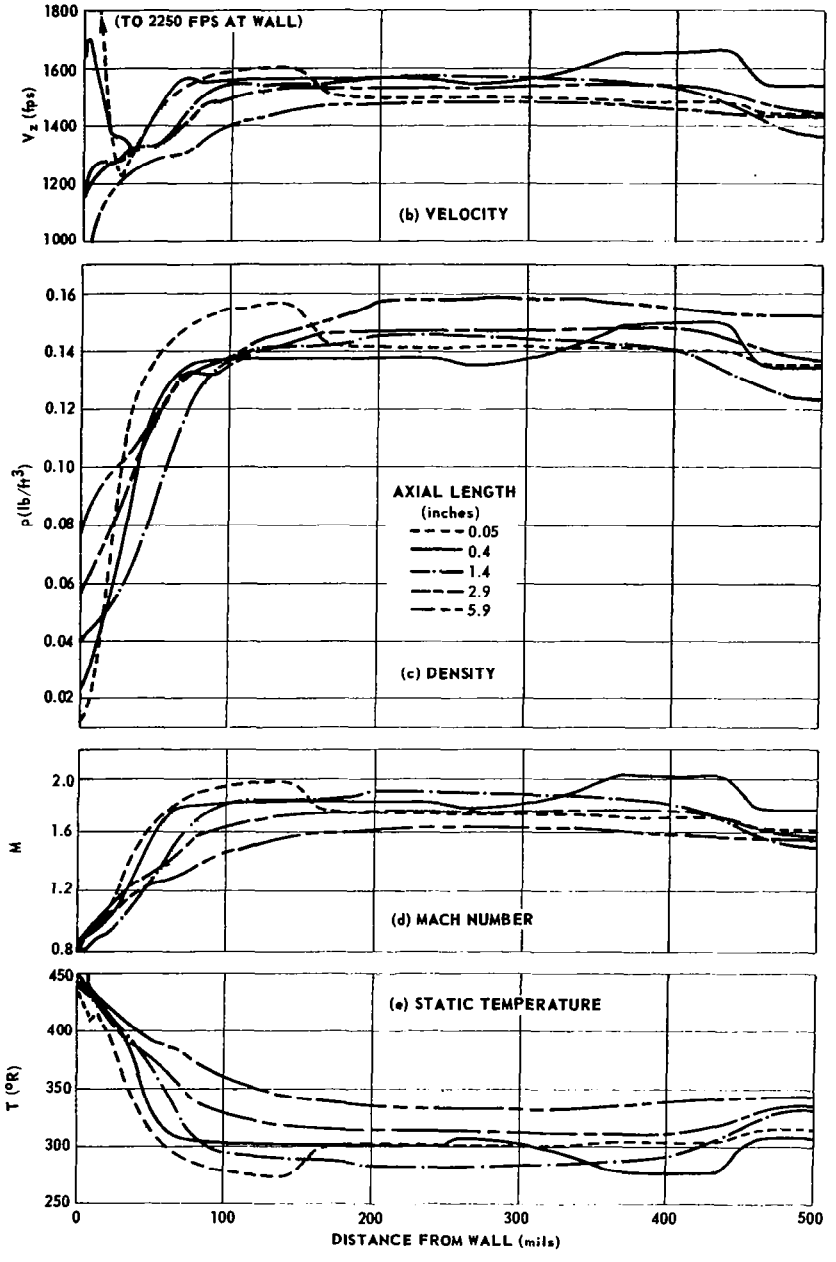

Fig. 6 CONCLUDED

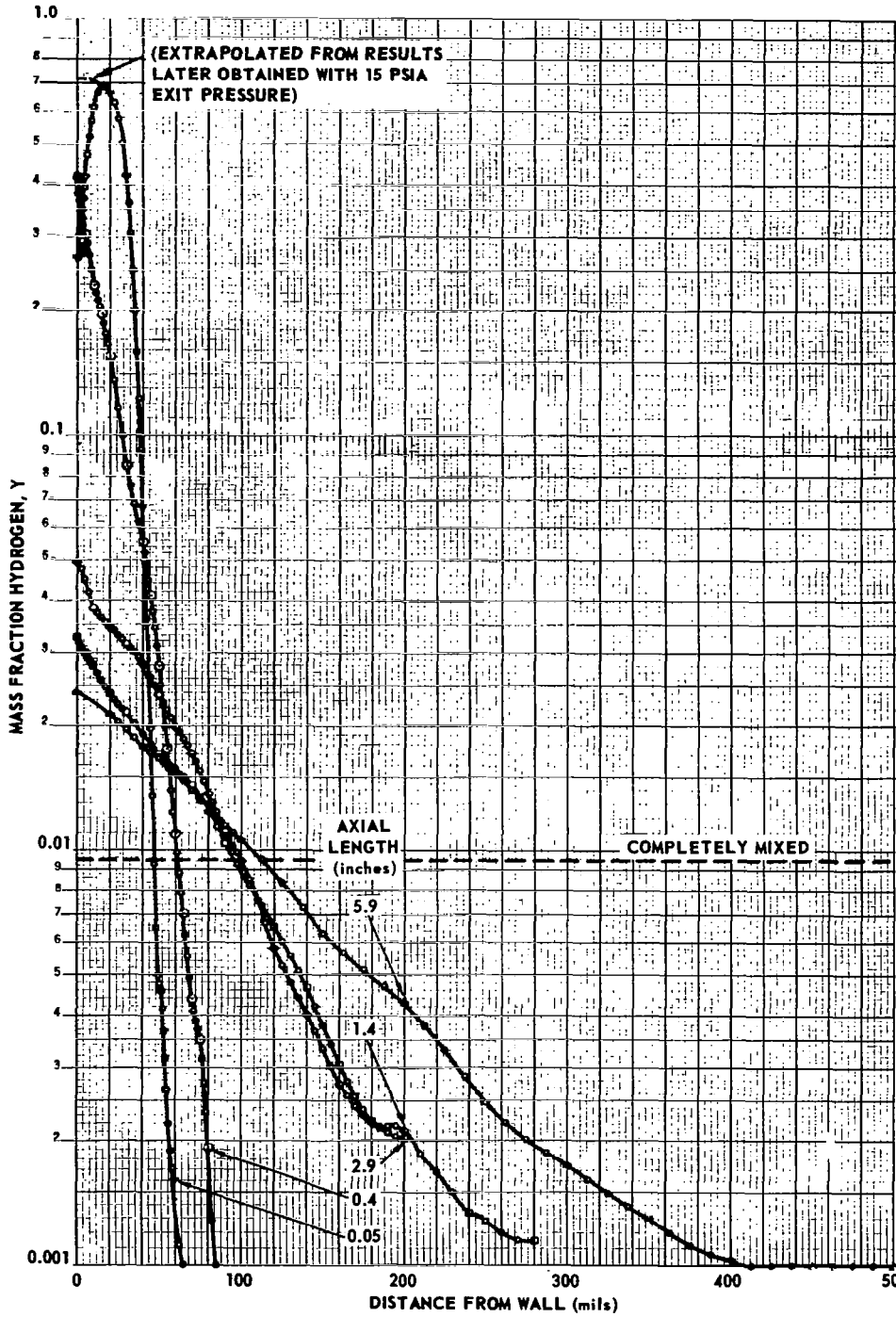

(a) HYDROGEN CONCENTRATION

Fig. 7 MIXTURE PROFILES, RADIAL HYDROGEN INJECTION AT 0.010 LB/SEC INTO MACH 2 AIR AT 1.06 LB/SEC; 5-MIL SLOT; INJECTION PRESSURE = 116 TO 128 PSIA; EXIT PRESSURE 23.1 TO 26.0 PSIA; EXCEPT AT L = 0.05 IN., WHERE IT WAS 11.3 PSIA

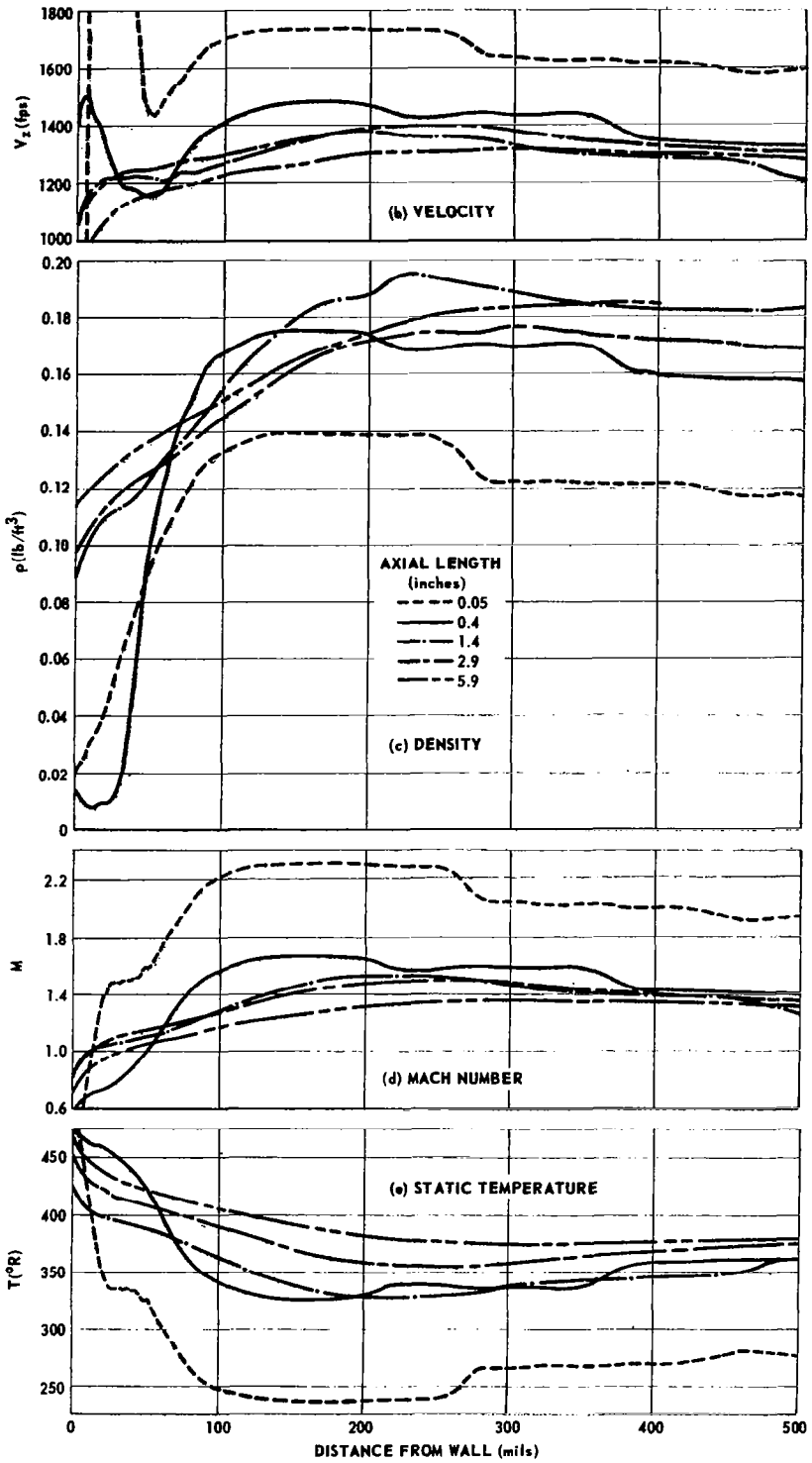

Fig. 7 CONCLUDED

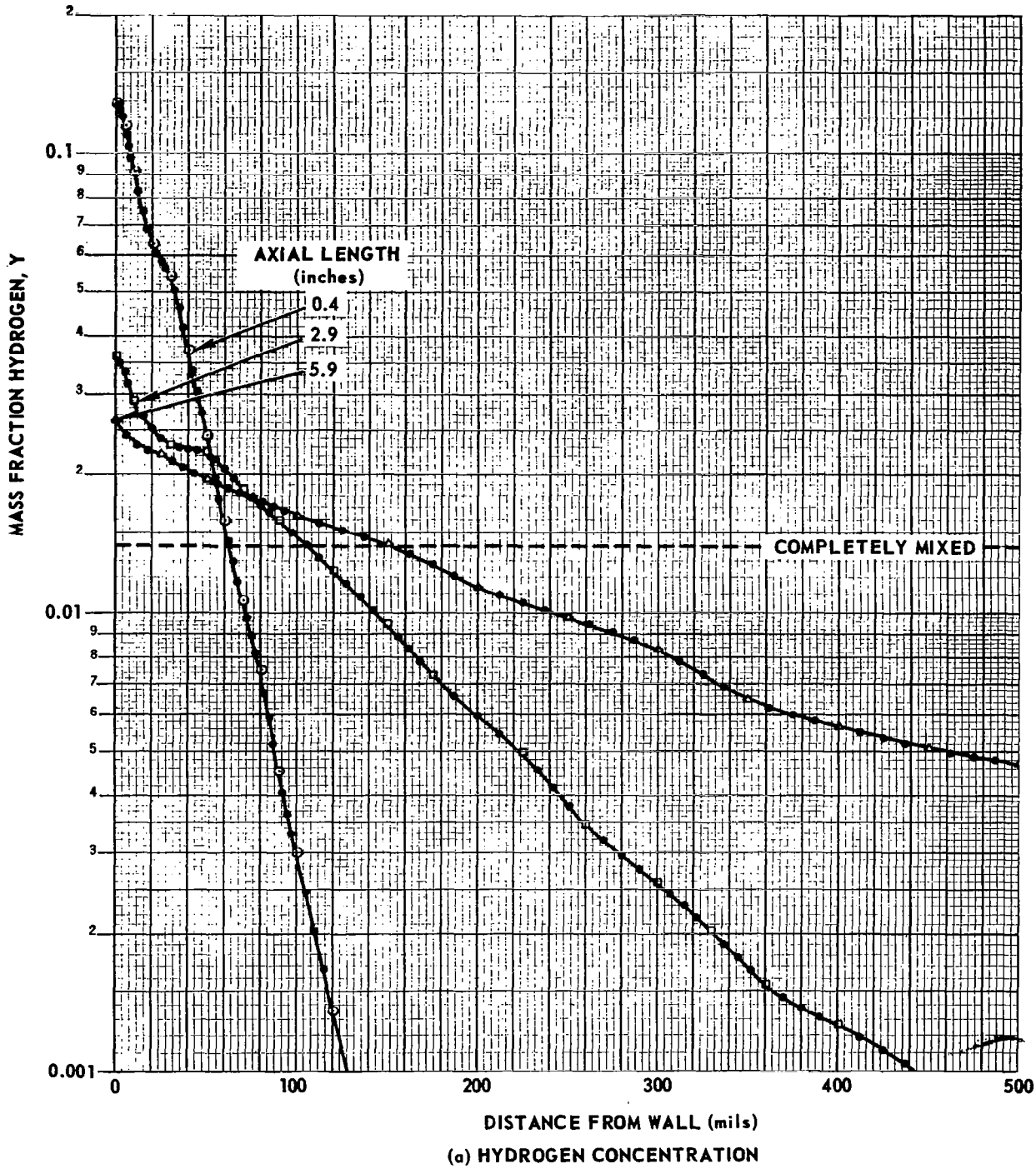

Fig. 8 MIXTURE PROFILES, RADIAL HYDROGEN INJECTION, AT 0.015 LB/SEC INTO MACH 2 AIR AT 1.05 LB/SEC; 5–MIL SLOT; INJECTION PRESSURE 179 TO 189 PSIA; EXIT PRESSURE 27.9 TO 33.8 PSIA.

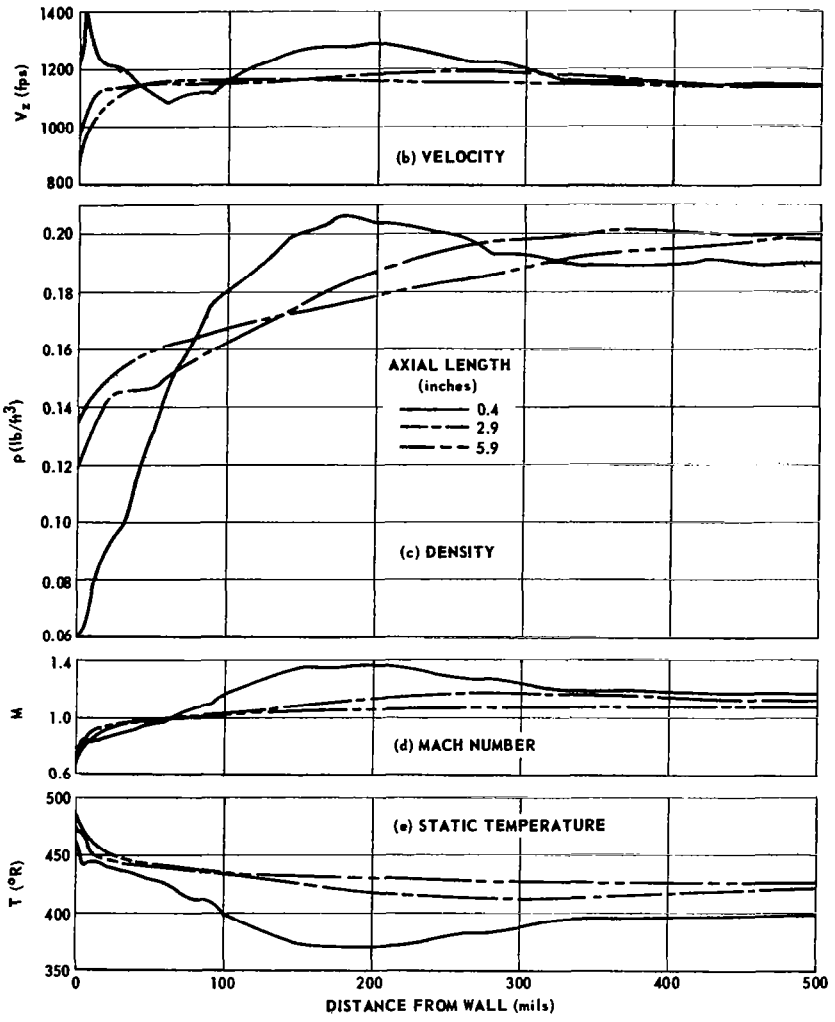

Fig. 8 CONCLUDED

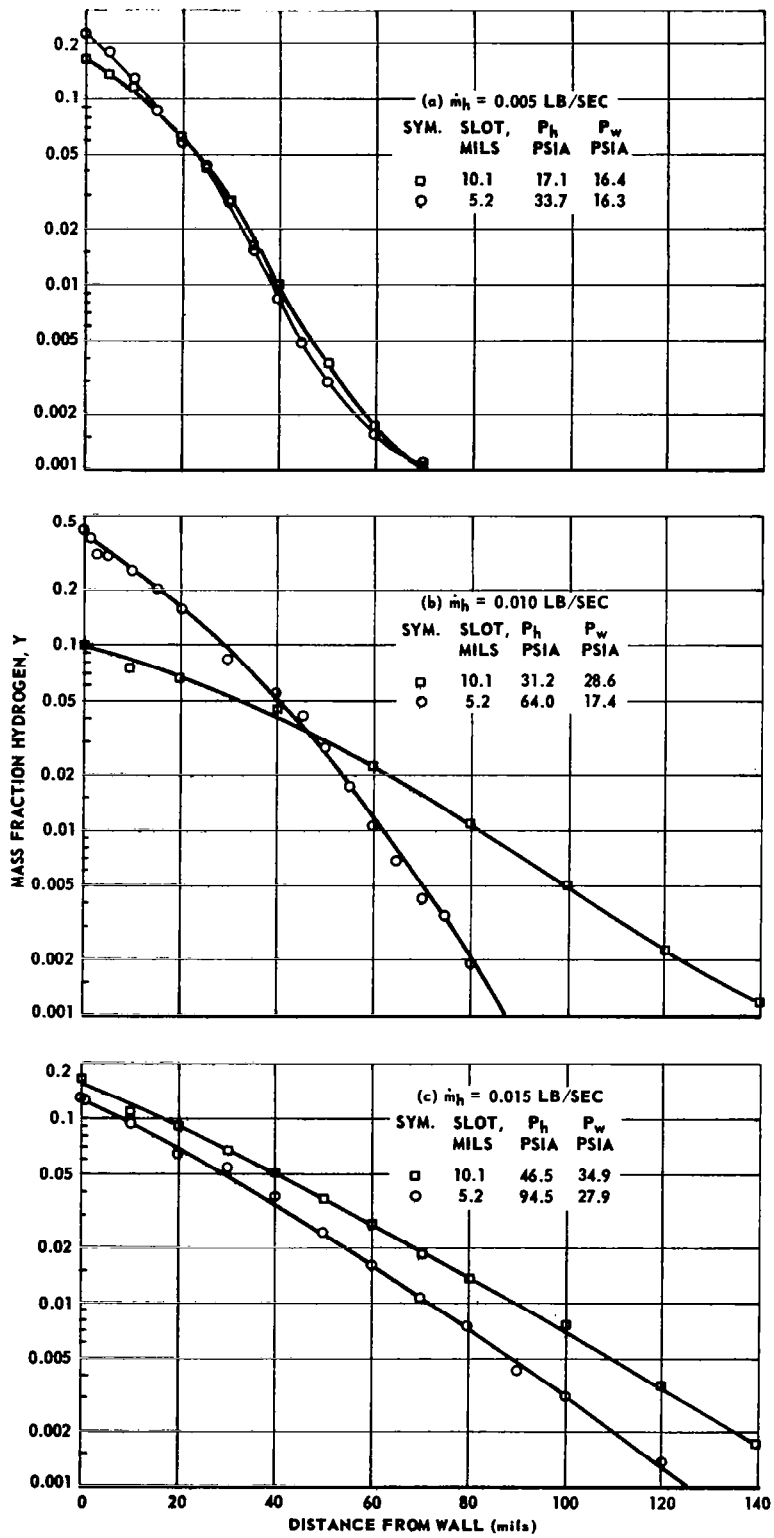

Fig. 9 EFFECT OF SLOT WIDTH ON HYDROGEN CONCENTRATION PROFILES, RADIAL INJECTION, MACH 2 AIR
P_h ≃ STATIC PRESSURE OF H_2 IN SLOT (M 1)
P_w = TEST SECTION WALL PRESSURE NEAR SLOT
L = 0.4 IN. FOR PARTS (a) THROUGH (c)

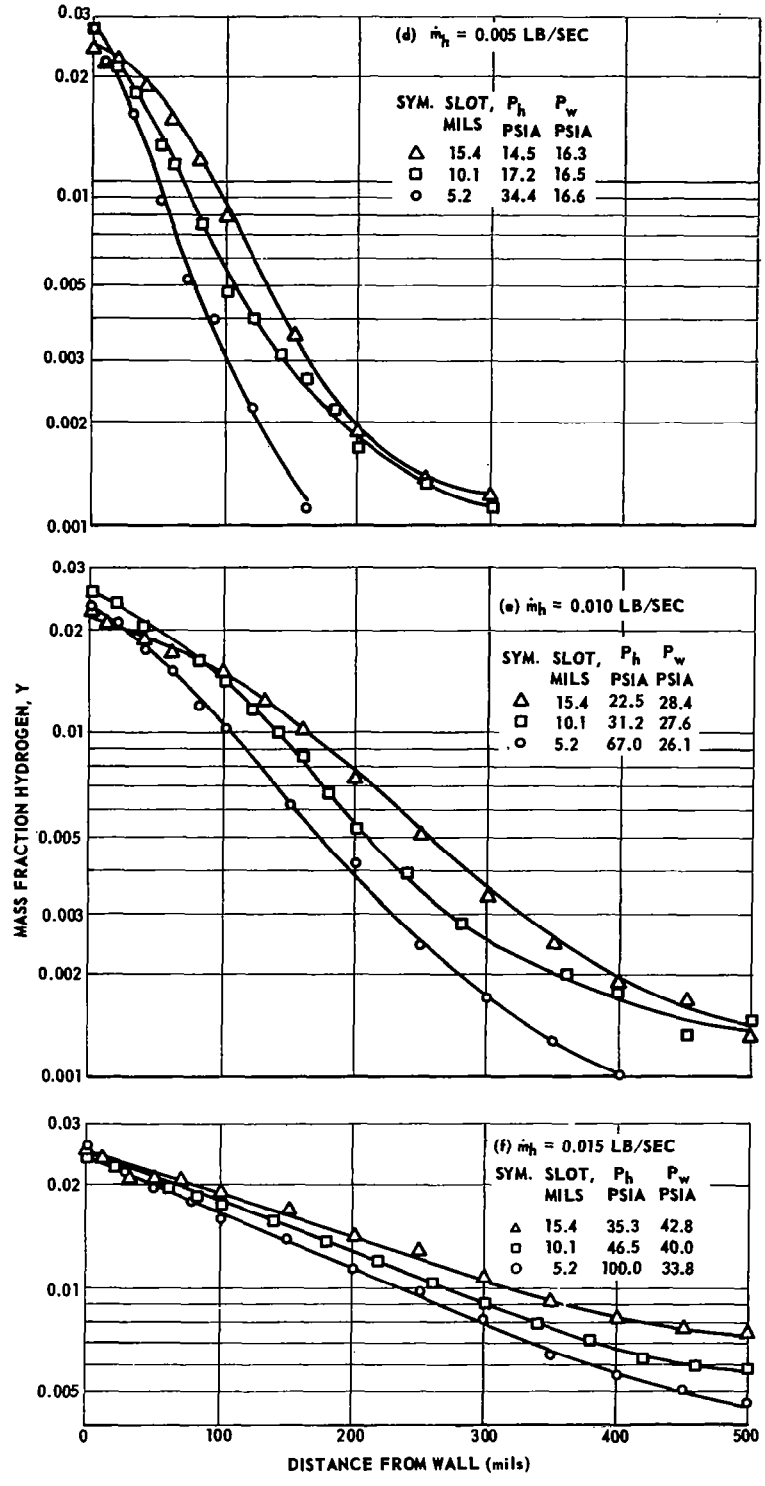

Fig. 9 CONCLUDED
L = 5.9 IN. FOR PARTS (d) THROUGH (f).
NOTE ALSO THAT SCALES ARE DIFFERENT FROM PARTS (a) THROUGH (c)

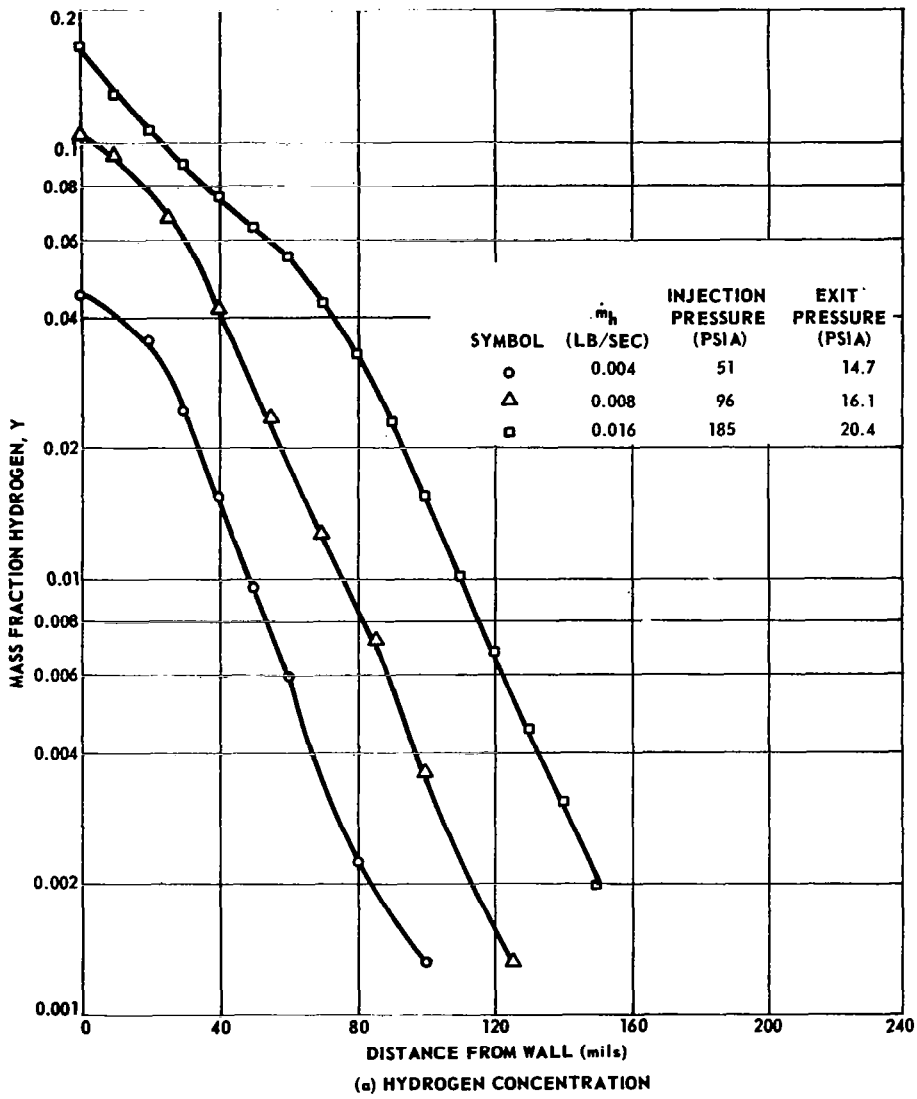

(a) HYDROGEN CONCENTRATION

Fig. 10 MIXTURE PROFILES, AXIAL HYDROGEN INJECTION AT 3 FLOW RATES INTO MACH 2 AIR AT 1.10 LB/SEC; 5-MIL SLOT; 3.4-IN.-LONG TEST SECTION.

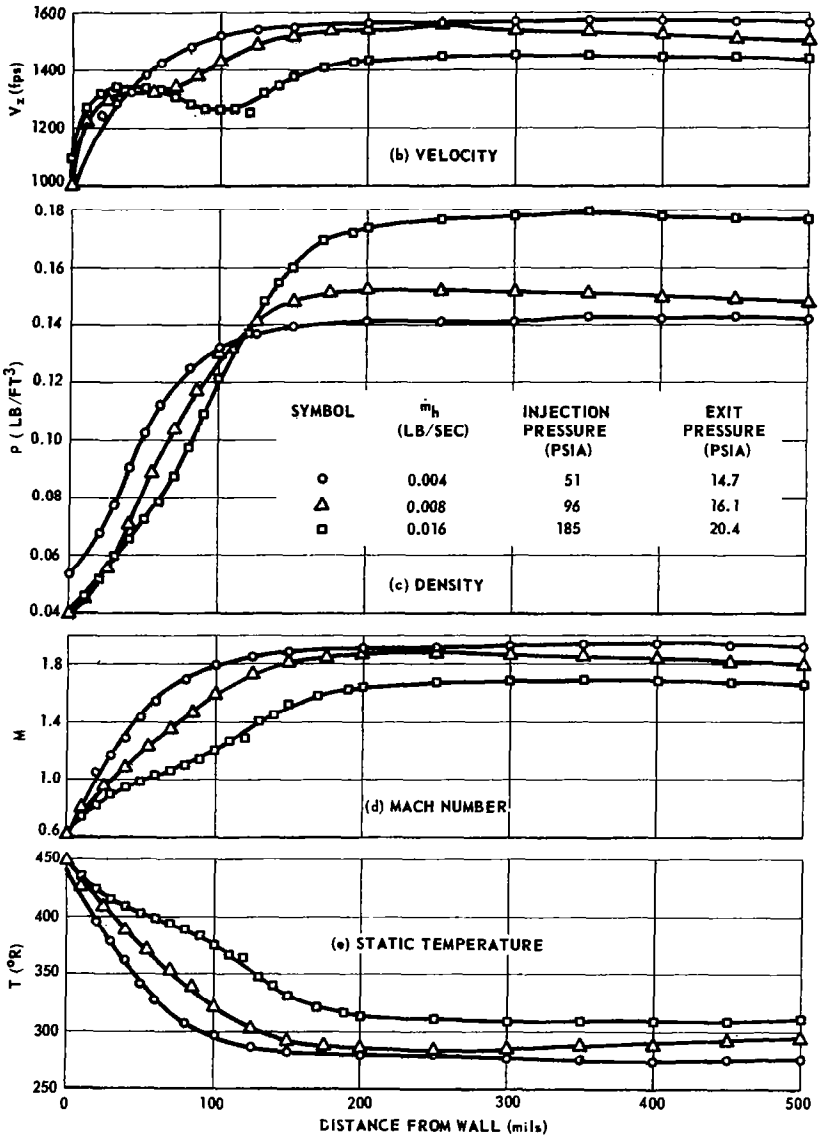

Fig. 10 CONCLUDED

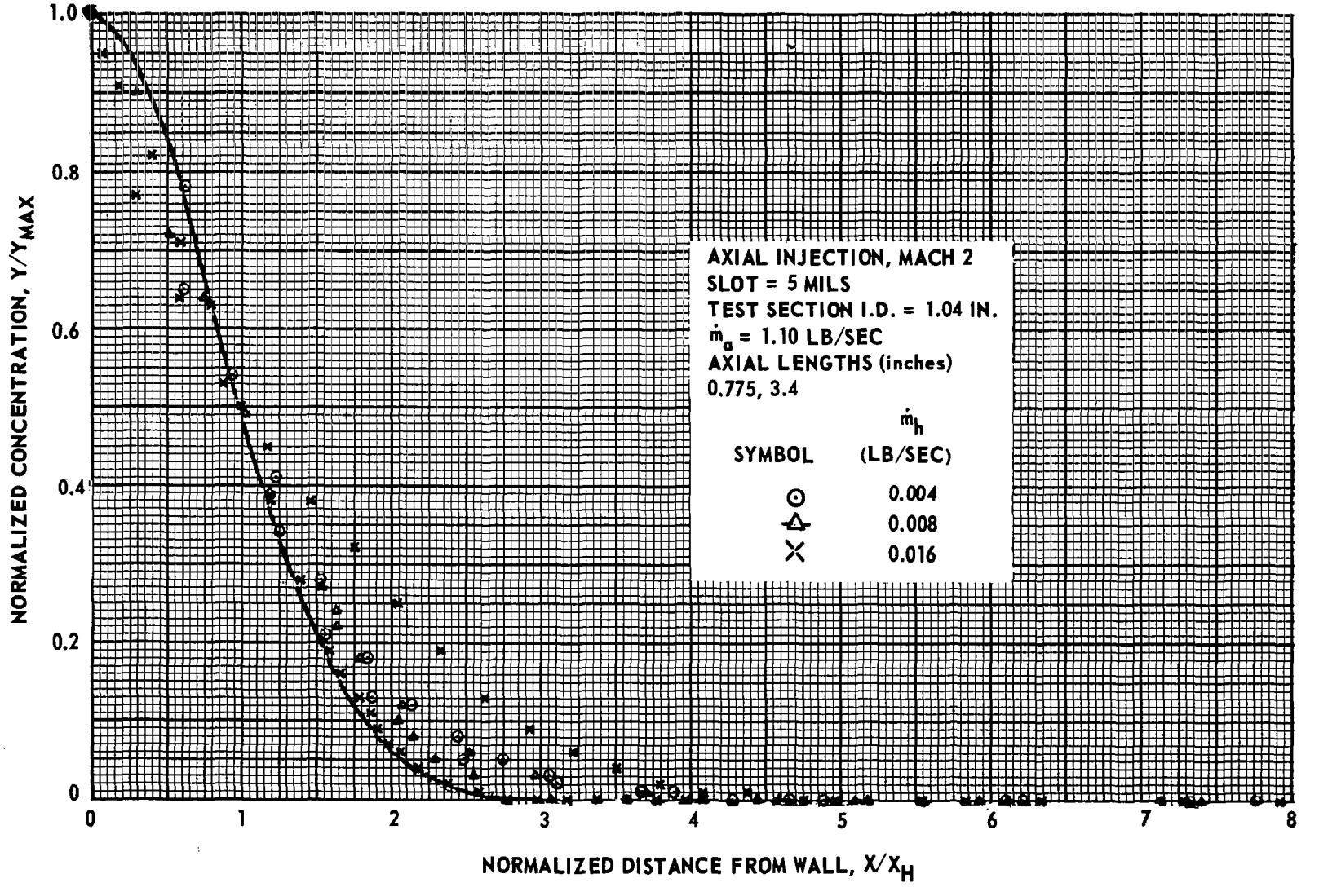

Fig. 11 NORMALIZED CONCENTRATION PROFILE, AXIAL HYDROGEN INJECTION, MACH 2 AIR.

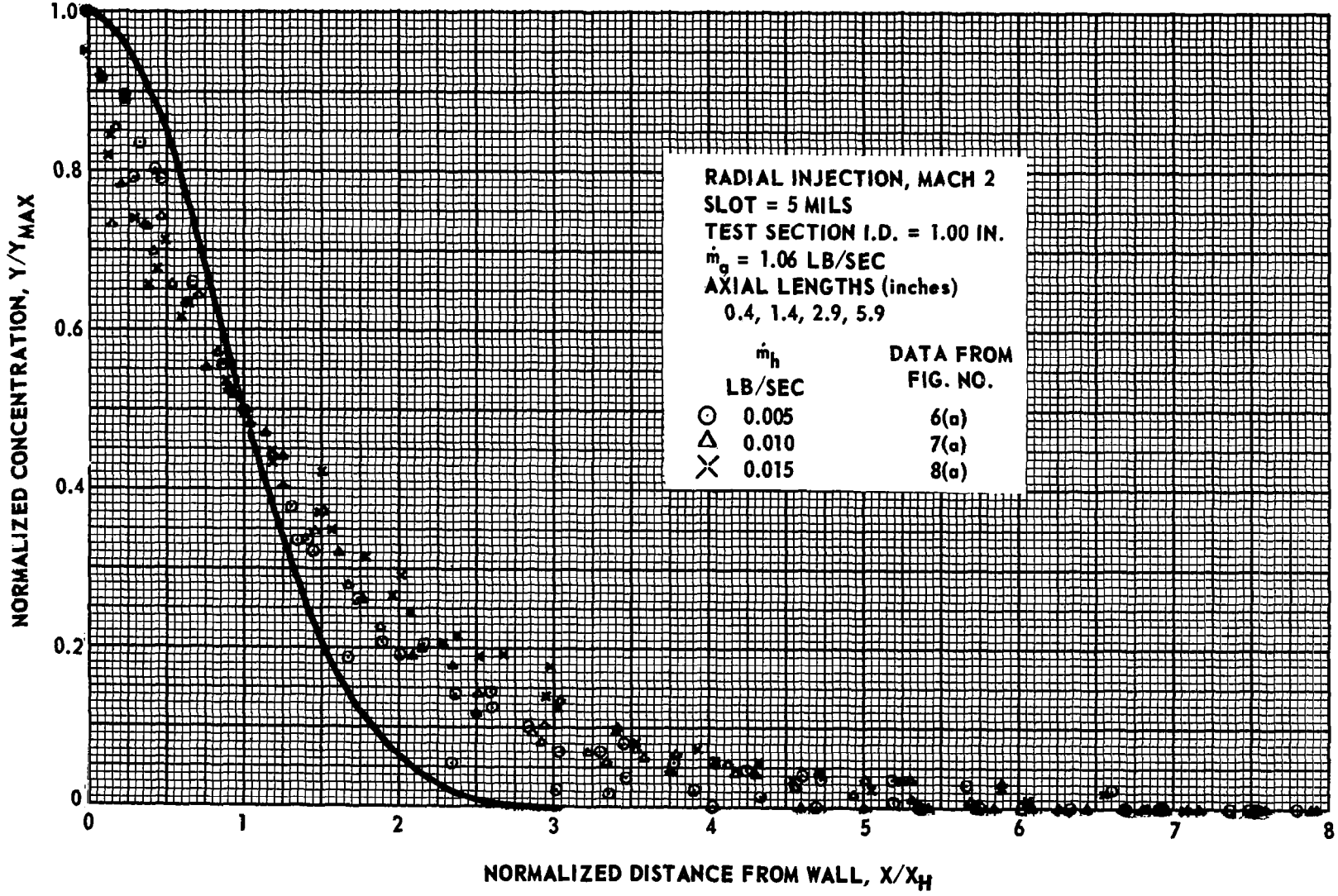

Fig. 12 NORMALIZED CONCENTRATION PROFILE, RADIAL HYDROGEN INJECTION, MACH 2 AIR.

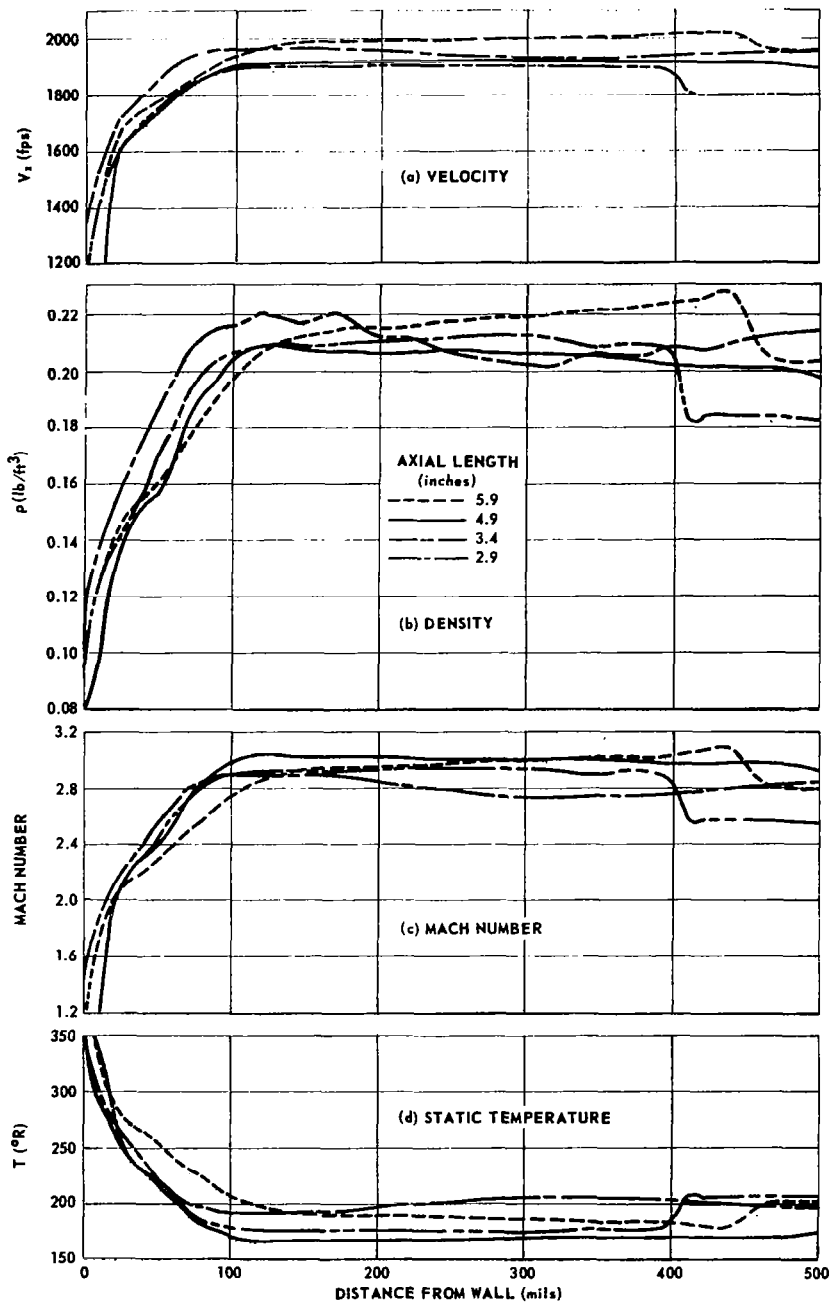

Fig. 13 AIR PROFILES (NO HYDROGEN), MACH 3, 1.97 LB/SEC; EXIT PRESSURE 12.8 TO 15.6 PSIA.

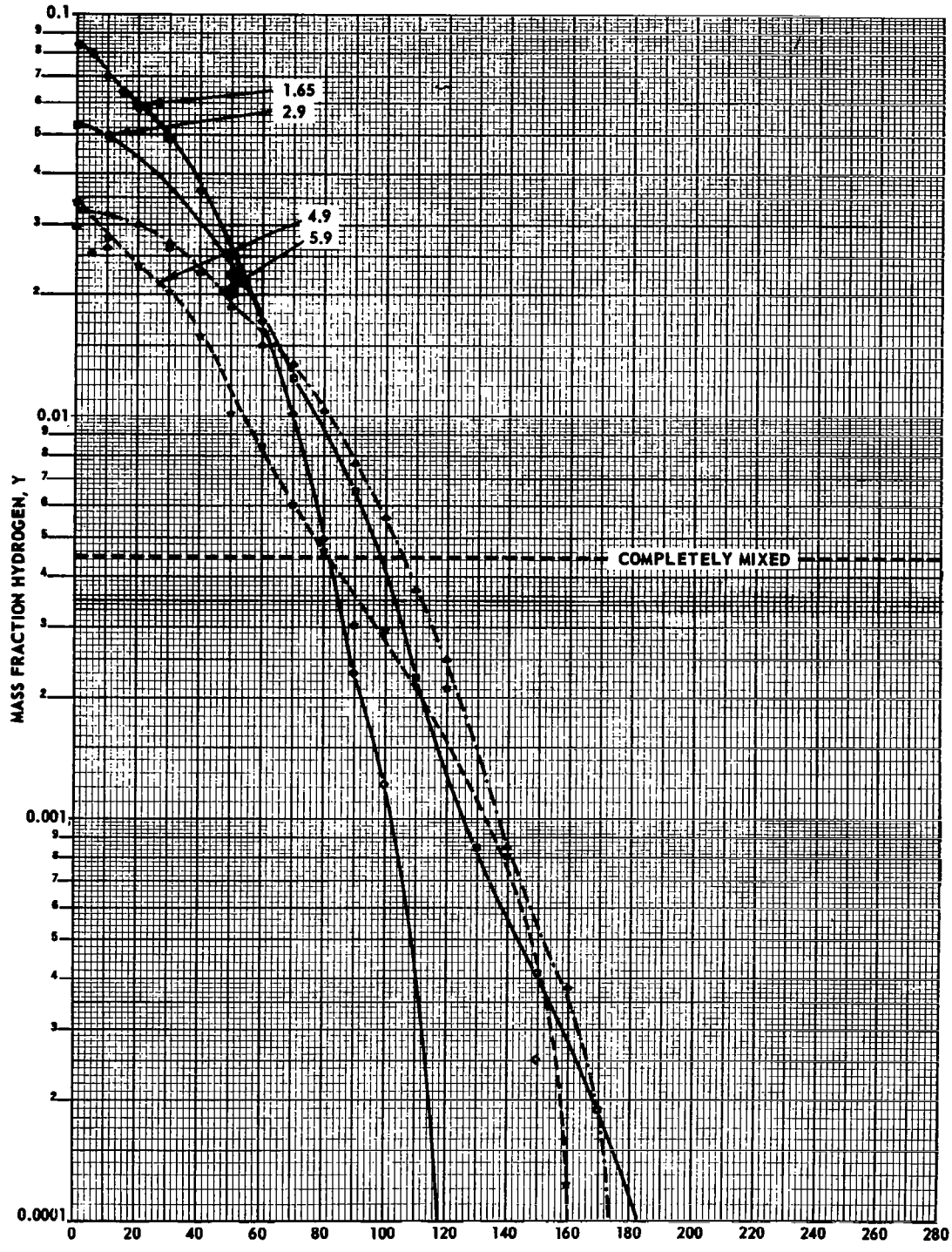

(a) HYDROGEN CONCENTRATION

Fig. 14 MIXTURE PROFILES, RADIAL HYDROGEN INJECTION AT 0.010 LB/SEC INTO MACH 3 AIR AT 1.99 LB/SEC; 5-MIL SLOT; INJECTION PRESSURE 104 TO 138 PSIA; EXIT PRESSURE 16.1 TO 19.6 PSIA.

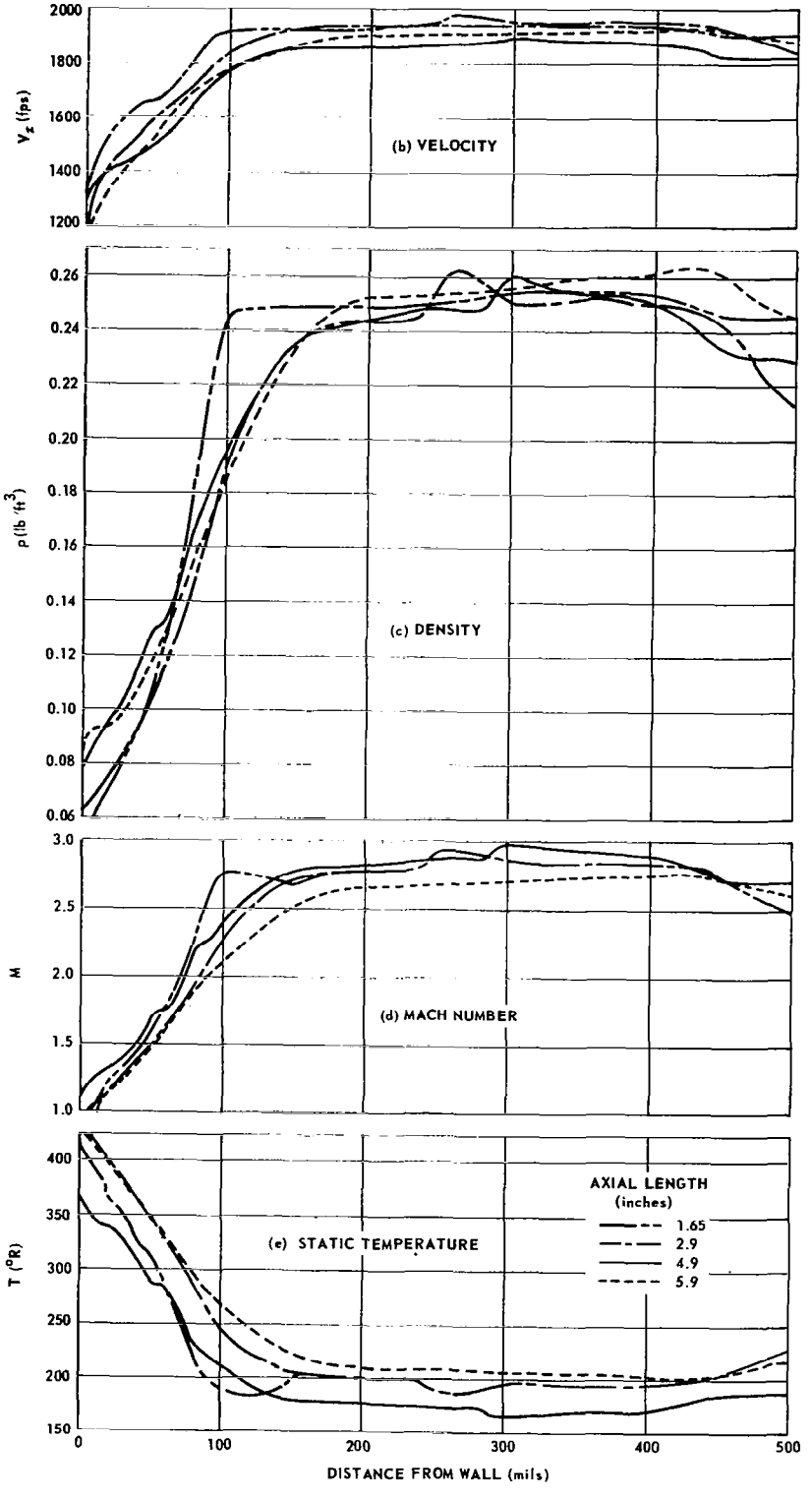

Fig. 14 CONCLUDED

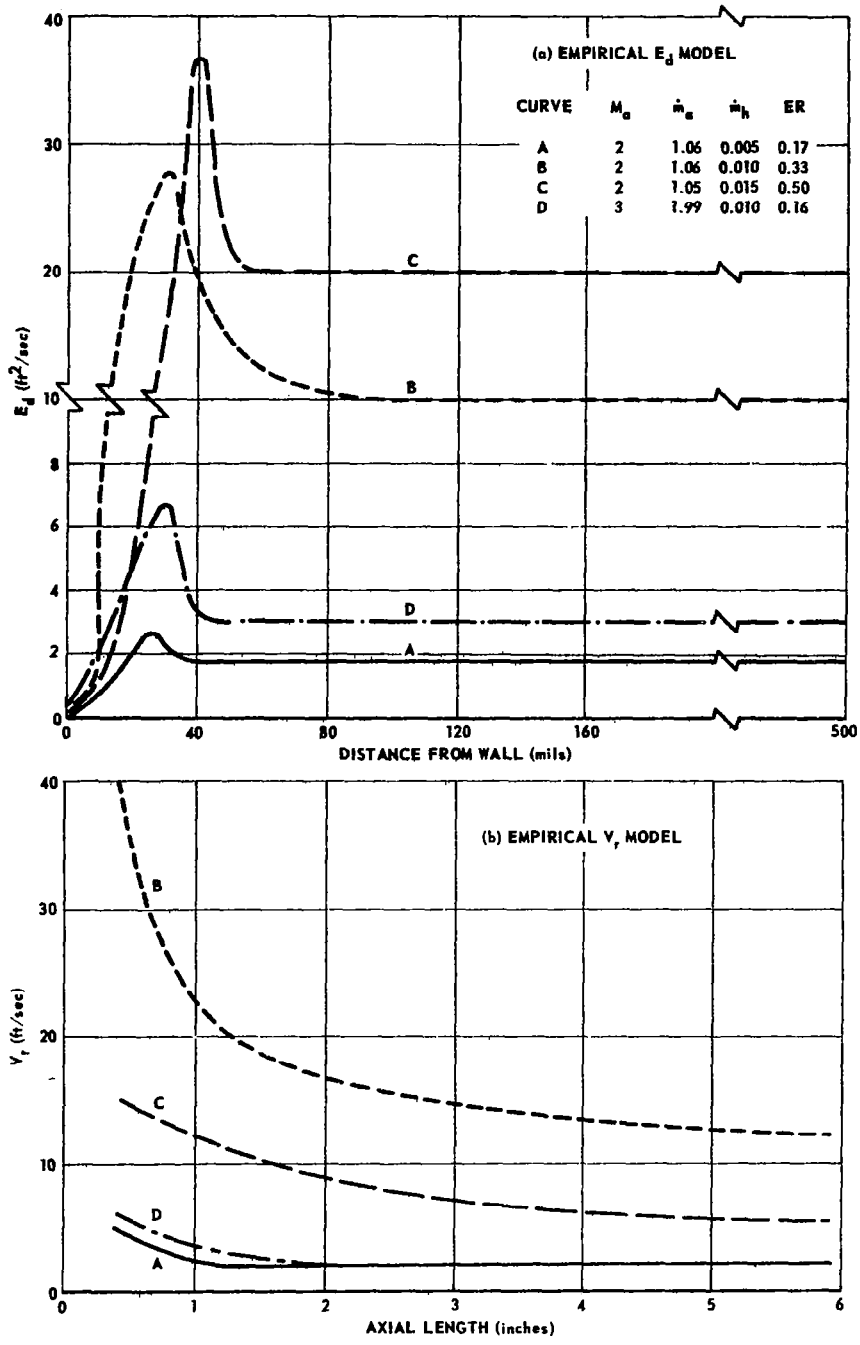

Fig. 15 EMPIRICAL MODELS FOR (a) EDDY DIFFUSIVITY OF MASS AND (b) RADIAL VELOCITY.

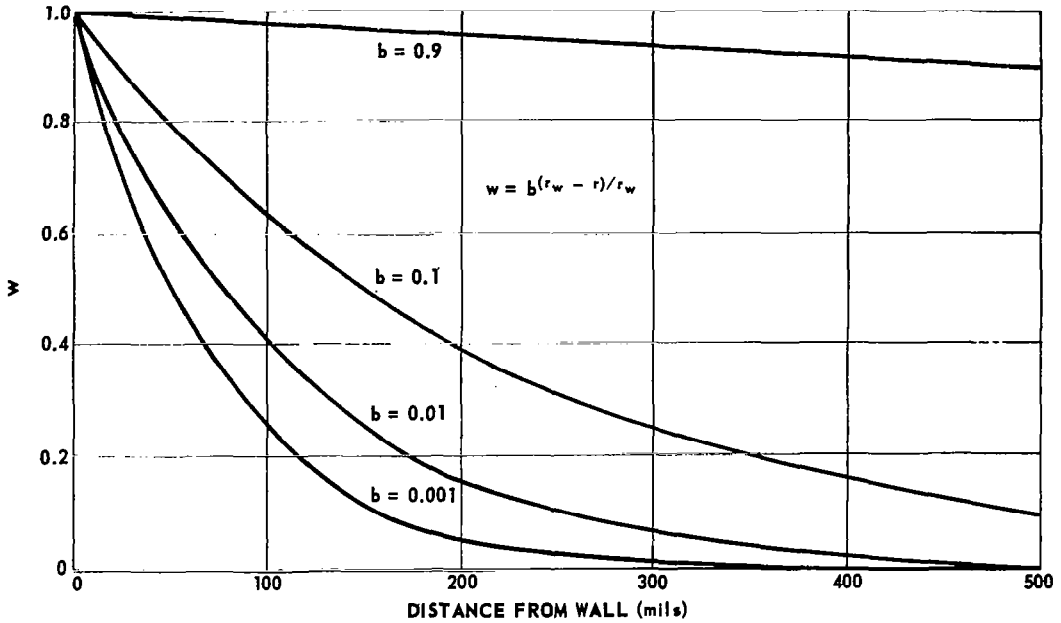

Fig. C–2 EFFECT OF CHANGING b ON RADIAL GRID SPACING.

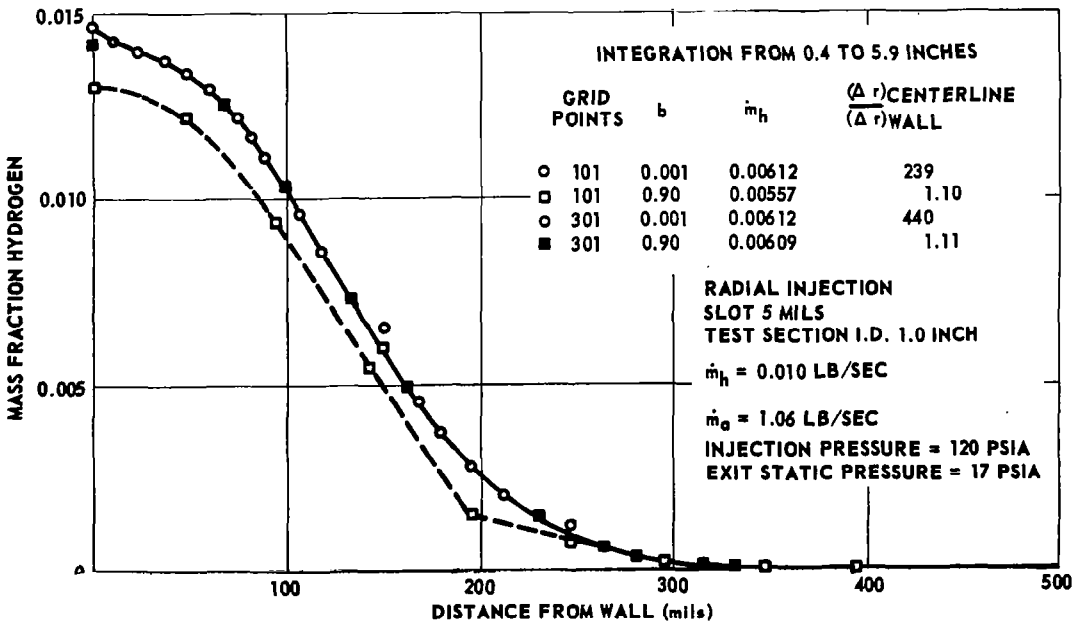

Fig. C–3 EFFECT OF CHANGING RADIAL GRID ON NUMERICAL SOLUTIONS.